Probing one-dimensional quantum systems through their entanglement structure

Kristian Ashley Patrick

School of Physics and Astronomy

University of Leeds

Submitted in accordance with the requirements for the degree of

Doctor of Philosophy

August 2019

Declaration

The candidate confirms that the work submitted is his/her own, except where work which has formed part of jointly authored publications has been included. The contribution of the candidate and the other authors to this work has been explicitly indicated below. The candidate confirms that appropriate credit has been given within the thesis where reference has been made to the work of others.

[1] Kristian Patrick, Titus Neupert, and Jiannis K. Pachos, *Topological quantum liquids with long-range couplings*, Physical Review Letters **118**, 267002 (2017).

The work in Chapter 3 is based on this paper. I am responsible for the numerical and analytical calculations. Neupert and Pachos directed the work.

[2] Kristian Patrick, Marcela Herrera, Jake Southall, Irene D'Amico, and Jiannis K. Pachos, *Efficiency of free auxiliary models in describing interacting fermions: from the Kohn-Sham model to the optimal entanglement model*, Physical Review B **100**, 075133 (2019).

The work in Chapter 4 is based on this paper. I am responsible for the non-perturbative bounds on density matrices and the analysis of the Hubbard dimer. Southall calculated the analytical solution for a four-level system. Herrera contributed numerical data for the Kohn-Sham approximation of the Hubbard dimer. D'Amico derived the trace distance bound in the perturbative limit. D'Amico and Pachos directed the work.

[3] Kristian Patrick, Vincent Caudrelier, Zlatko Papic, and Jiannis K. Pachos, *Interaction distance in the extended XXZ model*, Physical Review B **100**, 235128 (2019).

The work in this paper has not been included in this thesis.

There is nothing like looking, if you want to find something. You certainly usually find something, if you look, but it is not always quite the something you were after.

– J.R.R. Tolkien, *The Hobbit*

Acknowledgements

First and foremost I would like to thank my supervisor Prof. Jiannis Pachos. Without his perseverance, patience, and his ongoing support, I certainly would not have made it to the end of this PhD. His wisdom continually inspires me to make the right choices – not only in physics, but also in everyday life. Next, I thank those who I have worked alongside on publications: Zlatko Papic, Vincent Caudrelier, Irene D'Amico, Jake Southall, Marcela Herrera, and Titus Neupert. Over the time it has taken to reach this point I have learnt a lot from you about what it means to be a physicist and how to contribute positively to the field – thank you.

In addition to those who have helped with papers, there are a number of people who have also provided support for which I am grateful. First, I thank Nick Furtak and Chris Turner – it seems like only yesterday that the three of us were starting our PhD's, each with very different directions and interests. Throughout the PhD you have both been there to help with understanding physics problems and forgetting them, be that through board games, playing football, or drinks in the pub. I thank Lewis Clark and Konstantinos Meichanetzidis for being role models since day one and inspiring me to enjoy the finer things in life (craft beer and good music). Thank you also to the all other guys who have played an important part over the years: Ashk Farjami, Alex Bullivant, Chris Self, James de Lisle, Matt Bignold, Adam Infante, and the many others that are not forgotten.

Finally, I thank my family. My parents and brothers support me unconditionally and make it all worthwhile.

Abstract

Full knowledge of the entanglement properties of quantum systems can be used to identify different phases in condensed matter. Quantum correlations serve as a fingerprint for universal behaviours, leading to the discovery of new phases and new tools for probing them. In this thesis we use quantum correlations, as witnessed by the entanglement spectrum of a bipartitioned state, to probe the phases and behaviours of various one-dimensional quantum systems. In an era when novel quantum technologies are at the forefront of research it is important to find new models and new methods that may be applicable to the field. This thesis is a composition of two main works. The first is a study of a topological phase with non-local couplings, where we find that protected midgap states are split from zero energy whilst retaining their topological properties. The second aims to quantify the applicability of a known approximate method through the optimality of its entanglement spectrum. We determine bounds that confirm regions of applicability and suggest a new model that is by construction always optimal.

Contents

List of Figures

LIST OF FIGURES

Chapter 1

Introduction

1.1 Motivation

The landscape of quantum technologies is currently a very active, exciting area of physics. It brings together scientists from theoretical and experimental backgrounds in attempt to design and harness technologies that are unattainable with classical physics alone. This is not an entirely novel idea, for example semiconductors are quantum devices that have been used in electrical devices for around a century. However, modern quantum technologies rely on the direct manipulation of quantum states for some overriding purpose. There are two key technologies that are in mind throughout this thesis: quantum computation and quantum simulation.

A quantum computer differs from a conventional computer due to the manipulation of quantum bits rather than classical bits. Where a classical bit takes values $\{0, 1\}$, qubits are stored in entangled quantum states and takes superposition's of 0's and 1's, i.e. for a qubit built from a two-level system it can take any point between 0 and 1 that lie on the surface of a sphere extending into the complex plane. Exploiting this freedom, the quantum computer performs better than a classical computer for a certain set of specified tasks [5, 6, 7].

At the heart of this search is finding physical systems that can support the existence and manipulation of qubits. Due to the diversity of the field, there are many different flavours of quantum computer that may prove successful. A challenge for all flavours of quantum computation is finding quantum states that

are robust to small perturbations with long coherence times [8] – without this, the state would collapse onto a classical state and we lose the computational advantage of quantum mechanics. One contender uses ideas from topology, and has been the focus of intense research for the past couple of decades. This is with good reason, when a state is in a *topological phase* it receives a level of protection and robustness not afforded to other states. Fundamental to the existence of a topological phase is the special patterns of entanglement that they are built from [9, 10, 11]. By exposing its topological phase, it was suggested in [12] that protected qubits could be engineered in 1D. These systems are inherently simpler than those in higher dimensions and there has been success in their engineering through trapped ion systems [13, 14]. The work in this thesis is motivated in part by this search.

The aim of quantum simulation is to efficiently model complex quantum systems using other controllable quantum systems [15]. It was suggested by Feynman [16] that to do so computationally one would require a quantum computer. Though there has been an effort in simulating quantum systems both classically [17] and using quantum devices [18], it is important to develop new ideas for simplifying the complexity of known problems. One feature of interacting quantum systems is an exponentially growing Hilbert space required to completely describe them. Non-interacting systems have the advantage that the complexity in describing the Hilbert space grows linearly with the number of particles in the system. By determining when an interacting system can be accurately described by a free one opens up the possibility of a more efficient modelling of complex quantum states [19], whilst compressing the amount of information required for a full description.

The overall approach of the thesis uses the underlying quantum correlations of systems to probe characteristics that are desirable – the correlations are a result of entangled modes, the structure of these modes contains universal information about the state. By focussing on one-dimension, numerical analysis can often be supported by analytical calculations that would not be feasible in higher dimensional systems.

1.2 Structure of thesis

We begin in Chapter 2 by reviewing the different orders (or phases) and the structure of correlations in quantum systems. Quantum correlations are fundamental to expose such a variety of exotic phases that we know exist. Systems with inherent topological order are an example of this, for which the quantum Hall effect is a paradigmatic model. The entanglement spectrum is a set of energy levels that describe the entanglement between parts of a system, where the low-lying levels contain a 'signature' of the phase. This spectrum is used to probe the properties of different models in the later Chapters. Of particular importance is the distinction between single-particle entanglement spectra and the full many-body spectra. When there exists a single-particle description then the properties of a quantum state can be efficiently calculated. We then introduce the Kitaev chain as a topological free-fermionic model that can be used in the application to quantum technologies. We review its topological properties and the presence of Majorana zero modes in order to motivate further study in the field.

In Chapter 3 we introduce a generalisation to the Kitaev chain, the extended Kitaev chain, where long-range couplings are added. The choice in model is motivated through the development of engineered quantum systems that have been shown to have this property [20]. In order to probe the model directly we seek analytical solutions through a generating function method. From this method it is possible to extract information about edge mode energy, its localisation, and conditions for the existence of the topological phase. Following this, we study its entanglement spectrum in comparison to the local Kitaev chain to determine the signature of long-range couplings on a non-local model.

In Chapter 4 we move away from topology and include interactions between particles to find when free fermions offer a good approximation to an interacting model. A well-known method for approximating complex systems as free can be found in density functional theory. This theory has received much success, however, it is an approximate method and often fails to faithfully reproduce the correlations of a quantum state. To make this quantitative, we introduce the interaction distance as a diagnostic tool to probe its applicability. This tool diagnoses the entanglement spectrum as its primary objective and, as a byproduct,

it gives the optimal entanglement model with quantum correlations as close as possible to the interacting one.

Finally, in Chapter 5 the thesis is concluded, drawing on important findings from all studies in support of the overall motivation that is in the advancement of quantum technologies.

Chapter 2

Background

2.1 Introduction

It is the aim of this Chapter to introduce some of the key ideas that will be discussed in the remainder of the thesis. We begin by briefly introducing the different types of phases that we may explore when studying quantum matter. This begins with phases with orders described by Landau symmetry breaking and extends to those with a new kind of order: topological order. We then review what is known about correlations in free-fermionic and many-body systems, in order to motivate the entanglement spectrum as a tool for probing different phases. The entanglement spectrum is built from the weights of entangled modes in a bipartitioned state and contributes universal information about the state. It has been used as a fingerprint to characterise different phases of matter and will be an invaluable tool throughout this thesis. There is an emphasis on the spectra of both free and interacting models, as the distinction is important in the definition of the interaction distance that is defined and used in Chapter 4.

We then introduce an example free fermion model – the Kitaev chain – that displays a topological phase for some choice of parameter values. Interestingly, this model can derived by transformation from an interacting model. However, by modelling it as a non-interacting model we are able to uncover features that would be otherwise elusive. Topological systems are currently receiving a lot of attention due to their possible application in quantum technologies. We review

what makes the system topological, the existence of midgap Majoranas and a non-trivial invariant, as motivation for the work in Chapter 3 where we generalise the Kitaev chain and probe its topological features.

2.2 Quantum phase transitions, topological order, and symmetry protected phases

2.2.1 Landau symmetry breaking

At its core, condensed matter physics relies on the principle of emergence. Different orderings and configurations of particles are necessary to explain and engineer the large number of different phases that are already known. Consider a simple example: a collection of particles that form a liquid. When above a critical temperature $T > T_C$ (and with weak interactions between particles) the particles are organised with a random distribution. The system and state possess a continuous translational symmetry as any particle displacement will leave the overall system unchanged. At the critical temperature $T = T_C$ the particles undergo a transition and form a crystal structure for $T < T_C$. Now, only when particle displacement is by an integer number of lattice spacings does the system remain unchanged, so the system has a discrete translational symmetry. This is an example of spontaneous symmetry breaking, described by Landau's symmetry breaking theory [21, 22].

Importantly, the change in symmetry indicates a phase transition from a liquid to a crystal order. The transition is characterised by a local observable, or local order parameter, m, that has an expectation value of 1 in an ordered phase and 0 in an unordered phase [23]. In response to the change in the order parameter the state reduces its symmetry to minimise the overall energy, whilst the equations governing the system (the Hamiltonian) retain the full continuous translational symmetry. The type of transition depends on how the free energy changes at the critical temperature. For example, in a first order transition the free energy is discontinuous at the critical temperature, whereas for a second order (or continuous) phase transition the derivative of the free energy is discontinuous at T_C.

When explicitly describing a quantum phase transition we assume that the transition is driven by quantum fluctuations only, at $T = 0$. In this case only

the ground state of the Hamiltonian is of interest. Landau's symmetry breaking describe the phase transition, for example a superfluid is described by $U(1)$ symmetry breaking [24]. Of particular importance are second order quantum phase transitions where correlations become infinite ranged. This is interesting as microscopic details of the system can be ignored at the transition and Landau theory predicts universal behaviour that can be precisely calculated [24]. The universal behaviours depend on the symmetries present and models with the same symmetries fall into the same universality classes.

For decades it was believed that Landau's symmetry breaking captured all orders in materials and all continuous phase transitions. However, experimental and theoretical efforts in the late 1980's evidenced phases of matter that are not characterised by a local order parameter and symmetry breaking. Further, there exist universal properties of these new phases that are beyond Landau theory.

2.2.2 Topological Order

In this section we will introduce topological order, using an example from the beginning to help motivate the importance of it and its relevance to experiments. States with topological order are defined as gapped states, where there exists a finite gap between the ground state and first excited state, with long-range entanglement, i.e. they cannot be deformed into a trivial state by local unitary transformations [25]. The low energy physics is described by topological quantum field theories [26] and phases are identified by ground state degeneracy on any manifold, factionalised statistics (e.g. non-integer charge), and robustness to deformations of the Hamiltonian that do not result in the energy gap between the ground state and first excited state closing. On the other hand, there exist states with short-range entanglement and phases that are not described by Landau symmetry breaking. In these cases the topological groundstate is protected by a symmetry and is unique on any closed manifold. They are characterised by a topological invariant that is robust to deformations of the Hamiltonian, providing they do not close the energy gap or break the symmetry protecting the phase. These are symmetry protected topological phases and will be discussed

with another example later. Note that topologically ordered states may also have a topological invariant, though not in all cases.

In 1987, Kalmeyer and Laughlin [27] introduced the chiral spin state in an attempt to understand high temperature superconductivity. It was found that the state had broken time reversal and parity symmetries, whilst retaining spin rotation symmetry [28]. However, in contrast to what is predicted by Landau theory, there exist many different chiral spin states with the same symmetry [29]. Thus, there must be some other underlying order not accounted for by symmetry alone. Though they do not provide a complete understanding of high temperature superconductors, chiral spin states are closely related to the experimentally observed quantum Hall state [30] that has *topological order* [31]. To introduce topological order we now study the quantum Hall effect in more detail, beginning with the classical Hall effect [32].

The classical Hall effect

Consider electrons on an infinite conducting strip of width L_y in the $x-y$ plane, with a magnetic field B applied in the $\hat{z}$ direction. If a current I is allowed to flow in the $\hat{x}$ direction then the magnetic field will have the effect of inducing a voltage V_H in the $\hat{y}$ direction, where V_H is the Hall voltage. In order for an electron to travel through the strip when the current is flowing in equilibrium, the Lorentz force due to the magnetic field should equal the force due to the Hall voltage V_H, i.e.

$$\frac{e}{c}v_e B = \frac{V_H e}{L_y}, \tag{2.1}$$

where v_e is the electron velocity, e is electron charge, and c the speed of light. The current applied in the $\hat{x}$ direction is $I = \rho e v_e L_y$, with ρ the electron density. Then, the ratio of Hall voltage over current gives the Hall resistance:

$$R_H = \frac{V_H}{I} = \frac{B}{\rho e c}. \tag{2.2}$$

In addition, one may define the longitudinal resistance R_{xx} as the resulting ratio of the voltage in the direction parallel to the current with current itself. When the flow of current is at equilibrium, intuitively R_{xx} will be independent of the

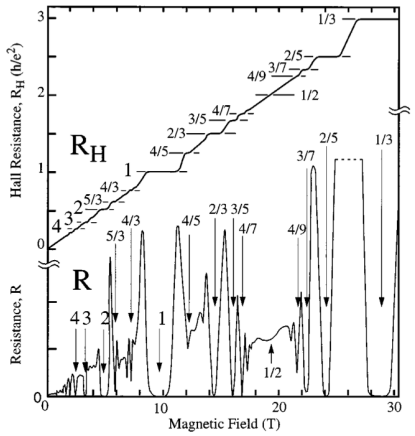

Figure 2.1: Quantum Hall data from an experimental study in close agreement with Eq. (2.3) [4]. The quantum number ν is labelled at each plateau and both longitudinal resistance and transverse resistance are shown as the magnetic field is varied.

magnetic field as the Lorentz force acts perpendicular to the current. However, so far this analysis does not take into account the quantum nature of electrons: we see that the resistance is a continuous function of magnetic field $B\hat{z}$.

Landau levels

In 1980, experimental results found that at low temperatures ($\sim$ mK) and with a strong magnetic field ($\sim$ 10T), where quantum effects become dominant, the Hall resistance was not a continuous function of the magnetic field and R_{xx} was zero for specific values of magnetic field [33]. Instead, the authors found plateaus at values close to

$$R_H = \frac{h}{e^2}\frac{1}{\nu}, \tag{2.3}$$

where ν is an integer (or a fraction $\nu = p/q$ [30], with p and q integers) and the ratio $\frac{h}{e^2}$ is the quantum of resistivity, see Fig. 2.1.

In order to explain the origin of this phenomenon we must first consider a single electron moving under a magnetic field $\nabla \times \boldsymbol{A} = B\hat{z}$ in the $x-y$ plane.

The Hamiltonian describing its motion is

$$H = \frac{1}{2m_b}\left[\boldsymbol{p} + \frac{e\boldsymbol{A}}{c}\right]^2, \tag{2.4}$$

where m_b is the electron band mass with charge $-e$. To find solutions, Hamiltonian (2.4) is simplified by making a gauge choice for the vector potential $\boldsymbol{A}$. One choice is the symmetric gauge: $\boldsymbol{A} = \frac{\boldsymbol{B}\times\boldsymbol{r}}{2} = \frac{B}{2}(-y, x, 0)$, that preserves rotational symmetry about the origin so that angular momentum is a good quantum number [34]. Fixing the unit of length to be the magnetic length $l = \sqrt{\hbar c/eB} = 1$, the Hamiltonian becomes

$$H = \frac{\hbar eB}{m_b c}(a^\dagger a + \frac{1}{2}), \tag{2.5}$$

where the ladder operators are $a^\dagger = \frac{1}{\sqrt{2}}\left(\frac{\bar{z}}{2} - 2\frac{\partial}{\partial z}\right)$ and $a = \frac{1}{\sqrt{2}}\left(\frac{z}{2} + 2\frac{\partial}{\partial \bar{z}}\right)$, with $z = x - iy = re^{i\theta}$, satisfying $[a^\dagger, a] = 1$ [35]. The factor $\omega_b = \frac{eB}{m_b c}$ is the cyclotron frequency of an electron orbiting in the $x-y$ plane, with the eigenvalue of $a^\dagger a$ giving the index n of the level, named a Landau level. The Landau levels are discretised and each level is separated by an energy gap $\hbar\omega_b$. The set of eigenvalues of Eq. (2.5) are given by $E_n = (n + \frac{1}{2})\hbar\omega_b$ with $n = 0, 1, 2, \ldots$ and E_0 named the lowest Landau level.

It is possible to define a second set of operators, $b^\dagger = \frac{1}{\sqrt{2}}\left(\frac{z}{2} - 2\frac{\partial}{\partial \bar{z}}\right)$ and $b = \frac{1}{\sqrt{2}}\left(\frac{\bar{z}}{2} + 2\frac{\partial}{\partial z}\right)$, that satisfy $[b^\dagger, b] = 1$ [35]. The z-component of angular momentum can therefore be defined by the operator $-i\hbar(b^\dagger b - a^\dagger a) = -i\hbar\frac{\partial}{\partial\theta} = -\hbar m$ with $m = 0, 1, 2, \ldots$ in the nth Landau level. The full space of single-particle states is given by the set $\{|n, m\rangle\}$ labelled by quantum numbers n, m, with the state $|0, 0\rangle$ destroyed by a and b:

$$|n, m\rangle = \frac{(a^\dagger)^n (b^\dagger)^m}{\sqrt{n!m!}}\,|0, 0\rangle\,. \tag{2.6}$$

The state with $n = m = 0$ is the Gaussian $\langle r|0, 0\rangle = \psi_{0,0}(r) = \frac{1}{2\pi}e^{-\frac{1}{4}z\bar{z}}$. By repeated application of $b^\dagger$ onto $|0, 0\rangle$ one can find all states in the lowest Landau level:

$$\psi_{0,m}(r) = \frac{z^m e^{-\frac{1}{4}z\bar{z}}}{\sqrt{2\pi m! 2^m}}. \tag{2.7}$$

States in the lowest level are radially symmetric (due to the gauge choice) with a peak at $r = \sqrt{2m}l$. We also know that all states with the same n quantum number are degenerate. Therefore, the degeneracy of the lowest level is found by calculating the maximum number of states that can fit into a circular region of radius R. The largest m that fits into this region is given by $M = R^2/2l^2$. The value M is also the total number of single-particle states that fit into the lowest level. The degeneracy per unit area is therefore $d = M/\pi R^2 = (2\pi l^2)^{-1}$. The magnetic length was previously defined to be $l = \sqrt{\hbar c/eB}$, leading to $d = \frac{B}{\Phi_0}$ with $\Phi_0 = hc/e$ the flux quantum. The filling fraction ν is then defined as the number of electrons per flux quanta:

$$\nu = \frac{\rho B}{\Phi_0}, \tag{2.8}$$

with ρ the electron density. The main result here is that the number of available states in each Landau level increases linearly with an increasing magnetic field. At integer values (and specific fractions) of ν are the centre of the plateaus in the Hall resistivity found in Fig. 2.1.

In order to construct a many-body state we take an antisymmetric product of $\psi_{n,m}$'s, filling the lowest levels first. Up to normalisation, the resulting state for the completely filled Landau level with $n = 0$ is [35]

$$\Psi_0 = \prod_{k<j}(z_k - z_j)\exp\left[-\frac{1}{4}\sum_j |z_j|^2\right]. \tag{2.9}$$

Integer quantum Hall effect

We are now in a position to discuss the integer quantum Hall effect and the role of topology. First, consider the effect of increasing the magnetic field for an electron gas confined to a two-dimensional plane. With fixed B, the electrons will fill $d = \frac{B}{\Phi_0}$ levels in the $n = 0$ Landau level, with any left over electrons filling the $n = 1$ level. As the magnetic field is increased the number of available orbitals d in the lowest level increases. This has the effect of reducing the number of occupied states in the higher landau levels. In order to see broad plateaus for a range of B values it is required that there is some disorder in the system so that excess electrons that spill over from the fully filled Landau levels are restricted to

filling only certain localised orbitals and do not contribute to the conductance. Put simply, the combination of disorder and filling discrete Landau levels result in the plateaus in the Hall resistance at $R_H = \frac{h}{e^2}\nu^{-1}$ and $R_{xx} = 0$, as observed in Fig. 2.1. The Hall resistance can be seen as an average over all of the flux quanta threading the system. This is, of course, not the entire story.

So far we have avoided mentioning the effect of boundaries on the system, considering only bulk effects. Let us make this more concrete by explicitly considering a torus, i.e. periodicity in the $\hat{x}$ and $\hat{y}$ directions, and seeing what happens to the ground state wavefunction $|\psi\rangle$ as it is perturbed by magnetic flux. Thread a flux through both $\hat{x}$ and $\hat{y}$ directions of the torus, given by Φ_x and Φ_y. We now want to see how the wavefunction evolves as a result of those fluxes. The idea is as follows: as a charge completes a closed orbit around a flux it picks up a non-trivial phase factor that depends only on the area of the path taken and not the path itself, this is the Aharanov-Bohm effect [36].

To see the topological nature of the model we need only explore the local $U(1)$ gauge symmetry of the vector potential given by [37]

$$\boldsymbol{A} \to \boldsymbol{A} + \mathrm{d}\chi \tag{2.10}$$

$$-i\hbar\partial_\alpha \to -i\hbar\partial_\alpha - e\partial_\alpha\chi, \tag{2.11}$$

for which the Hamiltonian in Eq. (2.4) is invariant. Now, define a translation operator $T(\boldsymbol{a})$ that translates the state by position vector $\boldsymbol{a}$

$$T(a) = e^{-\frac{i}{\hbar}\boldsymbol{a}\cdot\boldsymbol{p}}. \tag{2.12}$$

Translating the state about a closed curve C results in phase factor dependent on the area enclosed by the curve A_C only

$$P\exp\left[\frac{i}{\hbar}\oint_C \mathrm{d}x_\alpha p_\alpha\right] = \exp\left[-iA_C\right] \tag{2.13}$$

where P is a path ordering [37]. This non-trivial phase picked up by the wavefunction is the topological origin of the quantized Hall levels.

Alternatively, the non-trivial phase picked up by the wavefunction can be interpreted through the Berry curvature – a non-observable quantity that tracks changes in the phase of a wavefunction due to infinitesimal changes in parameter

space [38]. For the state $|\psi\rangle$ under the influence of the flux Φ_α the Berry curvature can be defined as

$$\mathcal{F} = -i\left[\frac{\partial}{\partial\Phi_y}\langle\psi|\frac{\partial\psi}{\partial\Phi_x}\rangle - \frac{\partial}{\partial\Phi_x}\langle\psi|\frac{\partial\psi}{\partial\Phi_y}\rangle\right]. \tag{2.14}$$

Note that it also possible to define a Berry curvature over the space of states rather than over parameter space. For this discussion we only need to focus on one representation of the curvature. The integral of the Berry curvature over all of parameter space results in the Chern number

$$C = \frac{1}{2\pi}\int d^2\Phi\ \mathcal{F}. \tag{2.15}$$

Remarkably, the Chern number is an integer and is related to the Hall conductance $\sigma_H = R_H^{-1}$ by

$$\sigma_H = -\frac{e^2}{h}C. \tag{2.16}$$

This shows that the Hall conductance is an example of a topological invariant, measured in units of e^2/h; for the integer quantum Hall effect it is also called the TKNN integer, named after the authors that realised the connection between the Hall plateaus and the topological invariant in 1982 [39]. This invariant is robust to deformation of the Hamiltonian that do not close the energy gap; as C is not continuous and only takes integer values small perturbations on the system do not change its value.

Finally, we can expose edge excitations in the quantum Hall effect. To do so, consider a geometry that is periodic in one direction and open in another, e.g. an open ended cylinder, with a magnetic field threading the sample. Now, the edges must host gapless states for the following reason: in the bulk of the sample there exists a non-trivial Chern number that is protected unless the gap closes; outside of the sample the Chern number is trivially zero; therefore, the energy gap must close at the interface between the two regions resulting in gapless edge modes. In Fig. 2.2 we sketch this setup. Electron orbitals in the bulk form cyclotron orbit, filling the lowest Landau level first. At the edge, due to the fixed clockwise motion of the orbitals, currents flow in only one direction, i.e. they are chiral. The current flowing at the edge of sample I_y is related to the topological invariant

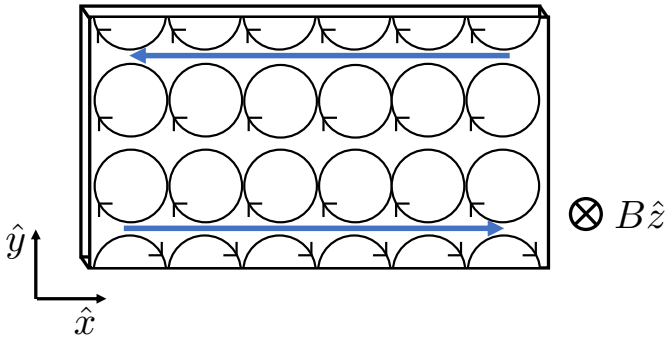

Figure 2.2: Sketch of the quantum Hall effect, with the magnetic field of strength B perpendicular to the plane coming out of the page. Bulk orbitals (depicted by full circles) localise due to disorder and form an insulator, where there exists a gap separating the occupied from unoccupied orbitals. With open boundaries along the $\hat{y}$ direction, there exist gapless edge currents formed by conducting electrons (depicted by semi-circles) at the boundary. The current at the edges is a global property, independent of microscopic details, making it a signature of topological order.

by $\sigma_H = I_y/V_H$. This is an example of bulk-boundary correspondence, where a bulk topological invariant implies the existence of gapless boundary excitations. The chiral edge modes are robust in the same way as the conductance plateaus characterised by the bulk topological invariant.

The fractional quantum Hall effect

From Fig. 2.1 it can be observed that plateaus also occur for non-integer values of the filling factor ν. In particular, the most prominent fractions are at $\nu = 1/m$ with m an odd integer [30, 34]. However, to move from the integer to the fractional quantum Hall effect requires electron-electron interactions; without interactions it is not possible to expose fractionalised excitations. It is justified to neglect Coulomb interactions when there are an integer number of Landau levels filled and the energy splitting between the Landau levels $\hbar\omega_b$ is much greater than the Coulomb interaction $\sim e^2/l$ [10]. For a partially filled Landau level, interactions become relevant when disorder is reduced so that overflow orbitals above the highest filled Landau level are no longer fixed to localise in the bulk. The under-

lying reason for the fractionalised filling factor is that interacting electrons form 'composite fermions' [35], or quasiparticle excitations, that have fractionalised exchange statistics [40]. The fractional quantum Hall state cannot be probed by a topological invariant in the same way as the integer quantum Hall effect, as the Chern number is restricted to integer values. Instead, they are exposed by their exchange statistics and edge excitations.

The wavefunction for the $\nu = 1/m$ quantum Hall state is given by the Laughlin state [34]

$$\Psi_{1/m} = \prod_{k<j} (z_k - z_j)^m \exp\left[-\frac{1}{4}\sum_j |z_j|^2\right]. \tag{2.17}$$

For m odd the state is anti-symmetric and is described by composite fermions. For m even the state is symmetric and represents a bosonic quantum Hall state. Take for example the $\nu = 1/3$ fractional quantum Hall state: this state is required to move around another fermion three times to return to its original state (fractionalised statistics) and has charge $-e/3$ (fractionalised charge) [31].

In both integer and fractional quantum Hall states there is long-range entanglement, i.e. states cannot be deformed to a trivial product state. However, it should be noted that under Kitaev's definition of topological order [41]: a gapped quantum systems with long-range entanglement and non-trivial excitations above the ground state; the integer quantum Hall state does not have topological order as it does not exhibit factionalised statistics. Thus, one could argue that topological orders also require interactions. For the purpose of this thesis, it is enough to note that topological orders arise from long-range entanglements and present themselves in a variety of ways, as evidenced by the different quantum Hall effects. Some other example systems with topological order include chiral spin liquids [42], $\mathbb{Z}_3$ parafermion states[43], and the Toric code [9].

2.2.3 Symmetry protected topological phases

Further to those states defined as having topologically order, there exist gapped ground states of quantum Hamiltonians without long-range entanglement where there are distinct phases not captured by Landau symmetry breaking arguments

(or any other non-topological orders, e.g. crystalline or spin orders). In these cases the phase is characterised by a topological invariant, for e.g. the Chern number introduced previously for the integer quantum Hall effect, that is robust to deformations of the Hamiltonian. When a non-local symmetry protects the non-trivial phase against perturbations the state is in a symmetry protected topological phase [44]. Further, and of particular importance to this thesis, all non-interacting gapped symmetry protected phases have been classified in the '10-fold way' [45]. We now look at this classification scheme in more detail.

Symmetry transformations on a non-interacting Hamiltonian

For free fermionic Hamiltonians with a gapped ground state there are three symmetries that dictate the classification: time reversal symmetry (TRS) given by the operator $\mathcal{T}$, particle-hole symmetry (PHS) by $\mathcal{C}$, and sublattice symmetry by $\mathcal{S}$, that result in 10 possible classifications [45]. The symmetries are defined by their action on creation/annihilation operators and on the Hamiltonian itself. For the following, consider the set of creation and annihilation operators $\left\{\hat{\psi}_j^\dagger, \hat{\psi}_j\right\}$ that act on a lattice with sites labelled $j = 1, 2, .., L$, satisfying the fermionic anticommutation relations $\{\hat{\psi}_j, \hat{\psi}_k\} = \delta_{j,k}$. Let $\hat{\psi}^\dagger, \hat{\psi}$ be vectors containing the respective lattice site operators. Then, the second quantised Hamiltonian of a non-superconducting system can be expressed as $\hat{H} = \hat{\psi}^\dagger H \hat{\psi}$, where H is an $L \times L$ matrix representation of the single-particle Hamiltonian. If the Hamiltonian is superconducting then we use the Bogliubov de Gennes Hamiltonian that contains Nambu spinors and not complex fermion operators [46], this will be touched on in later chapters.

Due to Wigner's theorem [47], symmetry operations on a Hilbert space can be represented by either a unitary, linear operator or an antiunitary, antilinear operator. Both a linear and antilinear transformation is a mapping $f : V \to W$ from a complex vector space to another, the former given by $f(ax+by) = af(x)+bf(y)$ and the latter by $f(ax + by) = a^* f(x) + b^* f(y)$, where * denotes complex conjugation. We are now ready to look at each of the symmetries in turn.

Time reversal symmetry

The time reversal operator is defined by the action of the antiunitary operator $\mathcal{T}$ on the fermionic creation and annihilation operators

$$\mathcal{T}\hat{\psi}_j\mathcal{T}^{-1} = (U_T)^k_j\hat{\psi}_k \qquad\qquad \mathcal{T}i\mathcal{T}^{-1} = -i \tag{2.18}$$

where $U_T = \{(U_T)^k_j\} \in \mathbb{C}^{L\times L}$ is a unitary [46].

The system is invariant under the action of this operator if both the second quantised Hamiltonian is invariant under its action $\mathcal{T}\hat{H}\mathcal{T}^{-1} = \hat{H}$, and the canonical commutation relations are preserved $\mathcal{T}\left\{\hat{\psi}^\dagger_j, \hat{\psi}_k\right\}\mathcal{T}^{-1} = \left\{\hat{\psi}^\dagger_j, \hat{\psi}_k\right\}$. From invariance of the Hamiltonian, we can derive a constraint on H:

$$\begin{aligned}
\mathcal{T}\hat{H}\mathcal{T}^{-1} &= \mathcal{T}\hat{\psi}^\dagger_i H^j_i\hat{\psi}_j\mathcal{T}^{-1} \\
&= \mathcal{T}\hat{\psi}^\dagger_i\mathcal{T}^{-1}\mathcal{T}H^j_i\mathcal{T}^{-1}\mathcal{T}\hat{\psi}_j\mathcal{T}^{-1} \\
&= \mathcal{T}\hat{\psi}^\dagger_i\mathcal{T}^{-1}(H^j_i)^*\mathcal{T}\hat{\psi}_j\mathcal{T}^{-1} \\
&= \hat{\psi}^\dagger_i[(U_T)^k_i]^*(H^l_k)^*(U_T)^j_l\hat{\psi}_j \\
&= \hat{\psi}^\dagger_i U_T^\dagger H^* U_T\hat{\psi}_j \\
&= \hat{H}.
\end{aligned} \tag{2.19}$$

Comparing the second to final and final lines we see that $U_T^\dagger H^* U_T = U_T^\dagger\mathcal{K}H\mathcal{K}^{-1}U_T = H$, so that the operator $T = U_T\mathcal{K}$ acts on H as $THT^\dagger = H$ where $\mathcal{K}$ is complex conjugation.

Finally, consider the action of applying the time reversal operator twice. We obtain $[(U_T)^*U_T]^\dagger H(U_T)^*U_T = H$. Due to Schur's Lemma this fixes $(U_T)^*U_T$ to a multiple of the identity matrix [46], i.e. $(U_T)^*U_T = e^{i\theta}\mathbb{1}$. However, U_T is unitary so $(U_T)^* = e^{i\theta}U_T^\dagger$. Taking the complex conjugate of this gives $U_T e^{i\theta} = U_T^T$, leading to $e^{2i\theta} = 1$. This gives two choices: $\mathcal{T}^2 = (U_T)^*U_T = \pm\mathbb{1}$. For an operator $\hat{O}$ composed of n fermionic operators the action of time reversal twice will be $\mathcal{T}^2\hat{O}\mathcal{T}^{-2} = (\pm1)^n\hat{O}$. The final constraint on the time reversal operator is therefore

$$\mathcal{T}^2 = (\pm1)^{\hat{N}}, \tag{2.20}$$

where $\hat{N} = \sum_j \hat{\psi}^\dagger_j\hat{\psi}_j$ is the total fermion number operator. This constraint tells us that for systems that are time reversal invariant and have $\mathcal{T}^2 = 1$ then they are

composed of particles zero or integer spin, if it has $\mathcal{T}^2 = -1$ then the particles have half-integer spin. We now apply the same analysis to the other two symmetries, but leave out the algebraic steps.

Particle-hole symmetry

Like with time reversal symemtry, we can define particle-hole symmetry (or charge-conjugation) $\mathcal{C}$ by its action on second quantised operators. The transformation acts on fermion operators as

$$\mathcal{C}\hat{\psi}_j\mathcal{C}^{-1} = (U_C)^k_j\hat{\psi}^\dagger_k \tag{2.21}$$

where $U_C = \{(U_C)^k_j\} \in \mathbb{C}^{L\times L}$ is a unitary. The system is invariant under the action of $\mathcal{C}$ if both the anticommutation relation and the second quantised Hamiltonian are invariant under it. Again, invariance of $\hat{H}$ leads to a constraint on H. In this case it is found that $CHC^{-1} = -H$ where $C = U_C\mathcal{K}$. This has the implication that for every single particle state $\hat{psi}_j$ with energy E_n, there exists a conjugate single-particle eigenstate $C\hat{\psi}_j$ with energy $-E_n$. Similarly to the previous case the final constraint on the operator is

$$\mathcal{C}^2 = (\pm 1)^{\hat{N}}. \tag{2.22}$$

If particle-hole symmetry is an invariant in a superconducting system and $\mathcal{C}^2 = 1$ then the system supports spin-triplet pairing whereas for $\mathcal{C}^2 = -1$ it supports spin-singlet pairing [46].

Sub-lattice symmetry

The combination of both time reversal and particle-hole symmetries gives a sub-lattice (or chiral) symmetry $\mathcal{S} = \mathcal{TC}$. It is defined by its action on the fermionic operators, inferred from Eqs. (2.18) and (2.21), as

$$\mathcal{S}\hat{\psi}_j\mathcal{S}^{-1} = (U_TU_C)^k_j\hat{\psi}^\dagger_k. \tag{2.23}$$

The action on H is found to be $U_SHU_S^\dagger = -H$ where $U_S = U_TU_C$, and the operator is constrained by

$$\mathcal{S}^2 = (\pm 1)^{\hat{N}}. \tag{2.24}$$

Interestingly, there exist systems where neither $\mathcal{T}$ or $\mathcal{C}$ are invariant, but $\mathcal{S}$ is.

Classification of non-interacting SPT phases: the 10-fold way

A complete classification of all possible non-interacting gapped fermionic phases was completed in [45] and is summarised in Table 2.2.3 – the table also extends to higher dimensions that have been omitted here. There are ten distinct categories found by different combinations of the symmetries $\mathcal{T}$, $\mathcal{C}$, and $\mathcal{S}$.

Class	$\mathcal{T}$	$\mathcal{C}$	$\mathcal{S}$	0	1	2	3
A	0	0	0	$\mathbb{Z}$	0	$\mathbb{Z}$	0
AI	+	0	0	$\mathbb{Z}$	0	0	0
AII	-	0	0	$2\mathbb{Z}$	0	$\mathbb{Z}_2$	$\mathbb{Z}_2$
AIII	0	0	1	0	$\mathbb{Z}$	0	$\mathbb{Z}$
BDI	+	+	1	$\mathbb{Z}_2$	$\mathbb{Z}$	0	0
CII	-	-	1	0	$2\mathbb{Z}$	0	$\mathbb{Z}_2$
D	0	+	0	$\mathbb{Z}_2$	$\mathbb{Z}_2$	$\mathbb{Z}$	0
C	0	-	0	0	0	$2\mathbb{Z}$	0
DIII	-	+	1	0	$\mathbb{Z}_2$	$\mathbb{Z}_2$	$\mathbb{Z}$
CI	+	-	1	0	0	0	$2\mathbb{Z}$

Table 2.1: Table of symmetry classes for free-fermionic Hamiltonians. The class name is in the first column, followed by the action of each of the symmetries $\mathcal{T}$, $\mathcal{C}$ and $\mathcal{S}$ on the single-particle Hamiltonian. The final columns give the resulting classification in dimensions $d = 0, \ldots, 3$. A result of 0 means that there is only a single (trivial) phase in that dimension, $\mathbb{Z}$ gives distinct topological phases, $\mathbb{Z}_2$ gives only two distinct topological phases.

The first column of Table 2.2.3 gives the name of the symmetry class; the next three are headed by a symmetry operator for e.g. $\mathcal{T}$, the corresponding value indicates if the symmetry is not an invariant 0, or if the symmetry is an invariant then the value shows the square of the operator, e.g. $\mathcal{T}^2 = \pm 1$. The final four columns are headed by the dimension of the system, with value of the corresponding to the possible number of distinct topological phases. For example, if a system only has particle-hole symmetry and the operator squares to $+1$, then it belongs in the symmetry class D. If the system is one dimensional then it has a $\mathbb{Z}_2$ topological invariant, meaning that there are two distinct topological phases.

The phases are robust as it is required to break the protecting symmetry or close the energy gap to move from one phase to another.

Having a complete classification scheme means that for a given Hamiltonian, by inspecting its symmetries alone, we know how many distinct topological phases that may exist. We will study an example of an SPT phase in more detail later in this chapter.

2.3 Correlations and entanglement measures

2.3.1 Free fermion correlations

Ground state of a non-interacting Hamiltonian

Consider a non-interacting Hamiltonian consisting of spinless fermions hopping between L lattice sites, for which we wish to study bipartite correlations in its groundstate. Let $c_j^\dagger(c_j)$ be the creation(annihilation) operators that act on a local Hilbert space of occupations $c_j |0\rangle = 0$ and $c_j^\dagger |0\rangle = |1\rangle$, satisfying $\{c_j^\dagger, c_k\} = \delta_{j,k}$ and $\{c_j, c_k\} = \{c_j^\dagger, c_k^\dagger\} = 0$. The local Hilbert space builds a Fock space that consists of all products of local occupations, e.g. for two occupations, an element of Fock space is $|10\rangle = |1\rangle \otimes |0\rangle$. The full Fock space is 2^L dimensional for L occupations.

The Hamiltonian is

$$H = -\sum_{j,k}^{L} t_{j,k} c_j^\dagger c_k, \tag{2.25}$$

where $t_{j,k} = t_{j,k}^* = t_{k,j}$ is the amplitude for hopping between sites j and k. The $t_{j,k}$ form an $L \times L$ Hamiltonian T that may be diagonalised by a unitary transformation U, i.e. $UTU^{-1} = \{E_j\}_{j=1}^L$. For now we choose to neglect any supeconducting terms, though the arguments that follow also hold with their inclusion providing terms are at most quadratic, e.g. $c_j^\dagger c_k^\dagger + c_k c_j$. Being explicitly free, H has eigenstates that are Slater determinants, Eq. (4.2). An appropriate linear combination of the original fermionic modes leaves H in its diagonal representation. Let the transformation be $d_k = \sum_{j=1}^L u_{j,k} c_j$, where $\{u_{j,k}\}$ build the unitary matrix U.

The Hamiltonian may be expressed as

$$H = \sum_{j}^{L} \Lambda_j d_j^\dagger d_j, \tag{2.26}$$

where the ground state is $|\psi_0\rangle = \prod_{\Lambda_j<0} d_j^\dagger |0\rangle$, with $|0\rangle$ the vacuum state and we set $E = 0$ as the Fermi energy.

Correlations of a single-particle state

To study correlations of the ground state we construct the single-particle correlation matrix C that contains all two-point correlation functions

$$C_{j,k} = \langle\psi_0| c_j^\dagger c_k |\psi_0\rangle . \tag{2.27}$$

As $|\psi_0\rangle$ is a free fermion state, through Wick's theorem all higher order correlations can be found as products of (particle number conserving) two-point correlation functions, e.g. $\langle c_j^\dagger c_k^\dagger c_l c_m\rangle = C_{j,m}C_{k,l} - C_{j,l}C_{k,m}$.

Often when studying topological states with an energy gap it is convenient to use a topologically equivalent 'flatband' Hamiltonian that is given by [48]

$$Q = \frac{\mathbb{1}}{2} - C, \tag{2.28}$$

with eigenvalues $\pm\frac{1}{2}$. This will be used later in Chapter 3 when studying correlations in the groundstate of a Majorana chain.

Bipartite correlations of a single-particle state

Now, we wish to study correlations between a subsystem A, consisting of M sites, and its complement B, with $L - M$ sites. The correlation matrix for subsystem A is found by simply using Eq. (2.27) and restricting the indices to $j, k \in A$, likewise for subsystem B. We shall see that the restricted correlation matrix is an important tool for probing bipartite correlations.

The reduced density matrix contains entanglement information between subsystems A and B. For the subsystem A, the reduced density matrix is found by tracing out the degrees of freedom in B of the full density matrix,

$$\sigma = \mathrm{Tr}_B |\psi_0\rangle\langle\psi_0| . \tag{2.29}$$

It has the property that the non-zero eigenvalues of σ are the same regardless of whether we choose to trace out A or B. This is good as we expect the bipartite entanglement to be a property of both subsystems (or more specifically the *partition*).

From a density matrix it is possible to extract the expectation value of a general operator O through the property $\langle O \rangle = \mathrm{Tr}\left[\sigma O\right]$. Therefore, we may also obtain elements of C through the relation

$$C_{j,k} = \mathrm{Tr}\left[\sigma c_j^\dagger c_k\right], \tag{2.30}$$

with the sites j and k in the subsystem A. Using Wick's theorem again, Eq. (2.30) is only true if the reduced density matrix σ is an exponential of free fermion Hamiltonian, i.e.

$$\sigma = \frac{e^{-H_E^f}}{Z}, \tag{2.31}$$

with $Z = \mathrm{Tr}\left[\sigma\right]$ a normalisation constant and H_E^f the free fermion *entanglement Hamiltonian*. This Hamiltonian can be built from the same fermionic operators as the original Hamiltonian in Eq. (2.25) [49]. Therefore, it can be expressed explicitly as $H_E = \sum_{j,k}^{M} h_{j,k} c_j^\dagger c_k$.

The entanglement Hamiltonian is diagonalised using the transformation $\tilde{d}_j = \sum_k \tilde{u}_{j,k} c_k$, where $\{\widetilde{U}\}_{j,k} = \tilde{u}_{j,k}$ build the $M \times M$ unitary matrix $\widetilde{U}$. Then, we are able to extract the free fermion entanglement spectrum $\{\epsilon_j\}$ as the eigenvalues of H_E^f,

$$H_E^f = \sum_j^M \epsilon_j \tilde{d}_j^\dagger \tilde{d}_j. \tag{2.32}$$

Following this analysis of correlations, it is clear that the eigenvalues ϵ_j of H_E^f are related to the eigenvalues λ_j of σ by $\epsilon_j = -\ln \lambda_j$. As σ is a density matrix it has non-zero eigenvalues in the range $\lambda_j \in (0, 1]$, so that $\epsilon_j \in [0, \infty)$.

One may also relate ϵ_j to the eigenvalues ζ_j of C. The form of (2.32) dictates that the reduced density matrix is

$$\sigma = \frac{1}{Z} \exp\left(- \sum_j^M \epsilon_j \tilde{d}_j^\dagger \tilde{d}_j \right). \tag{2.33}$$

Using this together with Eq. (2.30) gives an expression for $C_{j,k}$ in terms of the energies ϵ_j and the fermionic operators, i.e.

$$C_{j,k} = \mathrm{Tr}\left[\frac{1}{Z}\exp\left(-\sum_j^M \epsilon_j \tilde{d}_j^\dagger \tilde{d}_j\right) c_j^\dagger c_k\right]. \tag{2.34}$$

Remembering that the two sets of operators are related by a unitary transformation $\tilde{c}_j = \sum_k \tilde{u}_{j,k}^* d_k$, this simplifies the expression to

$$C_{j,k} = \mathrm{Tr}\left[\frac{1}{Z}\sum_m^M e^{-\epsilon_m}\tilde{d}_m^\dagger \tilde{d}_m \left(\sum_{m,n} \tilde{u}_{j,m}\tilde{u}_{k,n}^* d_m^\dagger d_n\right)\right]. \tag{2.35}$$

where in the exponential term we have used the fact that $e^X = \sum_k \frac{1}{k!}X^k$ and that the $\tilde{d}_m^\dagger \tilde{d}_m$ are occupations of eigenstates of H_E^f. These conditions result in the identity $\exp\left(-\sum_j^M \epsilon_j \tilde{d}_j^\dagger \tilde{d}_j\right) = \sum_j^M e^{-\epsilon_j}\tilde{d}_j^\dagger \tilde{d}_j$. Finally, by tracing over all eigenstates and remembering that $Z = \mathrm{Tr}\sigma = 1$ the expression simplifies further

$$C_{j,k} = \sum_l^M \frac{1}{e^{\epsilon_m}+1}\tilde{u}_{j,l}\tilde{u}_{k,l}^*. \tag{2.36}$$

Comparing this expression with the Hamiltonian in the same representation:

$$(H_E^f)_{j,k} = \sum_l^M \epsilon_m \tilde{u}_{j,l}\tilde{u}_{k,l}^*, \tag{2.37}$$

we find that the eigenvalues are related by

$$\zeta_j = (1+e^{\epsilon_j})^{-1}, \tag{2.38}$$

with $\zeta_j \in (0, \frac{1}{2}]$. These relations show that the entanglement spectrum is a reparameterisation of the set of probabilities of entangled modes. A low-energy entanglement energy corresponds to an entangled mode existing between subsystems A and B with high probability.

As a final note before continuing, it was remarked at the beginning of this analysis that all arguments given hold with the inclusion of quadratic pairing terms. To see this, one must simply make a transformation to Majorana fermions, $c_j = \gamma_{2j-1} + i\gamma_{2j}$. This transforms the Hamiltonian to an imaginary Hamiltonian of hopping Majoranas, that is of a similar form to Eq. (2.25) with the upper limit of the summations extended to $2L$ and $c_j \to \gamma_j$.

2.3.2 Many-body correlations

Many-body spectra from single-particle spectra

It is now the aim to find the entanglement spectrum of a fully interacting many-body system. Before doing so, let us consider what it means to build a many-body eigenstate from single-particle eigenstates. It was shown in Chapter 2 that it is possible to build such an eigenstate using a Slater determinant. In second quantised notation, this is equivalent to

$$|\Psi_j\rangle = \prod_{k=1}^{L} (d_k^\dagger)^{n_k(j)} |0\rangle \tag{2.39}$$

where $n_k(j) \in \{0, 1\}$ is the occupation of the single-particle level $d_k^\dagger d_k$ for the j^{th} many-body state. The restriction of occupations to 0 and 1 is due to Pauli's exclusion principle, it can take any natural number for bosonic modes.

The corresponding energy of the determinant $|\Psi_j\rangle$ is simply the sum of the single-particle energies used to construct it. In order to build the full set of 2^L many-body eigenvalues from L single-particle values it is required to take all possible combinations of single-particle states. A many-body energy level is therefore built in the following way

$$E_j = E_0 + \sum_{k}^{L} n_k(j)\Lambda_k, \tag{2.40}$$

where Λ_k is a single-particle energy level (see Eq. (2.26)) and E_0 is a constant shift in energy that is the result of additive terms, like a chemical potential $\sum_j \mu c_j^\dagger c_j$, being added to Hamiltonian (2.25). Likewise, a full many-body entanglement spectrum $\{E_j^f\}$ (for a free-fermion entanglement Hamiltonian of the form (2.25)) is built by taking all possible combinations of single-particle entanglement levels,

$$E_j^f = E_0^f + \sum_{k}^{M} n_k(j)\epsilon_k. \tag{2.41}$$

The additive constant is a result of normalisation $E_0^E = -\ln\left[\sum_j e^{-E_j^f}\right]$.

Many-body entanglement spectrum from an interacting state

We now consider the a state that is built from a Hamiltonian with explicitly interacting terms, for e.g. density-density interactions $\sum_j n_j n_{j+1}$, such that the Hamiltonian cannot be brought into a single-particle form and eigenstates are no longer Slater determinants. A general state for a system with L sites can be expressed in terms of the orthonormal basis states $\{|\phi\rangle\}$

$$|\Psi\rangle = \sum_{\phi} \alpha_\phi |\phi\rangle , \tag{2.42}$$

where α_ϕ is a normalised amplitude satisfying $\sum_\phi |\alpha_\phi|^2 = 1$. As with the single-particle state, the procedure for finding the entanglement spectrum requires calculating eigenvalues of the reduced density matrix $\rho = \mathrm{Tr}_B |\Psi\rangle\langle\Psi|$.

The basis states have support over the entire system and can be decomposed into a tensor product of orthonormal basis states $\{|\phi^A\rangle\}$, $\{|\phi^B\rangle\}$ in subsystems A and B, i.e. $|\phi\rangle = |\phi^A\rangle \otimes |\phi^B\rangle$. Eq. (2.42) is then

$$|\Psi\rangle = \sum_{\phi_A,\phi_B} \Pi_{\phi^A,\phi^B} |\phi^A\rangle \otimes |\phi^B\rangle , \tag{2.43}$$

where the summation runs over all basis states in the each subsystem Hilbert space. The matrix Π is rectangular, as the size of each subsystem is not fixed, and has dimension $\dim\{|\phi^A\rangle\} \times \dim\{|\phi^B\rangle\}$. It can be brought into a diagonal form by use of a Singular Value Decomposition. Any rectangular matrix may be expressed as $UDV^\dagger$, where U is a $\dim\{|\phi^A\rangle\} \times \dim\{|\phi^A\rangle\}$ matrix satisfying $U^\dagger U = 1$, V is a $\dim\{|\phi^B\rangle\} \times \dim\{|\phi^B\rangle\}$ matrix satisfying $VV^\dagger = 1$, and D is $\dim\{|\phi^A\rangle\} \times \dim\{|\phi^B\rangle\}$ with $\min\left[\dim\{|\phi^A\rangle\}, \dim\{|\phi^B\rangle\}\right]$ non-zero values $\{e^{-E_j^E/2}\}$ on the diagonal.

The operators U and $V^\dagger$ act on $|\phi^A\rangle$ and $|\phi^B\rangle$, that transform $|\Psi\rangle$ into its Schmidt representation

$$|\Psi\rangle = \sum_j e^{-E_j^E/2} |\Psi_j^A\rangle \otimes |\Psi_j^B\rangle , \tag{2.44}$$

where $|\Psi_j^A\rangle$ and $|\Psi_j^B\rangle$ form an entangled mode with weight $e^{-E_j^E/2}$. For a state in Schmidt form, the eigenvalues of the reduced density matrix $\{\rho_j\}$ can be easily

calculated $\rho_j = e^{-E_j^E}$ [50]. Therefore, the SVD provides an elegant way to extract the entanglement spectrum $\{E_j^E\}$ of a quantum state. From this form we can see that if the number of non-zero ρ_j (the Schmidt rank) is one, then the state $|\Psi\rangle$ is a product state. If the Schmidt rank is greater than one then we have an entangled state. It is also clear that the eigenvalues of ρ do not change whether we trace out subsystem A or B. They are a property of the entire system, that depends only on how (or where) one chooses to partition.

Diagnostics with the entanglement spectrum

Li and Haldane showed that the low-lying energies of the entanglement spectrum contain universal features of a topological phase [50]. When comparing the entanglement spectrum of a fractional quantum Hall state with its corresponding conformal field theory (CFT), they found that the spectrum is separated by an entanglement gap and the low-lying energies coincide with the spectrum of the CFT. The CFT characterises the phase, giving information about universal properties of the system. The high energy levels above the gap are 'generic' many-body levels that remain distinct for large system sizes. So the low-lying levels, that are the spectra of correlated quasiparticles between the two subsystems, contain the most relevant information for characterising the phase.

Also, in a topological state where there exist gapless edge modes in a non-trivial phase, the full entanglement spectrum has the signature of being degenerate at all levels [51]. This follows from the existence of a zero energy edge mode in the single-particle spectrum of the reduced state.

Finally, the entanglement spectrum is an important object in the density matrix renormalisation group (DMRG) technique [52, 53]. The technique is used to find accurate groundstates of 1D quantum systems. It works by variationally minimising the energy of a trial state, whilst growing the number of degrees of freedom and throwing away entanglement levels above a cutoff. By retaining the low energy levels it is possible to find groundstates for large system sizes to a very good accuracy.

2.3.3 Entanglement entropy

Definition of entanglement entropy

That the entanglement between two subsystems can be characterised through a set of levels corresponding to the probability of the entangled mode is very useful. However, as the number of levels may grow exponentially (though the number of physically relevant levels is likely to be a lot smaller) it would also be useful to have a single number that characterises how much entanglement a quantum system has. Define the *entanglement entropy* (von Neumann entropy) for the reduced density matrix ρ with eigenvalues $\{\rho_k\}$ as

$$S(\rho) = -\sum_k \rho_k \ln \rho_k. \tag{2.45}$$

If the input state is a product state with a single level $\rho_1 = 1$ then $S(\rho) = 0$, that signals no entanglement between subsystems A and B. If a set of N entangled modes exist with equal probability $1/N$ (so that ρ is maximally mixed) then the entropy is $S(\rho) = \ln N$, signalling a maximally entangled input state.

Applications of entanglement entropy

The entanglement entropy has applications in condensed matter physics, in quantum information, and likely in other areas of physics. In this thesis it is used primarily in the study of condensed matter systems where it displays universal behaviour of the system [54]. In particular, the scaling of $S(\rho)$ in critical systems matches results from CFT, where entropy scales with a multiplicative 'central charge' c. Thus, at critical points the large scale behaviour of the model is universal and the phase transition falls into a universality class [55]. This behaviour manifests due to the algebraic decay of correlations in a critical phase and can be summarised by the relation [54],

$$S(\rho) = \frac{c}{3} \ln L_A + \mathcal{O}(1), \tag{2.46}$$

where L_A is the size of subsystem A and c is the central charge.

On the other hand, non-critical gapped systems have an 'area law' scaling behaviour where entropy scales with size of the boundary between the two subsystems [56]. This follows from correlations decaying exponentially in gapped

systems, so entanglement builds up around the partition. The exponential decay defines a characteristic length scale, the correlation length ξ. Entropy in a non-critical gapped system in 1D will increase for partitions up to the scale of ξ, but beyond the extent of the correlation length the entropy saturates, i.e.

$$S(\rho) = S^* \tag{2.47}$$

where S^* is the saturation entropy and $L_A \gg \xi$. The cutoff S^* means that whilst the rank of ρ grows exponentially, the effective rank is actually much smaller and only finitely many entangled modes contribute to the entanglement. This is useful for numerical techniques such as the DMRG technique, where accurate groundstates can be found efficiently in 1D gapped systems by rejecting low weight states that do not contribute towards entanglement of the model [52, 53]. Conversely, Eq. (2.46) dictates that critical models will be less successful through a DMRG analysis as there will be many states contributing to $S(\rho)$.

2.4 From interacting spins to free fermions

The work in this thesis works mostly with free-fermions. This includes explicitly non-interacting models, like those introduced in the previous section, but also interacting models that have a free description (alternatively free fermions with an interacting description). A good example of a this is the Heisenberg XY spin chain with a transverse magnetic field. It is a 1-dimensional model of hardcore spin-$\frac{1}{2}$ bosons, with a Hamiltonian that has competing interactions seeking alignment of spins in both x and y spin directions. The anisotropy of these terms is characterised by a parameter γ, that moves the ground state between a spin ordered and a spin disordered phase. The model was solved analytically in 1961 by Lieb, Shulz and Mattis, and is an example of a quantum integrable (or exactly solvable) model [57].

Through a Jordan-Wigner transformation it is possible to map the Hamiltonian from local spins to a Hamiltonian of non-local spinless fermions. This transformation preserves the energy spectrum, whilst changing the underlying basis states that build the Hilbert space. Dirac fermions can be represented as Majorana fermions, completely real which new representation it was shown by

Kitaev [12] that the spin ordered phase is equivalent to a topologically ordered one. To do so, Kitaev introduces Majorana fermions that, when present as zero energy edge modes, indicate a topological phase.

2.4.1 Heisenberg XY spin chain

In its most general form, the Heisenberg model is one of spin-n hardcore bosons, each with spin components $\mathbf{S}_j$ labelled with lattice index j, that couple through an exchange interaction $\mathbf{S}_j \cdot \mathbf{S}_k$ with an exchange coupling $J_{j,k}$. This model has Hamiltonian

$$H = \sum_{j \neq k} J_{j,k} \mathbf{S}_j \cdot \mathbf{S}_k. \tag{2.48}$$

where each term seeks to align spins j and k in the same direction, with the energy cost for alignment given by $J_{j,k}$. These spins are vectors in Euclidean space, so label the three orthogonal components as $\alpha \in \{x, y, z\}$.

The model can be defined on any lattice in any dimension, d, for a spin-n particle, with the complexity of the problem increasing (in general) with increasing d and n. Here, we restrict to $d = 1$ and $n = \frac{1}{2}$ giving two orthogonal spin polarizations. Then, the spin operators take the form of the Pauli spin matrices, defined by

$$S^x = \frac{\hbar}{2}\begin{pmatrix} 0 & 1 \\ 1 & 0 \end{pmatrix} \qquad S^y = \frac{\hbar}{2}\begin{pmatrix} 0 & -i \\ i & 0 \end{pmatrix} \qquad S^z = \frac{\hbar}{2}\begin{pmatrix} 1 & 0 \\ 0 & -1 \end{pmatrix} \tag{2.49}$$

and $S^\alpha = \frac{\hbar}{2}\sigma^\alpha$, that act on a local Hilbert space of up spins $|\uparrow\rangle = \begin{pmatrix} 1 \\ 0 \end{pmatrix}$ and down spins $|\downarrow\rangle = \begin{pmatrix} 0 \\ 1 \end{pmatrix}$. The operators σ^α along with the identity I_2 are generators of $SU(2)$ that describe all rotations about a sphere in Euclidean space. They therefore provide a suitable (irreducible) representation of spin-$\frac{1}{2}$ particles, where the local Hilbert space consists of two states that can be represented on a Bloch sphere.

In making certain restrictions to the choice of exchange coupling in Hamiltonian (2.48), it is possible to expose different intriguing aspects of many-body

physics. The most general form is found upon setting all components of the coupling non-equal, i.e. $J_x \neq J_y \neq J_z \neq 0$. This describes an XYZ spin chain – an integrable model with a rich phase diagram. It is by no means a trivial task to find the ground state of an XYZ model for arbitrary system size. However, by restricting one of the exchange components to be zero, choose $J_z = 0$, it is possible to find all solutions, as it can be mapped to a free fermionic Hamiltonian – one that is quadratic in its second quantised fermionic operators.

In terms of the Pauli operators, the XY Hamiltonian is

$$H_{\mathrm{XY}} = \sum_j (1+\gamma)\sigma_j^x \sigma_{j+1}^x + (1-\gamma)\sigma_j^y \sigma_{j+1}^y + h\sigma_j^z \tag{2.50}$$

where the anisotropy of the x and y exchange couplings is dictated by the parameter γ and h is a transverse magnetic field that shifts the energy level of all states (by an equal amount in the same magnetisation sector). This Hamiltonian has a $\mathbb{Z}_2$ symmetry given by the non-local operator $\hat{P} = \prod_j \sigma_j^z$, where j runs across all sites and $[H_{\mathrm{XY}}, \hat{P}] = 0$. The operator has eigenvalues $P = \pm 1$ returning -1 for an odd number of down spins and $+1$ for an even number, providing a way to distinguish different configurations of spins. We will see now that this symmetry manifests as particle number conservation modulo 2, in the fermionic representation.

2.4.2 Kitaev's Majorana chain

In 1961, Lieb, Shulz, and Mattis, showed that the Heisenberg XY spin chain was exactly solvable, through a Jordan-Wigner transformation from bosonic spins fixed at lattice sites to spinless (non-local) non-interacting fermions. The authors also show that it is possible to find a complete set of solutions for any free fermionic Hamiltonian, and exploit this hidden simplicity of the many-body problem. In that work, it was found that there exists a degeneracy in the ground state when the number of spins is taken to infinity Taking a combination of these ground states reveals end-to-end order, i.e. that spins at sites 1 and N align, a *quasi*-long range order in 1D.

It was nearly 30 years before Kitaev exploited the model further and realised that one can decompose these spinless fermions into Majorana fermions. It is the

presence of unpaired Majorana fermions localising at the boundary of a chain with open ends that results in the end-to-end order Lieb, Shulz, and Mattis witnessed many years before. It was shown that these energy modes are topological and are protected from small perturbations due to the presence of an energy gap between them and the bulk energy states.

Local Hamiltonian in fermionic representation

By a Jordan-Wigner transformation we can represent Hamiltonian (2.50) in terms of fermions. To do so, first rewrite the Pauli operators as spin raising and lowering operators $\sigma^{\pm} = \sigma^x \pm i\sigma^y$. Then, the Jordan-Wigner transformation takes a spin excitation to a fermionic excitation with non-local string, i.e. $c_j^\dagger = \prod_{k<j} \sigma_k^z \sigma_j^+$, and the hermitian conjugate gives the relation for the reverse. The $c_j^\dagger(c_j)$ operators are spinless fermionic operators acting on a Fock space, satisfying $\{c_j^\dagger, c_k\} = \delta_{j,k}$ and $\{c_j, c_k\} = \{c_j^\dagger, c_k^\dagger\} = 0$.

In the form given by Kitaev, Hamiltonian (2.50) with L sites and open ends is

$$H_{\text{Kit}} = \sum_{j=1}^{L-1}(-Jc_j^\dagger c_{j+1} + \Delta c_j c_{j+1}) + \text{h.c.} + \sum_{j=1}^{L} \mu c_j^\dagger c_j \tag{2.51}$$

where $J \in \mathbb{R}$ is the energy contribution for fermions tunnelling between sites, $\Delta = |\Delta|e^{i\theta}$ is the cost for creating superconducting Cooper pairs, and $\mu \geq 0$ is a chemical potential that acts locally at all sites. Hamiltonian (2.51) contains terms that are quadratic in the fermionic operators and is therefore explicitly non-interacting.. Conversely, an interacting Hamiltonian would contain terms with order greater than two in the fermionic operators, for example $c_j^\dagger c_j c_k^\dagger c_k$ that describes an interaction between fermionic populations at sites j and k. Interactions akin to this are discussed in later chapters, for now we restrict to formally non-interacting systems.

Solution for the closed chain

It is possible to find solutions to Hamiltonian (2.51) for both open and closed boundary conditions. The latter requires an additional boundary term $H_{bound.} =$

$\beta[-Jc_N^\dagger c_1 + \Delta c_N c_1 + \text{h.c.}]$ that ensures translational symmetry, where $\beta = +1(-1)$ gives periodic (antiperiodic) boundary conditions PBC(APBC). Preservation of translational symmetry corresponds to conversation of momentum and so the Hamiltonian may be diagonalised in a momentum representation. For the annihilation operator the transformation is given by

$$c_j = \frac{1}{\sqrt{L}} \sum_{k \in BZ} e^{-ijk} c_k \tag{2.52}$$

where the sum is over all wave numbers in the Brillouin zone, that are fixed by the choice of boundary condition. With PBC Eq. (2.52) gives

$$c_{J+L} = \frac{1}{\sqrt{L}} \sum_{k \in BZ} e^{-i(j+L)k} c_k \tag{2.53}$$

$$= \frac{1}{\sqrt{L}} \sum_{k \in BZ} e^{-ijk} c_k \qquad = c_j, \tag{2.54}$$

that identifies the equality $e^{-ikL} = 1 = e^{2\pi n}$ with $n \in \mathbb{Z}$. Thus the allowed wave numbers are restricted to $k = \frac{2\pi n}{L}$ for any integer n. Via a similar argument for APBC one finds $k = \frac{(2n+1)\pi}{L}$. This set of k values is restricted further by recognising that the system is periodic by translation of k by 2π, thus the first Brillouin zone is the set of allowed wave numbers in a 2π interval, i.e. $k \in [-\pi, \pi)$. There exist exactly L numbers in this interval separated by $\frac{2\pi}{L}$.

The Hamiltonian can be conveniently in written as a sum over points in the Brillouin zone (in BdG form) $H = \sum_k \psi_k^\dagger \mathcal{H}(k) \psi_k$,

$$H = \sum_k \begin{pmatrix} c_k^\dagger & c_{-k} \end{pmatrix} \begin{pmatrix} J\cos(k) + \frac{\mu}{2} & -i\Delta\sin(k) \\ i\Delta\sin(k) & -J\cos(k) - \frac{\mu}{2} \end{pmatrix} \begin{pmatrix} c_k \\ c_{-k}^\dagger \end{pmatrix} \tag{2.55}$$

where the delta function $\delta_{p,q} = \frac{1}{N}\sum_j e^{-i(p-q)j}$ has been used. The Bloch Hamiltonian is given by $\mathcal{H}(k)$. Each wave number corresponds to a single-particle energy given by the determinant of the Hamiltonian $\mathcal{H}(k)$. This results in a *bulk* spectrum given by

$$E_{\text{bulk}}^{\pm}(k) = \pm\sqrt{\left|\frac{\mu}{2} + J\cos(k)\right|^2 + |\Delta\sin(k)|^2}. \tag{2.56}$$

The presence of the superconducting term is to induce a gap in the spectrum defined by $E_{\text{gap}} = 2\min_k E^+_{\text{bulk}}(k)$. Including the energy, the form of $\mathcal{H}(k)$ allows other useful quantities to be extracted, such as relevant symmetries and a topological invariant.

Winding number topological invariant

We have already discussed the existence a $\mathbb{Z}_2$ symmetry in the XY model – we now aim to probe the phases through an invariant. When a Hamiltonian has a gap in its single-particle spectrum it is the case in some systems that midgap states can exist, protected against perturbations by the presence of the gap separating them from all other levels. This is an example of a topological phase, where the Hamiltonian cannot be continuously deformed into one without midgap states without the spectral gap closing. Of course, if one breaks the symmetry defining the phase of the Hamiltonian then the spectrum could change drastically – thus we call these states symmetry protected states. Another kind of topological protection arises in topologically ordered states [58]; however, there is no long-range order in 1D [59] so the phase must be protected by some symmetry for all systems studied in this thesis.

A well-used invariant to probe topological phases is the winding number, ν. From the Bloch Hamiltonian in Eq. (2.55) we may study the winding θ_k of the Hamiltonian as it varies in k-space. Define the normalised vector $\hat{h}(k) = \frac{h(k)}{|h(k)|} = (h_x, h_y, h_z)$ where $\mathcal{H}(k) = h(k)\cdot\sigma$ and $\sigma = (\sigma_x, \sigma_y, \sigma_z)^T$ is the vector of Pauli matrices. The winding number $\nu = \frac{1}{2\pi}\int_{BZ} d\theta_k$ counts how many times the vector $\hat{h}(k)$ winds about the origin as k is varied. As there is no σ_x component in (2.55), we define the angle the vector $\hat{h}(k)$ makes with the σ_z axis as $\tan\theta_k = h_y/h_z$ so that the winding number can be expressed as

$$\nu = \frac{1}{2\pi}\int_{BZ} dk \frac{h_z h_y' - h_y h_z'}{h_y^2 + h_z^2}, \tag{2.57}$$

that is amenable to both analytical and numerical calculation. The prime notation, e.g. h_x', represents the partial derivative with respect to the wave vector k. A non-zero winding corresponds to a topological phase with zero winding a

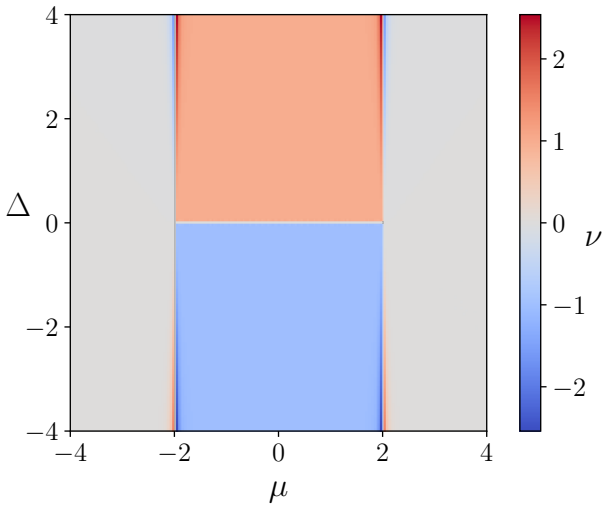

Figure 2.3: Winding number analysis of the local Kitaev chain with PBC, $J = 1$ and varying Δ and μ couplings. There are four distinct regions in phase space. The grey regions with $\nu = 0$ are in a topologically trivial phase for all $|\mu| > 2J$. There is a non-zero winding number in the region $|\mu| < 2J$ providing $\Delta \neq 0$. The lines $|\mu| = 2J$ and $\Delta = 0$ are points where $E_{\text{gap}} = 0$, in agreement with Eq. (2.56).

trivial phase – due to a bulk-boundary correspondence, the winding of a periodic chain counts the number of gapless boundary modes in the bulk gap of an open chain [12]. Let us first analyse the winding of the Bloch Hamiltonian before moving to the open chain.

In Fig. 2.3 we plot the winding number of the Bloch Hamiltonian, Eq. (2.55), calculated numerically using Eq. (2.57). The plot shows four distinct regions in parameter space, two grey regions with $\nu = 0$, a red region with $\nu = 1$ and a blue region with $\nu = -1$. The critical lines separating the regions are $|\mu| = 2J$ and $\Delta = 0$, that agree with the gap closing points of $E^{\pm}_{\text{bulk}}$, in Eq. (2.56).

The regions with $\nu = 0$ characterise the trivial phase, where we do not expect to see midgap states on the open chain. Both regions with $|\nu| = 1$ describe a topological phase as the winding vector makes a full clockwise or anticlockwise revolution about the origin. The only difference between the two phases is the

sign of Δ that results in the vector winding in the opposite direction. However, these two values of ν describe the same topological phase. A better topological invariant would therefore be the absolute value of the winding number, $\nu_K = |\nu|$, so that there is no distinction between $\nu = \pm 1$.

Whether we choose ν or ν_K, we now get an idea of what is meant by 'topological protection' – we see that for the winding number to change the bulk gap must close. Therefore, if a system is in a topological phase, providing the bulk gap does not close we may deform the Hamiltonian however we see fit and the system will remain in the same topological phase. Before moving to the open chain and exposing other signatures of a topological phase, we complete our analysis of the BdG Hamiltonian by looking at its symmetries.

Symmetries

With the Hamiltonian in BdG form in Eq. (2.55), the time reversal operator is of the form $T = \mathcal{K}\sigma_z$, the particle-hole operator is $C = \mathcal{K}\sigma_x$, and the chiral operator is $S = TC$. When acting on $h(k)$ the operators must satisfy the following equations

$$Th(k)T^\dagger = h(-k) \qquad\qquad Ch(k)C^\dagger = -h(-k). \tag{2.58}$$

Indeed, for the Kitaev model all three symmetries are present and it can be easily shown that $T^2 = C^2 = S^2 = +1$ using their explicit expressions given above. Following the 10-fold way symmetry classification presented in Section 2.2.3, this model belongs to the BDI symmetry class and can be described by a $\mathbb{Z}$ topological invariant. However, we know that the XY model has a $\mathbb{Z}_2$ symmetry. We also saw in Fig. 2.3 through a winding number analysis that there are only two distinct phases. Therefore the $\mathbb{Z}$ classification can be reduced to a $\mathbb{Z}_2$ classification that fully captures the phases of the model. To see this further we transform to the Majorana representation.

Majorana representation

To fully expose what makes the topological phase of the Kitaev chain we must first transform to a Majorana representation. They are real operators satisfying

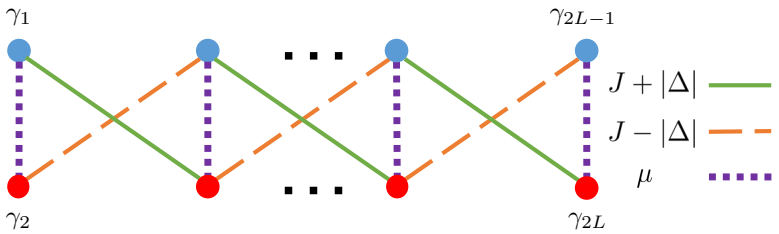

Figure 2.4: Pictorial representation of the couplings in Hamiltonian (2.60), with L fermionic sites. Majoranas connected by μ (purple, short dashed) are of the same fermionic site. The solid green and dashed orange lines are Majorana hopping amplitudes. Majoranas from different fermionic sites pair up when $J = |\Delta|$ or $J = -|\Delta|$, leaving unpaired Majoranas at the ends that are the zero energy edge modes.

$\gamma^2 = 1$, i.e. their action on a state can be either to create a Majorana excitation or to annihilate an excitation, and are related to the fermionic operators by

$$c_j = \frac{\gamma_{2j-1} + i\gamma_{2j}}{2} \qquad c_j^\dagger = \frac{\gamma_{2j-1} - i\gamma_{2j}}{2}. \tag{2.59}$$

This process is analogous to splitting a complex number into its real and imaginary parts. So that the fermionic anticommutation relation to holds, $\{c_j^\dagger, c_k\} = \delta_{j,k}$, the Majorana operators must satisfy $\{\gamma_j, \gamma_k\} = 2\delta_{j,k}$ that gives back the condition $\gamma_j^2 = 1$ when $j = k$. We call the Majoranas 'fermions' as they satisfy an anticommutation relation, however they are altogether quite a different kind of particle. In particular, as there is no well defined number operator for a single Majorana (as $\gamma^2 = 1$) they must exist in pairs. Expressed as Majoranas, the number operator for a fermion excitation is $c_j^\dagger c_j = \frac{1+i\gamma_{2j-1}\gamma_{2j}}{2}$, so that $i\gamma_{2j-1}\gamma_{2j} = \pm 1$ depending on whether a fermionic mode is occupied $(+1)$ or not (-1).

Majorana representation of Kitaev chain

Decomposing the fermions of Hamiltonian (2.51) into Majorana fermions results in the following representation of H_{Kit}

$$H_{\text{Kit}} = \frac{i}{2}\sum_{j=1}^{L-1}\left[(|\Delta|+J)\,\gamma_{2j-1}\gamma_{2j+2} + (|\Delta|-J)\,\gamma_{2j}\gamma_{2j+1}\right] + \frac{i}{2}\sum_{j=1}^{L}\mu\gamma_{2j-1}\gamma_{2j}, \tag{2.60}$$

where the complex superconducting phase $\Delta = e^{i\theta}|\Delta|$ has been hidden in the Majorana operators $c_j^\dagger = e^{i\theta/2}\left(\frac{\gamma_{2j-1}-i\gamma_{2j}}{2}\right)$ and any constant shifts in energy have been omitted. The Hamiltonian remains quadratic in the new operators. When expressed as $H_{\text{Kit}} = \frac{i}{4}H$ we see that H is skew-symmetric satisfying $H^T = -H$. It can therefore be brought into a block-diagonal form using a unitary operator U, such that $H = U\Sigma U^T$ with $\Sigma = \oplus_n \Lambda_n \begin{bmatrix} 0 & 1 \\ -1 & 0 \end{bmatrix}$ and Λ_n the set of single-particle energies.

In Fig. 2.4 there is a pictorial representation of the couplings in a Majorana basis. Particle and hole degrees of freedom are replaced with Majorana occupations, extending the number of effective sites from L to $2L$, with Majoranas connected by μ occupying the same fermionic site. Such a figure becomes enlightening when one considers extremal cases: i) $J = \Delta = 0$ and $\mu > 0$ or ii) $J = -|\Delta| > 0$ and $\mu = 0$. Beginning with case (i), there a Majorana only couples with the other Majorana at the same fermionic site. Without tunnelling fluctuations or pairing to open a gap the system remains uninteresting – this is a trivial phase. For case (ii) Majoranas couple with a Majorana at a neighbouring site, leaving γ_1 and γ_{2L} unpaired. These Majoranas form a non-local fermion and are at zero-energy as they do not enter the Hamiltonian – this is a topological phase.

As the energy of the *quasiparticle* is zero the many-body groundstate has the same energy whether it is occupied or not, thus we expect a two-fold degenerate groundstate. The two states differ by fermionic parity $P = \prod_j (-1)^{n_j} = \prod_j (-i\gamma_{2j-1}\gamma_{2j})$. To see this, consider the limiting case in the topological phase from above. The Hamiltonian is diagonal with Majoranas paired a different sites, i.e. $H = \sum_j \Lambda_j (d_j^\dagger d_j - \frac{1}{2})$ with $d_j = \gamma_{2j} + i\gamma_{2j+1}$. The groundstate $|0\rangle$ is therefore annihilated by all d_j, $d_j|0\rangle = 0$. Now, the parity operator can be expressed in

terms of the new fermionic operators $\prod_j(-i\gamma_{2j-1}\gamma_{2j}) = -i\gamma_1\gamma_{2L}\prod_j(1-d_j^\dagger d_j)$. As $d_j|0\rangle = 0$ for all j, the action of parity on the groundstate is reduced to $P|0\rangle = -i\gamma_1\gamma_{2L}|0\rangle$, where $i\gamma_1\gamma_{2L} = \pm 1$ represents an occupation (-1) or no occupation (+1) of a non-local fermion $f = \gamma_1 + i\gamma_{2L}$. Thus, the degenerate groundstate modes can be labelled by their parity $|0_\pm\rangle$, obeying $f^\dagger f|0_+\rangle = 0$ $f^\dagger f|0_-\rangle = 0$.

For values away from the ideal values discussed above, edge modes remain localised to the boundary and decay exponentially away from it. In the infinite limit this treatment is exact and diagonalisation of the Hamiltonian would result in a pair of zero energy modes in the middle of the gap. For finite system sizes the modes are split from zero due to an overlap between the two edges. However, the edge modes remain exponentially localised at the boundary, protected by the presence of a gap, with a splitting $\sim e^{-L/l}$ that depends on the distance between the edges L and the localisation length l [12].

2.5 Summary

In this Chapter we have introduced some of the key ideas that are discussed in the remainder of the thesis. In particular, there is a focus on the entanglement spectrum of a bipartitioned state and on the topological phase of a Majorana chain.

We showed that the single-particle entanglement spectrum can be found through the eigenvalues of the single-particle correlation matrix restricted to a subsystem. It contains the weight of a single-body entangled modes across a partition. The many-body entanglement spectrum is built from the single particle levels by finding all occupation patterns of single-particle modes. The entanglement spectrum of an interacting state requires that the parent Hamiltonian cannot be brought into a quadratic form, otherwise the entanglement Hamiltonian would also be quadratic. An interacting entanglement Hamiltonian mixes the single-particle entangled modes, that requires exponentially many many-body entanglement levels to fully describe. Thus, if a quantum state has a free description it is computationally more convenient to find the the underlying single-particle modes rather than the full many-body entanglement spectrum.

We then gave an example of an interacting Hamiltonian – an XY model with a transverse field – that can be transformed to a free-fermionic Hamiltonian by a Jordan Wigner transformation – the Kitaev chain. In this case, it would be advantageous to find the entanglement spectrum from the single-particle correlation matrix rather than the full reduced density matrix of the many-body state. The free-fermionic representation is enlightening as it allows for exact solutions and is computationally efficient to model. By a transformation to the Majorana basis we showed that the model is topological: it has a non-trivial topological invariant in the bulk and midgap zero energy Majorana edge modes at the boundary of an open chain. This opens the question, can other systems host Majorana edge modes? The answer is of course yes and the search is certainly on for finding different systems capable of hosting edge states.

Chapter 3

Probing the topological phase of a non-local Majorana chain

3.1 Introduction

In this Chapter, we study the topological properties of a Majorana chain with extended range hopping and pairing. In the previous Chapter we studied the local Majorana chain, showing that it has single-particle energies of zero energy exponentially localised at the boundary in a topological phase. This is complemented by a non-trivial topological index that can be evaluated for open or closed chains. The Majorana chain is a 'toy model' proposed to expose edge Majoranas that have applications in quantum computing and quantum technologies. The interest in extending the range of couplings to include non-local couplings follows experimental proposals, where cold atom setups may be engineered with an effective Hamiltonian like the Kitaev chain and including variable range hopping and pairing terms [60, 20, 61, 62]. It was found in [20] that a consequence of long-range couplings, in a setup of magnetic impurities placed in contact with a superconductor, is that edge modes may persist at the critical point in absence of the topological gap.

Following experimental studies, theoretical interest shifted towards characterising the topological phase of long-range models through a 'toy model' approach i.e. construct a model Hamiltonian with appropriate tunnelling and pairing terms, in order to analyse the energy, localisation properties and a relevant topological

invariant. In an attempt to model more physically realistic setups, in [63] the authors include a three spin interaction to the XY model extending the nearest coupling to next nearest neighbour. This interaction dramatically changes the phase diagram of the XY model, introducing another distinct topological phase with two Majorana edge modes. Further, in the following studies [64, 65, 66, 67, 68], the pairing terms are extended to long-range whilst including a decay parameter. They also found that phase diagram was modified, where now the strength of the long-range couplings alters the properties of edge modes. In general, dependent on whether hopping, pairing, or both are extended, the model exhibits a variety of novel phenomena. This includes edge modes with non-zero energy and also multiple edge modes that require a full $\mathbb{Z}$ classification [63, 69], contrary to the sufficient $\mathbb{Z}_2$ classification of the local model [12].

The work presented in this Chapter is adding to the conversation about free fermionic long-range topological phases, where we aim to find analytical solutions to a long-range model and study the characteristics exposed in its entanglement spectrum [1]. We first introduce the model in a more general form, where it is has many tunable parameters that exposes a variety of different phases [69]. This motivates the choice of model that we then focus on – one with open boundaries and infinite range couplings.

3.2 The non-local generalisation of the Kitaev chain

Following the notation introduced in the previous Chapter, define the Hamiltonian for an extended Majorana chain in one-dimension and with PBC $a_{L+j} = a_j$ to be

$$H = \sum_{j=1}^{L} \sum_{l=1}^{r} \left(e^{i\phi_l} \frac{J}{d_l^{\alpha}} a_j^{\dagger} a_{j+l} + \frac{\Delta}{d_l^{\beta}} a_j a_{j+l} \right) + \frac{\mu}{2} a_j^{\dagger} a_j + \text{h.c.}, \tag{3.1}$$

where we have extended the hopping and pairing terms to include up to r nearest neighbours, with a strength that decays with distance $d_l = \min(l, L - l)$. The type of decay, e.g. power-law, exponential, or some other, is generic; however,

power-law is chosen here in line with experimental setups [60, 20, 61]. A complex phase has been introduced in the hopping term, ϕ_l, that can be chosen to break time reversal symmetry; while the exponents α and β are chosen to expose either long-range hopping, long-range pairing, or both.

In our work [1] we take $\alpha = \beta$ on a chain with OBC and $r \to L - j$ for the entire study and allow its value to range from infinite range for $\alpha = 0$ to the local chain for $\alpha \to \infty$; however, through the periodic chain we may motivate our reasons why.

3.2.1 Extremal cases: recovering the local chain and extending to infinite range couplings

It is helpful to first consider some limiting cases of the different parameters that are at our disposal. At one extreme, the short-range Majorana chain is found by either letting $r = 1$ or taking the limit $\alpha, \beta \to \infty$[1], with $\phi = 0, \pi$ to preserve TRS. In this limit there exists a topological phase characterised by a non-trivial integer winding number when $\mu < 2J$ and $\Delta \neq 0$, as discussed in the previous Chapter.

At the other extreme is the infinite-range chain where there exist couplings of equal strength between all sites, that is found by extending r and setting $\alpha, \beta = 0$ removing any d_l dependence from the Hamiltonian. On a periodic lattice, it is not possible to simply set $r = L - 1$ as this results in cancellation's of terms in the Hamiltonian. To see this, consider an infinite-range chain with PBC and $r = L - 1$ for some generic L. In the Hamiltonian there exists pairing terms like $a_j a_k + a_k^\dagger a_j^\dagger$, with $k = j + l$ for some l, and also $a_k a_j + a_j^\dagger a_k^\dagger$. Due to the fermionic anti-commutation relations all terms here cancel. Equally, if one sets APBC, $a_{L+j} = -a_j$, with $r = L - 1$ all hopping terms cancel. This is clearly not capturing the physics that we are interested in, so instead restrict to $r < \frac{L}{2}$ and L odd. Only then is it possible to see equal couplings between all sites, without cancellations or redundancies, see Fig. 3.1. Note that with even L it is

[1] Each of these cases give an identical chain with nearest neighbour hopping and pairing only; however, by choosing different scaling parameters we may independently probe the different contributions to the behaviour of the long-range chain.

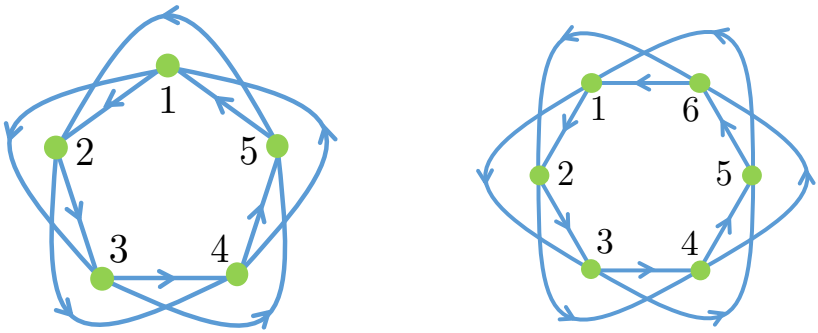

(a) (b)

Figure 3.1: A sketch of the maximal extent of long-range couplings for an (a) odd length and (b) an even length chain with closed boundaries. In (a) every site is connected to every other site. In (b) sites j and $j+L/2$ are not connected for any j as hermitian conjugate terms of the Hamiltonian result in cancellations for both PBC and APBC. To remove this effect we choose to study odd length chains only.

not possible to couple the j and $j+\frac{L}{2}$ sites. Though the effect of this missing coupling is negligible, in this work whenever PBC are enforced we use odd length chains.

3.2.2 Bloch Hamiltonian

To probe this model further it is worth making use of the translational invariance of the model, i.e. invariance under translation of lattice indices, and use a Fourier transformation to momentum space as we did with the local model. Using a Fourier transformation, Hamiltonian (3.1) becomes

$$\begin{aligned} H &= \sum_k \begin{pmatrix} a_k^\dagger & a_{-k} \end{pmatrix} \begin{pmatrix} \frac{\mu}{2} + J\sum_l^r \frac{1}{l^\alpha}\cos(\phi_l l - kl) & -i\Delta\sum_l^r \frac{1}{l^\beta}\sin(kl) \\ i\Delta\sum_l^r \frac{1}{l^\beta}\sin(kl) & -\frac{\mu}{2} - J\sum_l^r \frac{1}{l^\alpha}\cos(\phi_l l - kl) \end{pmatrix} \begin{pmatrix} a_k \\ a_{-k}^\dagger \end{pmatrix} \\ &= \sum_k \psi_k^\dagger \mathcal{H}(k)\psi_k, \end{aligned} \tag{3.2}$$

where we have made use of the Dirac delta function $\delta_{k,k'} = \frac{1}{L}\sum_j e^{i(k-k')j}$ and $\mathcal{H}(k)$ is the BdG Hamiltonian. Taking into account PHS that gives a symmetric

distribution of energies about zero, the analytical expression for the bulk energy spectrum is

$$E^{\pm}_{\text{bulk}}(k) = \pm\sqrt{\left|\frac{\mu}{2} + J\sum_{l}\frac{\cos(\phi_l l - kl)}{l^{\alpha}}\right|^2 + \left|\Delta\sum_{l}\frac{\sin(kl)}{l^{\beta}}\right|^2}, \tag{3.3}$$

allowing one to define the energy gap as $E_{\text{gap}} = 2\min_k E^{+}_{\text{bulk}}(k)$.

Making use of a trigonometric identity, we see that $\cos(\phi_l l \pm kl) = \cos(\phi_l l)\cos(kl) \mp \sin(\phi_l l)\sin(kl)$ and can conveniently rewrite the BdG Hamiltonian as

$$\begin{aligned}\mathcal{H}(k) = \left[\Delta\sum_{l}\frac{\sin(kl)}{l^{\beta}}\right]\sigma_y - \left[\frac{\mu}{2} + J\sum_{l}\frac{\cos(\phi_l l)\cos(kl)}{l^{\alpha}}\right]\sigma_z \\ + \left[J\sum_{l}\frac{\sin(\phi_l l)\sin(kl)}{l^{\alpha}}\right]\mathbb{1}_2\end{aligned} \tag{3.4}$$

where σ_j are the 2×2 Pauli matrices and $\mathbb{1}_2$ is the identity. The effect of the complex hopping phase now becomes clear. TRS is conserved if $\mathcal{H}(-k)^* = \mathcal{H}(k)$. In Hamiltonian (3.4), the term proportional to the identity breaks this symmetry unless $\phi_l = 0, \pi$. Breaking TRS changes the topological invariant from a $\mathbb{Z}$ to a $\mathbb{Z}_2$ classification.

The physical relevance of breaking TRS can be interpreted in more than one way. First, we can think of a real system that could be prepared in the lab. In order to build a system of spinless fermions it is required that there is a strong magnetic field fixing the spin orientation of spinful fermions. TRS has the effect of flipping spins, but not the magnetic field. Therefore spins will not flip under TRS and it is therefore not an invariant. By including $\phi_l \neq 0, \pi$ we simulate this behaviour in Hamiltonian (3.1). Further, we can think about the effect TRS has on the momentum space single particle spectrum. If TRS is an invariant then the entire spectrum satisfies $\mathcal{H}(-k)^* = \mathcal{H}(k)$. The condition implies that at the points in the BZ that map to themselves $k = 0, \pi$, there is a time reversal state with the same energy. Thus TRS implies degeneracies in the energy spectrum, this is confirmed by Kramer's theorem [70] providing the system has half-integer total spin or $\mathcal{T}^2 = -1$. Degeneracies at time reversal invariant points can only be lifted by breaking the symmetry.

Another relevant symmetry is particle-hole symmetry – an anti-unitary operation transforming the Bloch Hamiltonian as $\mathcal{C}^{-1}\mathcal{H}(k)\mathcal{C} = -\mathcal{H}(k)$, where $\mathcal{C} = \sigma_x\mathcal{K}$ and $\mathcal{K}$ is complex conjugation [71]. The existence of both TRS and PHS implies a chiral symmetry, that is found upon the multiplication of TRS and PHS. This very general model is thus open to a wide range of physics through the different choices of parameter value. Let's expose some of its features through a winding number analysis.

3.2.3 Winding number analysis

For this study we use the winding number topological invariant introduced in Eq. (2.57) of the previous Chapter, with the definitions $\hat{h}(k) = \frac{h(k)}{|h(k)|} = (h_x, h_y, h_z)$ for $\mathcal{H}(k) = h(k)\cdot\sigma$ and $\sigma = (\sigma_x, \sigma_y, \sigma_z)^T$. For now, it is sufficient to plot h_z against h_y in order to identify when points in k-space populate the unit circle. In Fig. 3.2 we show the winding of $\hat{h}(k)$ for different parameter values, with $\phi_l = 0$, $\alpha = \beta = 0$ and $L = 2001$ sites. In all figures the points only populate a semi-circle and not the full unit circle, leading to an apparent half-integer winding number [67], even as the system size increased. By definition a winding number measures full rotations about the origin, so the applicability of the winding number here may be brought into question.

Figs. 3.2(a) and 3.2(b) contain points densely populating the upper hemisphere and also a single point at $h_z = -1$ $h_y = 0$. The existence of points at both the north and south pole of the unit circle indicates a topological phase as the winding vector is required to have made a full rotation about the origin. Though, this is not enough to accept that the topological phase exists with half-integer winding. Fig. 3.2(c) contains a single point in the lower hemisphere with all other points having $h_z = 0$; this can be identified as the phase transition, in agreement with the energy gap closing. Fig. 3.2(d) has all points densely populating the lower hemisphere with no points above the h_y axis. This is a signature of a trivial phase as the winding vector only covers half the unit circle, without the single point at the opposite pole.

Instead, one could use the TRS symmetry of the model to define a better topological invariant. As $h_y(k)$ is the sum of sin terms, when k is an integer value

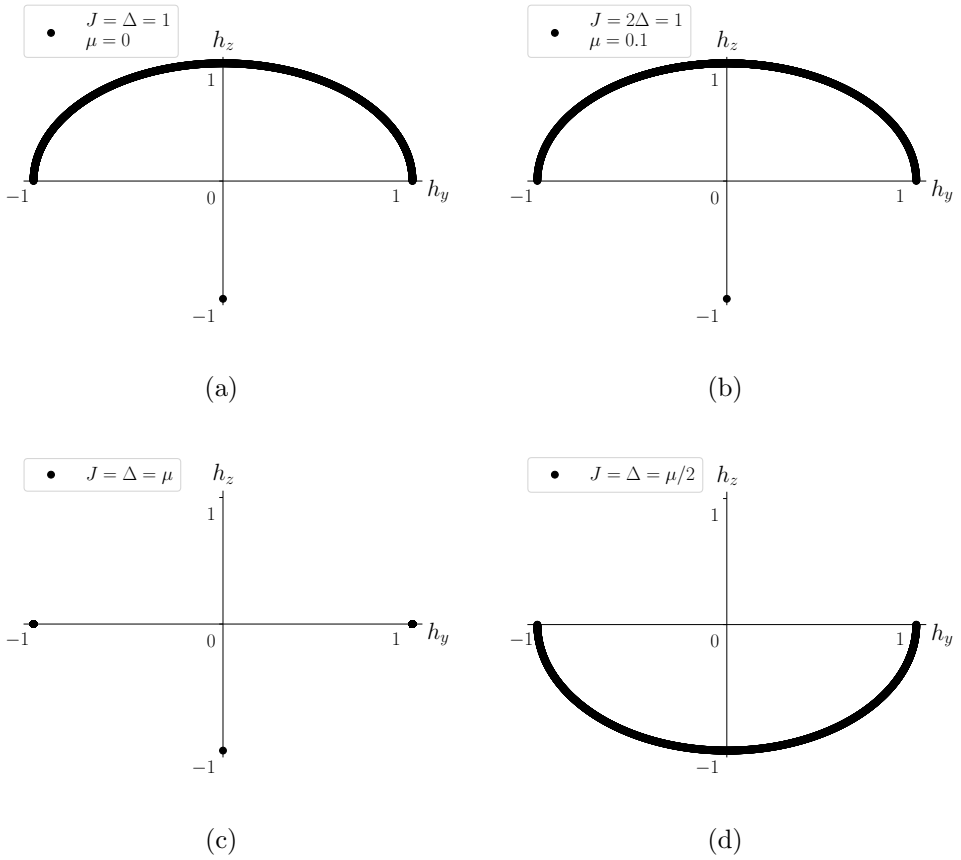

Figure 3.2: Winding of the Bloch Hamiltonian in k-space for the infinite-range model $\alpha = \beta = 0$ with $L = 2001$ sites, PBC, and TRS $\phi_l = 0$, for different points in the phase diagram. The values of J, Δ and μ are labelled on each figure. Such a large system size is taken here to demonstrate where the density of points lie about unit circle.

of π, then that component of the Bloch vector is zero. When TRS is present, so that $h(k)_x = 0$, the vector is parallel to the z-axis. There are two points in the BZ with this property, i.e. $k \in [0, \pi]$. In order for the the path taken by the Bloch vector to be deformable to a full circle about the origin, it must pass through the north and south pole at the 0 and π points. Therefore define a topological invariant to be

$$\nu = \mathrm{sgn}[h_z(0)h_z(\pi)]. \tag{3.5}$$

When $\nu = -1$ there is a non-zero winding as the vector must pass through both poles. When $\nu = 1$ the vector draws out a path that passes over the same pole at both k points and is therefore a trivial phase with zero winding. This $\mathbb{Z}_2$ invariant appropriately characterises the system also with broken TRS as shown in [69] that results in the winding vector having three non-zero components.

To see why the winding number is not well behaved in the infinite limit, it is useful to plot the winding vector away from $\alpha = \beta = 0$ and with a reduced range of r. In Fig. 3.3 the winding vector is shown for different choices of r, α and β. In (a) the winding vector is plotted with power-law decaying couplings, with r extending to its maximal value of $\frac{L-1}{2}$ and $\alpha = \beta = 0.5$. The winding vector now has points in the lower hemisphere, breaking the argument for a half-integer winding. Though they still do not densely cover the entire circle, this result suggests that the long-range couplings affect the distribution of points along h_z. In (b) the winder vector is plotted with a reduced range r and without decay, $r = \frac{L-1}{2} - 1$ and $\alpha = \beta = 0$. Now, even with only a single r value less than what is plotted in Fig. 3.5, the vector densely populates the entire unit circle making a single revolution about the origin. If the $L \to \infty$ limit is taken, with also $r \to \infty$, it is found that $h_z(k)$ is constant for all values of k. It is therefore necessary to take the limit $L \to \infty$ before $r \to \infty$ (without the gap closing) to arrive at a reliable result for the winding number.

As an alternative approach, one could investigate a different choice of boundary condition that may probe different points in momentum space. For example, with a twisted boundary condition the first and last sites of an open chain are coupled up to an overall phase, e.g. if periodic boundaries has coupling J between the ends, then twisted boundaries has coupling $Je^{i\Theta}$ between ends with $\Theta \in \mathbb{R}$ and defined modulo 2π. Anti-periodic boundaries are found by setting $\Theta = \pi$. Including a twisted boundary condition has the effect of allowing for values of lattice momenta $k = \frac{2n\pi}{L}$ with $n \notin \mathbb{Z}$, that may populate the unit circle in regions where $\Theta = 0, \pi$ does not. This is an interesting point that would be insightful to explore in future work.

In order to definitively prove the existence of topological phase, beyond the arguments given above, we aim to find an analytical solution for the infinite range model with OBC. In doing so, we hope to find exponentially localised Majorana

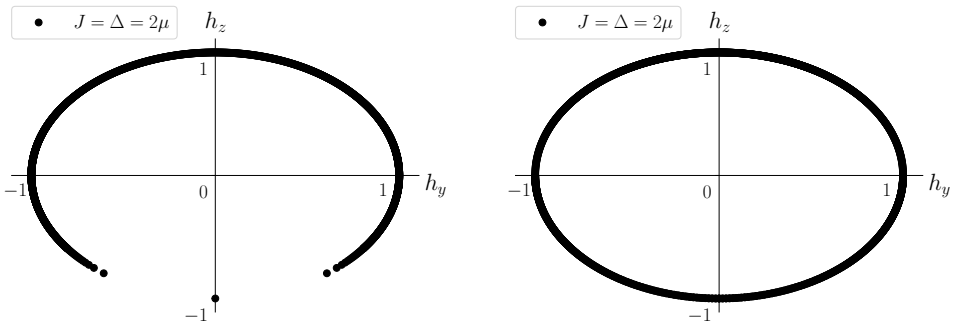

(a) (b)

Figure 3.3: Winding of the Bloch Hamiltonian in k-space with $J = \Delta = 2\mu = 1$, $L = 2001$, $\phi_l = 0$ and (a) $\alpha = \beta = 0.5$, $r = \frac{L-1}{2}$ (b) $\alpha = \beta = 0$, $r = \frac{L-1}{2} - 1$. From (a) it is clear that allowing for a power-law decay extends the density of points from the upper hemisphere in the lower hemisphere. However, from (b), points populate the entire circle if the range of interactions is reduced only slightly from its maximum value.

edge modes that are gapped away from the lowest energy bulk modes, given by Eq. (3.3). By probing directly the infinite range chain with open boundaries we may expose Majoranas in the most extremal case of Eq. (3.1), whilst bypassing the requirement for taking limits in a particular order to achieve a sensible result.

3.3 Analytical solution of the infinite range model

3.3.1 Forming a recursion relation for particle amplitudes

In order to show the existence of edge modes we obtain a full analytical solution for the infinite range model, setting $\alpha = \beta = 0$ with OBC and $\phi_l = 0$. The Hamiltonian becomes

$$H = \sum_{j=1}^{L-1} \sum_{l=1}^{L-j} \left(J a_j^\dagger a_{j+l} + \Delta a_j a_{j+l} + \text{h.c.} \right) + \sum_{j=1}^{L} \mu a_j^\dagger a_j \tag{3.6}$$

Without translational invariance it is not possible to use the momentum space representation as presented in the previous section that lends itself to winding

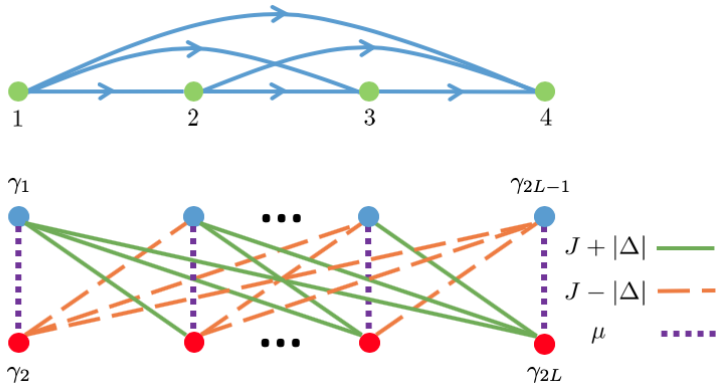

Figure 3.4: (Top) Pictorial representation of the infinite range chain in the fermionic representation with OBC and $L = 4$ sites. While tunnelling couplings create a fully connected graph, the pairing couplings encode direction that preserves the one-dimensional character of the model. (Bottom) Visualising the Hamiltonian in a Majorana representation with operators, γ_{2j-1} (blue) and γ_{2j} (red), the one-dimensional (and not zero or many-dimensional) character becomes clear. Lines represent terms in the Hamiltonian: $J + |\Delta|$ (green, solid), $J - |\Delta|$ (orange, dashed) and μ (purple, dotted).

number calculations. However, we still want to show that the ground state is topological, i.e. that there exist elementary excitations that are exponentially localised to the boundary. By making a transformation to the Majorana representation and viewing the Hamiltonian graphically, see Fig. 3.4, it is clear that edge Majorana modes do exist, at least for some choice of the parameter values. Take for example $J = |\Delta|$ along with $\mu = 0$. The Hamiltonian reduces to $H = \frac{i}{2}\sum_{j,k} J\gamma_{2j-1}\gamma_{2k+2}$ that does not contain the operators γ_2 and γ_{2L-1}. Such a situation presents zero energy edge modes in the same way as the local Majorana chain. Likewise, choosing $J = -|\Delta|$ leaves zero energy edge modes localised at Majoranas γ_1 and γ_{2L}. It now remains to find the effect of tuning away from these special points.

We return to the fermionic representation for the following calculation and use a modified generating function method that has been used successfully for finding edge mode localisation properties in local models [72, 73, 74, 75]. Choose a general state $|\psi\rangle = \sum_{j=1}^{N} \chi_j^\dagger \psi_j |0\rangle$ to be an eigenstate of Hamiltonian (3.6) with

energy E, where $\chi_j^\dagger = \begin{pmatrix} a_j & a_j^\dagger \end{pmatrix}$ contains particle and hole creation operators with amplitude $\psi_j = \begin{pmatrix} \psi_j^A \\ \psi_j^B \end{pmatrix}$, that acts on the superconducting vacuum $|0\rangle$ (filled Fermi sea). To show existence of edge modes we want to find amplitudes that satisfy $|\psi_j|^2 \sim \exp\left[\frac{-j}{\xi}\right]$, where ξ is the edge mode localisation length characterising the exponential profile of the mode.

Using the Schrödinger equation and ensuring the boundary condition is satisfied, $\psi_{L+m} = \psi_{1-m} = 0$ for all $m > 0$, returns a recursion relation relating site j to all other sites of the chain

$$\sum_{l=1}^{L} \left[\Gamma_2 \psi_{j+l} + \Gamma_2^\dagger \psi_{j-l}\right] + (\Gamma_1 - 2E)\psi_j = 0, \tag{3.7}$$

where $\Gamma_1 = \begin{pmatrix} \mu & 0 \\ 0 & -\mu \end{pmatrix}$ and $\Gamma_2 = \begin{pmatrix} J & -\Delta \\ \Delta & -J \end{pmatrix}$ contain the coupling amplitudes. This is not particularly simple to solve as can be seen by rearranging: extracting information about any site j requires information from all other sites. This can be simplified greatly by considering instead the sum of amplitudes

$$\Psi_j = \sum_{m=j}^{L} \psi_m. \tag{3.8}$$

By taking differences of Eq. (3.8) it is simple to show that $\psi_j = \Psi_j - \Psi_{j+1}$ and also $\sum_k^j \psi_k = \Psi_1 - \Psi_{j+1}$. Therefore, substituting Eq. (3.8) into Eq. (3.7) results in

$$M\Psi_j + K\Psi_{j+1} + \Gamma_2^\dagger \Psi_1 = 0 \tag{3.9}$$

where $M = \Gamma_1 - \Gamma_2^\dagger - 2E$ and $K = \Gamma_2 - \Gamma_1 + 2E$. We now have a recursion relation that at first glance looks significantly simpler: to find information about term $j+1$ we only need information about term j and the first term.

3.3.2 From a recursion relation to a generating function

From a set of amplitudes $\{\Psi_j\}$ related by a recursion relation it is possible to define a generating function

$$G(z) = \sum_{j=1}^{L} z^{j-1} \Psi_j, \tag{3.10}$$

that generates each term by repeated differentiation, i.e. $\Psi_j = \frac{1}{(j-1)!}\frac{d^{(j-1)}}{dz^{(j-1)}}G(z)\Big|_{z=0}$, with $z \in \mathbb{C}$. To find a function of this form, multiply Eq. (3.9) by z^j and sum over all j. Then, following some rearranging we find

$$\begin{aligned}
0 &= \sum_{j=1}^{L}\left[z^j K\Psi_{j+1} + z z^{j-1} M\Psi_j + z^j \Gamma_2^\dagger \Psi_1\right] \\
0 &= \sum_{j=1}^{L}\left[z^{j-1} K\Psi_{j} + z z^{j-1} M\Psi_j + z^j \Gamma_2^\dagger \Psi_1\right] - K\Psi_1 \\
0 &= (K+zM)G(z) + \left[-K + \Gamma_2^\dagger \frac{z(1-z^L)}{1-z})\right]\Psi_1, \qquad (3.11)
\end{aligned}$$

where in the second line we let $j \to j-1$ and in the final line we use $\sum_j^L z^j = \frac{z(1-z^L)}{1-z}$ that is the closed form solution for the first L terms of a geometric series, providing $|z| < 1$ and with singular points at $|z| = 1$. We will see later that restricting to the domain $|z| < 1$ is an acceptable restriction for this problem. Of course, writing it in its unrestricted form $\sum_j z^j$ only exposes that it is divergent for all $|z| \geq 1$. The generating function is therefore given by

$$G(z) = (K+zM)^{-1}\left[K - \Gamma_2^\dagger \frac{z(1-z^L)}{1-z})\right]\Psi_1. \qquad (3.12)$$

To expose the generating function in all of its detail, expand $A = K + zM$ to find its inverse and let $\Psi_1 = \begin{pmatrix}\phi_1 \\ \phi_2\end{pmatrix}$. This results in

$$\begin{aligned}
G(z) = \frac{1}{\det A}&\begin{bmatrix}\Sigma(1-z) & \Delta(1+z) \\ -\Delta(1+z) & -\bar{\Sigma}(1-z)\end{bmatrix} \\
&\times\left[\begin{pmatrix}-\bar{\Sigma}\phi_1 - \Delta^*\phi_2 \\ \Delta\phi_1 + \Sigma\phi_2\end{pmatrix} - \frac{z(1-z^L)}{1-z}\begin{pmatrix}J\phi_1 + \Delta^*\phi_2 \\ -\Delta\phi_1 - J\phi_2\end{pmatrix}\right], \qquad (3.13)
\end{aligned}$$

where $\det A = [4E^2 - (J-\mu)^2](1-z)^2 + \Delta^2(1+z)^2$, $\Sigma = -J + \mu + 2E$ and $\bar{\Sigma} = -J + \mu - 2E$. From this generating function it is possible to analyse the case where there is a boundary at both sites 1 and L, and also the case where there is a single boundary at site 1 or L on a semi-infinite chain extending to $\pm\infty$. We will see that both cases are important to completely describe this model.

3.3.3 Ground state of a semi-infinite chain with a single boundary

Generating function conditions for edge modes

Let us first explore what is required of the generating function of a non-local chain in order to expose the topological nature of the ground state, i.e. the existence of edge modes. For the non-local, semi-infinite, chain we have defined the generating function in Eqs. (3.10) and (3.8). If it was defined more simply as $g(z) = \sum_{j=1}^{\infty} z^{j-1}\psi_j$ (as is the case when solving the local chain) then the following proposition would hold. It is presented in [72], also for completeness in [1], and will be presented here. It relates poles z_i of a rational generating function to the localisation of its terms. The generating function can be expressed explicitly as $g(z) = \sum_i \frac{f_i(z)}{(z-z_i)^{n_i}}$ with $f_i(z)$ a vector with entries containing polynomials in z and n_i the order of the pole z_i,

Proposition: A rational generating function, $g(z) = \sum_{j=1}^{\infty} z^{j-1}\psi_j$, corresponds to an edge mode, $|\psi_j|^2 \xrightarrow{j\to\infty} 0$, if and only if all the poles, z_i, of $g(z)$ have absolute values greater than one, $|z_i| > 1 \ \forall \ i$.

In order to understand this proposition, consider a generating function with a first order pole only. If $a, b \in \mathbb{C}$ are constants that do not depend on index, it follows that

$$g(z) = \frac{z_0}{z_0 - z}\begin{pmatrix} a \\ b \end{pmatrix} \tag{3.14}$$

$$= \frac{1}{1 - \frac{z}{z_0}}\begin{pmatrix} a \\ b \end{pmatrix} \tag{3.15}$$

$$= \sum_j \left(\frac{z}{z_0}\right)^j \begin{pmatrix} a \\ b \end{pmatrix}. \tag{3.16}$$

From the definition of the local generating function, i.e. $g(z) = \sum_{j=1}^{\infty} z^{j-1}\psi_j$, we have that $\psi_j = \frac{1}{z_0^{j-1}}\begin{pmatrix} a \\ b \end{pmatrix}$. Thus poles of the closed form generating function give

exactly the distribution of particle amplitudes across the chain. Therefore, either

$$|z_1| < 1 \quad \Longrightarrow \quad |\psi_j|^2 \xrightarrow{j\to\infty} \infty, \tag{3.17}$$

$$|z_1| = 1 \quad \Longrightarrow \quad |\psi_j|^2 = e^{ikj}, \tag{3.18}$$

$$|z_1| > 1 \quad \Longrightarrow \quad |\psi_j|^2 \xrightarrow{j\to\infty} 0, \tag{3.19}$$

corresponding to a diverging (or converging on the opposite boundary), a bulk or an edge mode solution respectively. More complicated generating functions can be reduced to this single pole problem. Of course, our generating function, Eq. (3.13), is defined in terms of Ψ_j's that correspond to sum's of amplitudes ψ_j, i.e. $\Psi_j = \sum_{k=j} \psi_k$, where ψ_j is a vector containing support for particles and holes. Due to the use of Ψ_j, the condition found above in Eq. (3.19) is not enough to probe the existence of edge modes. For that we must look a little deeper at $G(z)$. In the above, the spinor notation was introduced by simply including the vector $\begin{pmatrix} a \\ b \end{pmatrix}$ in the ansätze and carrying it through the calculation. In the following, for simplicity and without loss of generality, we drop the spinor notation.

To expose $G(z)$ in more detail use Eq. (3.19) as an ansätze, i.e. that $\psi_j = z_0^{-j}$ with $|z_0| > 1$ (up to normalisation). We may therefore rewrite the inner summation of $G(z) = \sum_{j=1}^{\infty} \sum_{k=j}^{\infty} z^{j-1} \psi_k$ as

$$\begin{aligned} \sum_{k=j}^{\infty} \psi_k &= \sum_{k=j}^{\infty} \frac{1}{z_0^k} \\ &= \frac{1}{z_0^j} \sum_{l=0}^{\infty} \frac{1}{z_0^l}, \\ &= \frac{1}{z_0^j} \frac{1}{z_0 - 1}, \end{aligned} \tag{3.20}$$

where on the second line we substitute $l = k - j$ and then use the closed form for the infinite geometric series $\sum_l z_0^{-l} = (z_0 - 1)^{-1}$, that is analytic for $|z_0| > 1$ and is singular at $z_0 = 1$. Substituting Eq. (3.20) back into the generating function

and rearranging gives

$$\begin{aligned} G(z) &= \sum_{j=1}^{\infty} \frac{z^{j-1}}{z_0^j} \frac{1}{z_0 - 1} \\ &= \frac{1}{z_0 - 1} \sum_{j=1}^{\infty} z^{j-1} \psi_j \\ &= \frac{1}{z_0 - 1} g(z), \end{aligned} \tag{3.21}$$

where $g(z) = \sum_{j=1}^{\infty} z^{j-1}\psi_j$ must satisfy the condition found in Eq. (3.19). It is clear that the $z_0 = 1$ pole does not affect the localisation properties of ψ_j as these are contained entirely in $g(z)$. The $z_0 = 1$ pole is an artefact of the infinite range couplings.

Existence of edge modes

To continue, we now need to check the poles of Eq. (3.13) to find under which conditions they satisfy Eq. (3.19), that result in an edge mode. We should also be able to extract other properties of the edge mode, for example how fast it decays into the bulk, as this is related to the specific poles of $G(z)$. The poles are the two solutions $z_{1,2}$ of the quadratic $\det A = 0$. Vieta's formula states that for a quadratic equation $ax^2 + bx + c = 0$ with $x \in \mathbb{C}$, then its roots must satisfy $x_1 x_2 = c/a$ and $x_1 + x_2 = -b/a$. Making use of the first of these relations and realising that in our case $c = a$, we see that $z_1 z_2 = 1$. This leaves three choices: (i) $|z_1| = |z_2| = 1$, (ii) $|z_1| = \frac{1}{|z_2|} > 1$ or (iii) $|z_1| = \frac{1}{|z_2|} < 1$. For an edge mode we require either (ii) or (iii) and need to ensure that the pole less than one is cancelled with a zero in the numerator of $G(z)$, to satisfy Eq. (3.19).

We can simplify $G(z)$ by focusing on the region $|z| < 1$ (as this is where we find the pole that we wish cancel) so that $z^L \to 0$. Then, exposing the generating function in its full form gives

$$G(z) = \frac{1}{(1-z)\det A} \left[(1-z)P(z) - zQ(z)\right] \tag{3.22}$$

with $P(z)$ and $Q(z)$ both linear in z,

$$P(z) = \begin{bmatrix} -\Sigma(\bar{\Sigma}\phi_1 + \Delta^*\phi_2)(1-z) + \Delta^*(\Delta\phi_1 + \Sigma\phi_2)(1+z) \\ \Delta(\bar{\Sigma}\phi_1 + \Delta^*\phi_2)(1+z) - \bar{\Sigma}(\Delta\phi_1 + \Sigma\phi_2)(1-z) \end{bmatrix} \tag{3.23}$$

$$Q(z) = \begin{bmatrix} \Sigma(J\phi_1 + \Delta^*\phi_2)(1-z) - \Delta^*(\Delta\phi_1 + J\phi_2)(1+z) \\ -\Delta(J\phi_1 + \Delta^*\phi_2)(1+z) + \bar{\Sigma}(\Delta\phi_1 + J\phi_2)(1-z) \end{bmatrix}, \tag{3.24}$$

so that the numerator of $G(z)$ is at most quadratic in z. In order to cancel the $|z_j| < 1$ pole for the entire generating function the rows of $(1-z)P(z) + zQ(z)$ must be proportional, to cancel with $(z - z_j)$. To do so, and to also find the specific conditions for when the rows are or are not proportional, it is possible to form proportionality relations between the coefficients of 1, z and z^2. This results in three equations that may be solved for energy.

To be more clear, take the general form of the generating function to be $G(z) = \frac{1}{(z-z_1)(z-z_2)(1-z)} \begin{pmatrix} az^2 + bz + c \\ dz^2 + ez + f \end{pmatrix}$. Say $|z_1| < 1$, then for an edge mode we require the factorisation $az^2 + bz + c = f(z)(z - z_1)$ where the function $f(z)$ is linear in z and likewise for the bottom row, with the factorisation $dz^2 + ez + f = g(z)(z - z_1)$. Clearly multiplying the top row by $g(z)/f(z)$ gives the bottom row, so comparing coefficients of z^2, z and 1 we can form relations $a = \frac{g(z)}{f(z)}d$, $b = \frac{g(z)}{f(z)}e$, and $c = \frac{g(z)}{f(z)}f$. Then, rearranging for $\frac{g(z)}{f(z)}$ results in the following equalities requiring to be satisfied $\frac{a}{d} = \frac{b}{e} = \frac{c}{f}$.

Using this procedure, reading the values $a, b, \ldots, f$ from Eq. (3.22) along with Eqs. (3.23) and (3.24), it is found that the only valid solution satisfying the proportionality relations is one of zero energy $E = 0$ along with the conditions $\phi_1 = \pm e^{-i\theta}\phi_2$ and $|\Delta| \neq 0$, where θ is the complex phase of the superconducting parameter $\Delta = e^{i\theta}|\Delta|$. To ensure that this corresponds to an edge mode localising at site 1, fix the remaining singular point, z_2, to have an absolute value greater than 1. This gives the condition:

$$\mu < J. \tag{3.25}$$

Thus in the infinite range model we see a reduction by a factor of two in the value of chemical potential for which the model becomes critical, compared with the nearest neighbour model. The infinite-range model has a topological phase that is less robust than the local model, though it may be closer to physical in

small systems where decaying couplings may appear close to infinite range over the size of system.

Form of zero energy edge modes

In addition to finding the condition for the existence of zero modes, we can use this approach to find the form of the corresponding eigenstates. We have already seen in Eq. (3.12) that the generating function is proportional to the constant vector Ψ_1. It follows that all Ψ_j are also proportional to Ψ_1, as $\Psi_j = \frac{d^{(j)}G(z)}{dz^{(j)}}\Big|_{z=0} \propto \Psi_1$. It is therefore clear that each ψ_j is also proportional to Ψ_1 as ψ_j is found as the difference of two consecutive sums, i.e. $\psi_j = \Psi_j - \Psi_{j+1} \propto \Psi_1$. From Eq. (3.19) we know that the single-site amplitudes must decay with the remaining $|z_2| > 1$ pole; hence, the ground state is constructed by terms like

$$\psi_j = \Psi_j - \Psi_{j+1} \sim |z_2|^{-j} \begin{pmatrix} \pm e^{-i\theta} \\ 1 \end{pmatrix}, \tag{3.26}$$

up to normalisation. For $|z_2| < 1$ the mode will localise at a $j = N$ boundary of a semi-infinite chain that extends to $-\infty$, as per the condition in Eq. (3.17).

From the explicit expression found in Eq. (3.26) it is possible to find the *localisation length*, ξ, that quantifies the exponential profile of the edge mode. It is defined by $\psi_j \sim e^{-j/\xi}$, that gives $\xi = \frac{1}{\ln|z_2|}$. As one approaches a the phase transition, i.e. $J = \mu$, we expect the localisation length to diverge whilst the edge mode loses its exponential profile. Explicitly, the remaining pole is given by

$$z_2 = \frac{-|\Delta|^2 - (J-\mu)^2 + 2|\Delta|(J-\mu)}{|\Delta|^2 - (J-\mu)^2}. \tag{3.27}$$

As $\mu \to J$ from below, it is clear that the absolute value of the singular point approaches one from above, $|z_2| \to 1$, and $\xi \to \infty$ as expected.

Following this explicit treatment we have shown that Hamiltonian (3.6) does indeed host a zero-energy edge mode, providing the system is constructed on a semi-infinite geometry. It is a unique, spectrally isolated state, which is both an eigenstate of the Hamiltonian and of the particle-hole operator $\mathcal{P} = \mathcal{K}\sigma_2$, where $\mathcal{K}$ is complex conjugation and σ_2 the second Pauli matrix. That it is spectrally isolated follows from the existence of a bulk gap separating the remaining energy levels from it. Uniqueness follows from there being only a single boundary

and therefore a single edge mode, compared with a chain with two boundaries where there exist exactly two zero energy edge modes in the infinite system limit. These properties ensure the Majorana edge state is fixed to $E = 0$. If the system is deformed away from the exactly solvable point by a series of unitary operations (local or not) that commute with particle-hole symmetry, this property is preserved as long as the energy gap does not close. Hence, the edge mode (3.26) is topologically stable in the same way as the edge modes of the local Kitaev chain [12]. It now remains to include a second boundary at $j = L$ and to find under what conditions the model is in a topological phase.

3.3.4 Ground state of a finite chain with two boundaries

We now want to determine if a finite chain with infinite range couplings can support edge modes. We first make an intuitive analysis. Returning to the local chain, we know that exact zero-energy edge modes exist when $J = \pm|\Delta|$ or when $L \to \infty$. If L is allowed to be finite, and $J \neq \Delta$, we find that an edge mode exists at each boundary that weakly interact under some effective Hamiltonian, with an interaction that is exponentially suppressed with system size [12]. This interaction results in a small energy shift (such that there remains a finite gap separating the two modes from any bulk modes) that preserves particle-hole symmetry – one mode is shifted in the positive E direction, the other by the same amount in the negative E direction. As the system size increases the interaction will reduce and the edge modes approach zero energy. This shift in energy does not affect the topological phase, as one could adiabatically tune the system size without the energy gap closing. Further, fluctuations between edge modes localising at a single boundary require that a physical non-zero energy mode will have support over both boundaries. For the infinite range chain sites 1 and L are coupled for all system size. Intuitively, we may therefore expect the edge modes to have a non-zero energy for any system size and to have support at both edges.

Generating function conditions for edge modes

It is now the aim to determine whether the model remains topological when the second boundary is introduced. We take the generating function in Eq. (3.13)

with L finite. Like the previous analysis, we must first study the divergences of $G(z) = \sum_{j=1}^{L} z^{j-1}\Psi_j$ with $\Psi_j = \sum_{k=j}^{L} \psi_k$ in order to find what conditions are required that result in edge modes. It would certainly be incorrect to assume that the generating function for the finite chain obeys the same set of divergences as the semi-infinite chain – as we see that the generating function has a slightly different definition.

Unlike the previous analysis, for a finite size system there exist two transformations of the Hamiltonian that impose conditions on the ground state, and will simplify the calculation. Upon reflecting the chain about its centre, $j \to L-j+1$ with $l \to -l$, and also letting $a_j \to -a_j$, $a_j^\dagger \to a_j^\dagger$ the Hamiltonian transforms as $H \to -H$, that give $\psi_j^A = -\psi_{L-j+1}^A$ and $\psi_j^B = \psi_{L-j+1}^B$. This transformation imposes the condition $\phi_1 = \sum_j^L \psi_j^A = 0$. A second possible transformation includes a reflection, along with $a_j \to a_j$ and $a_j^\dagger \to -a_j^\dagger$, that also transform the Hamiltonian as $H \to -H$, that give $\psi_j^A = \psi_{L-j+1}^A$ and $\psi_j^B = -\psi_{L-j+1}^B$. This transformation imposes $\phi_2 = \sum_j^L \psi_j^B = 0$. While these symmetries are not needed to determine the edge modes in a local chain, they are necessary for the infinite range chain. Armed with these transformations we turn to the form of the generating function given in Eq. (3.10).

First we see that the sums of amplitudes can be broken up into parts, i.e.

$$\Psi_j = \sum_{k=1}^{L} \psi_k - \sum_{k=1}^{j} \psi_k + \psi_j. \tag{3.28}$$

Thus, the generating function can be split up into terms

$$G(z) = \sum_{j=1}^{L} z^{j-1} \sum_{k=1}^{L} \psi_k - \sum_{j}^{L} \sum_{k=1}^{j} z^{j-1}\psi_k + \sum_{j}^{L} z^{j-1}\psi_j. \tag{3.29}$$

Following our intuitive understanding of the non-local chain (and from the symmetry conditions found for the Hamiltonian above) we expect that a single mode must localise at both boundaries, decay with equal amplitudes and be symmetric about the centre. The mode must therefore be invariant under the transformation $j \to L - j + 1$. This motivates the choice of ansätze to be $\psi_j = z_1^{-j} + z_1^{j-L-1}$, with $|z_1| > 1$, so that the decay of ψ_j is the same as ψ_{L-j+1}. Any relative phase between the terms in this ansätze destroys breaks the $j \to L - j + 1$ invariance

of ψ_j. Note that there also remains intrinsic particle and hole support in this ansätze that has been dropped for simplicity. It is possible to make the spinor dependence more explicit by including a vector in the calculation; however, as with the similar calculation for an edge mode condition with a single boundary, we do not learn anything new from its inclusion. The generating function becomes

$$G(z) = \frac{1-z^L}{1-z}\frac{z_1^{-L}-1}{1-z_1} + \frac{z_1^{-L}}{1-z_1}\frac{1-(zz_1)^L}{1-zz_1} + \frac{1}{z_1-1}\frac{1-(zz_1^{-1})^L}{1-zz_1^{-1}}. \tag{3.30}$$

For large system sizes $\lim_{L\to\infty} z_1^{-L} \to 0$, so $G(z)$ becomes in the large system size limit

$$G(z) \approx \frac{1-z^L}{1-z}\frac{1}{z_1-1} + \frac{1}{z_1-1}\frac{1-(zz_1^{-1})^L}{1-zz_1^{-1}}. \tag{3.31}$$

It is clear that poles exist for $z = 1$ and $z_1 > 1$. Studying the divergences further gives that as

$$z \to 1 \qquad G \to \frac{L}{z_1-1} + \frac{1}{(z_1-1)(1-z_1^{-1})}, \tag{3.32}$$

$$z \to z_1 \qquad G \to \frac{z_1^L-1}{(1-z_1)^2} + \frac{L}{z_1-1}. \tag{3.33}$$

So, the $z = z_1$ pole diverges exponentially with L compared with the $z = 1$ pole that diverges polynomially with L. For $z_1 = 1$ the generating function has poles for all z and is a critical point.

Existence of hybridised edge modes

We may now apply the symmetry and divergence conditions described in the previous section to the physically relevant generating function, Eq. (3.13). We know that it is required to remove the $|z| < 1$ pole so, like we did previously, focus on this region so that $z^L \to 0$ whilst the $z = 1$ pole remains present, as necessary. Next, we impose either $\phi_1 = 0$ or $\phi_2 = 0$. Begin with $\phi_1 = 0$; then, the generating function becomes

$$G_1(z) = X\begin{bmatrix} z^2\Delta^*(J-\Sigma) + z\Delta^*(J+\Sigma) \\ z^2\bar{\Sigma}(J-\Sigma) + z(2\Sigma\bar{\Sigma} - \bar{\Sigma}J + |\Delta|^2) + (|\Delta|^2 - \Sigma\bar{\Sigma}) \end{bmatrix}, \tag{3.34}$$

where $X = \frac{\phi_2}{(1-z)\det A}$. The top row has the factors $z = 0$ and $z = \frac{J+\Sigma}{J-\Sigma}$. Choosing $z = 0$ as a pole does not give the desired condition for an edge mode – there will still exist poles greater than and less than one. Therefore, we choose $z \neq 0$ factor to cancel the pole by setting it as a factor of the bottom row. Rearranging the result gives immediately one energy solution. If we choose to impose the $\phi_2 = 0$ condition we arrive at the second energy solution. The two solutions are

$$E_{\pm} = \pm \frac{J-\mu}{2} \frac{J^2 - |\Delta|^2}{J^2 + |\Delta|^2}. \tag{3.35}$$

Of course, that the Hamiltonian is particle-hole symmetric means that we only need to impose one of the conditions, $\phi_1 = 0$ or $\phi_2 = 0$, in order to deduce the second solution; however, it is simple enough to perform this check to be complete. Upon demanding that the remaining pole has an absolute value greater than one gives the edge mode condition to be $\mu < J$, giving the same condition as the semi-infinite chain with a single boundary. This condition holds for both energy solutions.

Form of hybridised edge modes

Finally, we are able to determine the localisation properties of the edge mode using the ansätze fixed above, i.e. $\psi_j = z_1^{-j} + z_1^{j-L-1}$. We know that the mode must localise at both boundaries and decay into the bulk with the remaining pole z_1 that lies outside of the unit circle. We also know that either $\phi_1 = 0$ or $\phi_2 = 0$ depending on the mode of interest. Beginning with $\phi_1 = 0$ that corresponds to E_+, the condition fixes that at one end of the chain $\psi_j \sim \begin{pmatrix} a \\ 1 \end{pmatrix}$ whereas at the other end $\psi_{L-j+1} \sim \begin{pmatrix} -a \\ 1 \end{pmatrix}$, where the free component has been set to 1 and a is to be determined.

In order to find a we note that local amplitudes are extracted using $\psi_j = \Psi_j - \Psi_{j+1}$ and each Ψ_j is proportional to Ψ_1. The generating function is also proportional to Ψ_1 for any z. Properties of the edge mode are found by approaching the divergences of the generating function. Considerable simplifications are found by allowing $z \to 1$, for which the dominant term is linearly diverging with

system size:

$$\lim_{z\to 1} G(z) = CL \begin{pmatrix} J \\ \Delta^* \end{pmatrix} \tag{3.36}$$

where C is contains other terms of the generating function not relevant to Ψ_1. To be consistent with our ansätze, we may now immediately write down the unnormalised edge mode amplitude as

$$\psi_j^+ \propto z_2^{-j} \begin{pmatrix} \frac{J}{\Delta^*} \\ 1 \end{pmatrix} + z_2^{j-L-1} \begin{pmatrix} \frac{-J}{\Delta^*} \\ 1 \end{pmatrix}, \tag{3.37}$$

where $z_2 = \frac{2E_+ + 2J - \mu}{2E_+ - \mu}$ is the inverse of the cancelled pole.

Similarly we could have taken the negative energy solution along with $\phi_2 = 0$ giving

$$\psi_j^- \propto z_2^{-j} \begin{pmatrix} 1 \\ \frac{J}{\Delta} \end{pmatrix} + z_2^{j-L-1} \begin{pmatrix} 1 \\ \frac{-J}{\Delta} \end{pmatrix}, \tag{3.38}$$

where the remaining pole is of a similar form but with the negative energy solution $z_2 = \frac{2E_- + 2J - \mu}{2E_- - \mu}$.

Following this analysis, it is clear that the localised edge modes have non-zero energies due to a direct coupling between the edges that is present for all system sizes of the infinite range chain. This direct coupling has the effect of *hybridising* the edge modes, such that they have support at both edges as evidenced by Eqs. (3.37) and (3.38) [67, 69]. Note that when the parameters take values $J = \pm|\Delta|$ and $\mu = 0$ the edge modes have zero energy, as given by Eq. (3.3.4), and the amplitudes $\psi^{\pm}$ ultra-localise at sites 1 and L.

Further to an analytical treatment of the edge modes, it is possible to probe numerically the topological nature of the non-local chain: through the eigenstates themselves, the use of a topological invariant, and the entanglement spectrum.

3.4 Numerical analysis of the non-local chain

3.4.1 Topological Invariant

Symmetry classification

The non-local (and local) Majorana chain lives in symmetry class BDI of the Altland-Zirnbauer classification table [45, 76], presented in Table 2.2.3, due to the

presence of particle-hole and time-reversal symmetries that imply also sub-lattice symmetry. To see this for the infinite range chain with OBC, we could calculate explicitly the form of the symmetries $\mathcal{T}$, $\mathcal{C}$, and $\mathcal{S}$ through their action on the second quantised operators in Eq. (3.6), to determine whether they are invariant and to find the sign of the symmetries squared. Alternatively, if the system can be deformed from infinite range couplings to the local chain without the energy gap closing then it must be in the same phase. We saw in Chapter 2 that local chain with PBC is in class BDI. This classification extends to the local chain with OBC through bulk-boundary correspondence. Later in this chapter, in Fig. 3.6, we plot the ground state and first excited state energies for a long-range system, showing that the gap does not close as couplings are tuned with a power-law decay $1/r^{\alpha}$ from $\alpha = 0$ to $\alpha \to \infty$. The system therefore hosts the same topological phase as the local chain and lives in the BDI symmetry class with a $\mathbb{Z}$ topological invariant. However, we have seen that a $\mathbb{Z}_2$ classification is sufficient for the local chain. This corresponds to two distinct phases that are connected through the closing of the excitation gap. The phases are distinguished by their fermion parity: the trivial phase has an even number of fermions and the topological has an odd number, where the difference follows from the reduction in fermion number by one to create of a pair of edge modes [12]. Following the analytical treatment in the previous section, that resulted in bi-localised Majorana edge modes presented in Eqs. (3.37) and (3.38) together with the constraint found below Eq. (3.3.4), it is clear that there exist topological and trivial phases in the long range model that differ by fermionic parity. It would therefore be useful to probe this phase with an invariant in a similar way to the local chain.

If it were possible to close the infinite range chain then we could define a winding number topological invariant, where a non-trivial value directly implies a topological phase and therefore the existence of edge Majoranas on the open chain due to bulk-boundary correspondence. However, as we saw at the beginning of this chapter, it is not possible to close the (truly) infinite range chain without losing terms in the Hamiltonian, for finite system sizes. For this case, we require an invariant that can be evaluated for an open chain. The Pfaffian invariant $\mathcal{M}$ may be used for both open and closed chains and measures the fermion parity $(-1)^{N_F} = \pm 1$, where N_F is the total fermion number that is invariant modulo

2 [12]. We now briefly review some properties of the Pfaffian to understand why it is a useful tool for measuring parity and thus also the presence (or not) of a topological phase.

The Pfaffian invariant

For a skew-symmetric matrix A, i.e. $A^T = -A$, the Pfaffian of A is given by the square root of its determinant $\mathrm{Pf}(A)^2 = \det A$ and is related to fermion parity by its sign $\mathcal{M}(A) = \mathrm{sgn}[\mathrm{Pf}(A)]$. An important property of $2n \times 2n$ real skew-symmetric matrices is that their eigenvalues appear in complex conjugate pairs $\{\pm i\lambda_j\}_j^n$, where $\lambda_j \in \mathbb{R}$. As the determinant of a matrix is just the product of its eigenvalues and the product each conjugate pair $\pm i\lambda_j$ is non-negative$\lambda_j^2 \geq 0$, then the determinant is also non-negative. Thus, the Pfaffian of A lies somewhere on the real line $\mathrm{Pf}(A) \in \mathbb{R}$ and in terms of the eigenvalues of A is given by $\mathrm{Pf}(A) = \pm \prod_j^n |\lambda_j|$.

Consider the local Majorana chain with PBC. In that case, providing the superconducting term of the Hamiltonian is non-zero, then all eigenvalues of the single-particle Hamiltonian are non-zero with an energy gap separating the occupied from unoccupied states. An exception to this occurs at the phase transition when the gap closes, changing the topological phase. Therefore, at the phase transition the determinant is zero. However, when the gap reopens the determinant will not change sign as it is non-negative, so it does not distinguish between phases the different phases. Assuming there exists a skew symmetric representation of the local Majorana chain, then its Pfaffian will differ in sign on either side of a phase transition as it tracks the level crossing at the gap closing point. Let's look a little closer at its definition.

Formally, it is defined in terms of permutations π_α of the elements of $A = \{A_{i,j}\}$, with $\alpha \in \Pi$ the set of all different permutations. By partitioning the indices $1, 2, \ldots, 2N$ into unordered pairs $\alpha = \{(i_1, j_1), (i_2, j_2), \ldots, (i_N, j_N)\}$, where $i_n < j_n \ \forall\ n = 1, \ldots, N$ and $i_1 < i_2 < \cdots < i_N$, then the permutation is given by

$$\pi_\alpha = \begin{bmatrix} 1 & 2 & 3 & 4 & \ldots & 2N-1 & 2N \\ i_1 & j_1 & i_2 & j_2 & \ldots & i_N & j_N \end{bmatrix}. \tag{3.39}$$

From this, the Pfaffian is

$$\mathrm{Pf}(A) = \sum_{\alpha \in \Pi} A_\alpha \tag{3.40}$$

where $A_\alpha = \mathrm{sgn}(\pi_\alpha) A_{i_1,j_1} A_{i_2,j_2} \dots A_{i_N,j_N}$.

For the case of Hamiltonian (3.6) written in terms of Majorana operators, $H = \frac{i}{2} \sum A_{j,k} \gamma_j \gamma_k$, the matrix A is skew-symmetric and can be brought into block-diagonal form via a real orthogonal transformation W,

$$WAW^T = \mathrm{diag}_j \begin{bmatrix} 0 & \epsilon_j \\ -\epsilon_j & 0 \end{bmatrix}. \tag{3.41}$$

The $\pm\epsilon_j$ are the single particle energies that appear as complex conjugate pair eigenvalues of A. The rows of W are eigenvectors of A. Note that as a condition for using the Pfaffian it is required that there are no exact zero modes. In our case we find non-zero energy edge modes for all system sizes, so this condition is satisfied. Continuing, when written in this tridiagonal form the Pfaffian is simply $\mathrm{Pf}(WAW^T) = \prod_j \epsilon_j > 0$. Thus, the parity is $\mathcal{M}(A) = \mathrm{sgn}(\det W)$ as $\mathrm{Pf}(A)$ and $\det(W)$ are required to be the same sign to satisfy the property $\mathrm{Pf}(WAW^T) = \mathrm{Pf}(A)\det(W)$ [77].

Evaluating Eq. (3.40) for the non-local chain gives exact agreement with the analytically found result, see Fig. 3.5. For $\mu < J$ the parity returns a non-trivial value, $\mathcal{M} = -1$, whilst the edge modes are non-zero, in agreement with our result from the generating function analysis, Eq. (3.3.4), and separated from bulk modes by the presence of a finite gap. For $\mu > J$ the parity returns a trivial value, $\mathcal{M} = +1$, and there is no gap separating the lowest energy states from the first excited states.

3.4.2 The entanglement spectrum of a long-range Majorana chain away from infinite range couplings

Entanglement spectrum from a flatband Hamiltonian

The entanglement spectrum was introduced in section 2.3 as a fingerprint for different phases of matter. The aim now is to find what characteristics the entanglement spectrum of a long-range model have and whether we can probe the

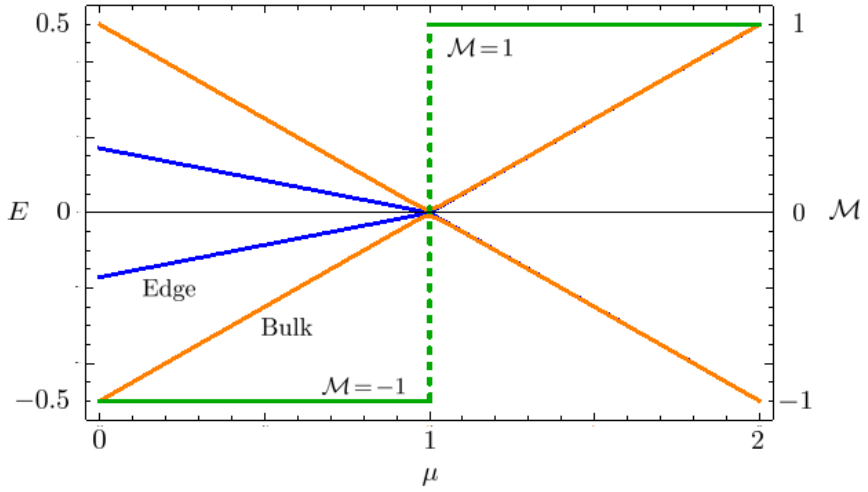

Figure 3.5: Varying chemical potential μ for $J = 1$, $\Delta = 0.7$ and $N = 100$, for the infinite range chain with OBC. Both the lowest four energy states (edge modes are blue, bulk modes are orange) and the parity (green) are plotted. For $\mu < J$ the edge modes are gapped from the bulk modes and the parity has a non-trivial value $\mathcal{M} = -1$. For $\mu = J$ the bulk gap closes as the system undergoes a phase transition. For $\mu > J$ the edge modes no longer exist and the parity reflects that with a trivial value $\mathcal{M} = +1$.

topological phase through their knowledge. The spectrum is found upon diagonalising the reduced density matrix $\rho = \mathrm{Tr}_B\,|\psi\rangle\langle\psi|$ of a state bipartitioned into regions A and B. The reduced density matrix has the form $\rho = e^{-H_E}$, where H_E is the entanglement Hamiltonian. Here we wish to probe the elementary single-particle excitations, so it is appropriate also study the single-particle entanglement spectrum $\{\epsilon_j\}$, that are the eigenvalues of the quadratic H_E^f.

In this study we extract the single-particle entanglement spectrum through the correlation matrix introduced in Chapter 2. It works for a system with a gapped bulk and midgap states in the single particle spectrum [78]. First, rewrite the single-particle correlation matrix as a the topologically equivalent flatband matrix $Q = \frac{\mathbb{1}}{2} - C$ with eigenvalues $\pm\frac{1}{2}$. It is topologically equivalent as one could continuously deform the gapped Hamiltonian to a flatband Hamiltonian without closing the gap. Then restrict to subsystem A by restricting $C \to C_A = \langle c_j^\dagger c_k\rangle$ with $j, k \in A$. The resulting matrix $Q_A = \frac{\mathbb{1}}{2} - C_A$ has eigenvalues $\lambda_j \in [-\frac{1}{2}, \frac{1}{2}]$.

But $C_A = (1 + e^{H_E^f})^{-1}$ so the eigenvalues λ_j are related to the single-particle entanglement spectrum ϵ_j by

$$\lambda_j = \frac{1}{2}\tanh\left(\frac{\epsilon_j}{2}\right), \tag{3.42}$$

with $j = 1, \ldots, L$. The values ϵ_j can be therefore be calculated directly from the correlation matrix of the single-particle eigenstates. Due to the presence of particle-hole symmetry and a gap in the full Hamiltonian (3.6), it is expected that there is a gap in the spectrum of Q_A and the levels come in pairs $\pm\lambda_j$ [51].

Numerical results for entanglement spectra

There are two different bipartition's that we may take for an open chain and both prove illuminating. One bipartition is a single cut separating the chain into left and right partitions, the other is two cuts where a middle partition is separated from boundary regions. We now compare properties of the physical spectrum and entanglement spectra against the local Majorana chain. It is most clear to plot the values λ_j, where all occupied(unoccupied) single-particle states sit around $-\frac{1}{2}(+\frac{1}{2})$, with topologically protected midgap states. If the midgap state has vanishing energy, $\epsilon \to 0$, then there are double degeneracies through the entire many-body entanglement spectrum.

Let's focus first on the case of a single partition separating the left and right sides of the chain, as in Figs. 3.6a and c. For the short range chain in (a), the entanglement Hamiltonian has a single virtual boundary at the partition, resulting in a single zero energy mode. This mode has its energy pinned to zero by PHS as there is no other midgap state to lift it from zero energy. The physical boundary does not couple with the virtual boundary as the system size is taken to be large, $L_A \gg \xi$ and both the physical boundary and virtual boundary are exponentially localised. For the long-range chain in (c), the spectrum has two midgap states split from zero energy. This implies that there is another edge state, the one at the physical boundary, overlapping with the virtual boundary at the partition. In Fig. 3.9, it is clear that this is because the virtual boundary has edge states that decay polynomially into the bulk, giving a non-zero overlap with the physical edge. The overlap is small as the physical edge mode decays

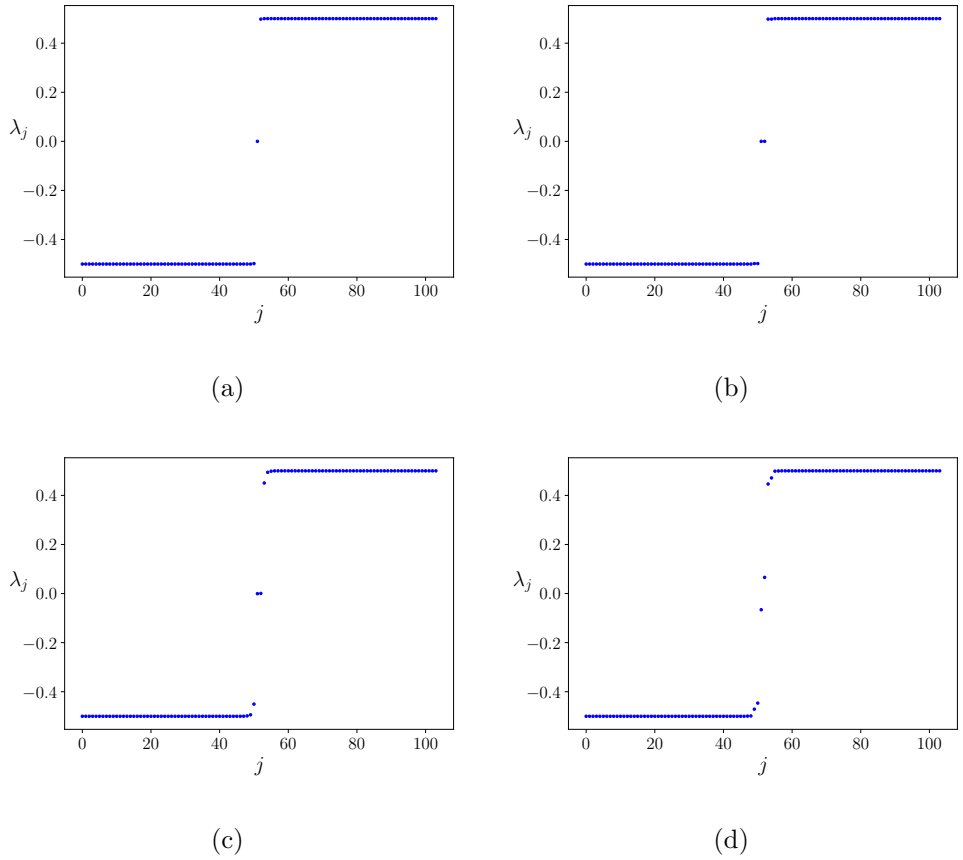

Figure 3.6: Entanglement spectra, parametrised as λ_j, of the (top) short range and (bottom) infinite range Majorana chain with $L = 100$, $\Delta = 0.7$, $\mu = 0.2$, and OBC. On the left, (a) and (c), shows a single partition of the system with subsystem A having 52 sites. On the right, (b) and (d), shows two partitions, where A has 52 sites with 21 sites to the left and 27 sites to the right. In all cases other than (c) the spectrum has a midgap state that corresponds to the virtual edge created by the partition. In (c), for the long-range chain with a single cut, there are two mid gap states due to a non-local coupling between the virtual edge and the physical edge.

quickly into the bulk. Thus, for very large system sizes the full entanglement spectrum should display degeneracies much like the local Majorana chain.

Next, turn to a partition such that region A is sandwiched by region B, as in Figs. 3.6b and d. Now there are two midgap states for both the short range

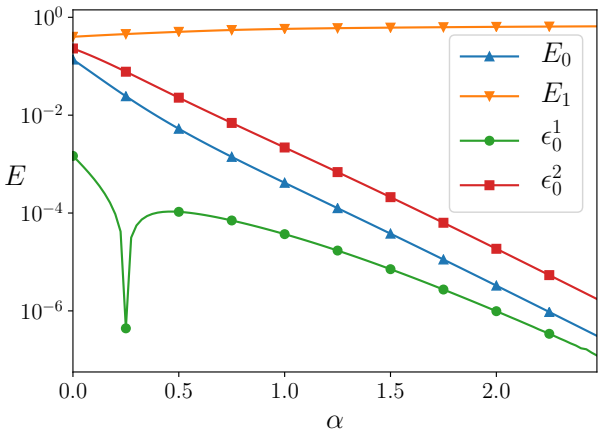

Figure 3.7: The lowest two positive energy single-particle levels for the physical spectrum E_0 (blue, tri-up) E_1 (orange,tri-down) with $L = 152$ sites and the entanglement spectrum with a single cut ϵ_0^1 (green,dots) and two cuts ϵ_0^2 (red,squares) with $L = 300$ and $L_A = 152$, all plots have $\Delta = 0.7$, $\mu = 0.2$, and OBC. The energy is split from zero due to a non-local coupling between edges, even in the case of a single-partition.

(b) and long-range (d) chain. For the short range chain, the midgap energies are within $\sim e^{-L_A/\xi}$ of zero energy as exponentially localised edge modes form at the virtual boundaries. In this case the entanglement Hamiltonian is of a similar form to the physical short-range Hamiltonian. For the infinite range chain, the midgap energies are is split significantly from zero energy, much like the unpartitioned chain. We saw that the physical spectrum is split from zero due to a physical coupling between the edges. This could be the case here, where the entanglement Hamiltonian may have a similar form to the physical Hamiltonian with a long-range coupling between all sites. Alternatively, and more likely as evidenced by Fig. 3.9, the overlap between the virtual boundaries is now significant enough to split the energies due to the polynomial decay into the bulk.

Comparing entanglement spectra with physical energies

Compare now the affect of α on the lowest positive single-particle entanglement level with the equivalent physical energy, see Fig. 3.7. So that the entanglement

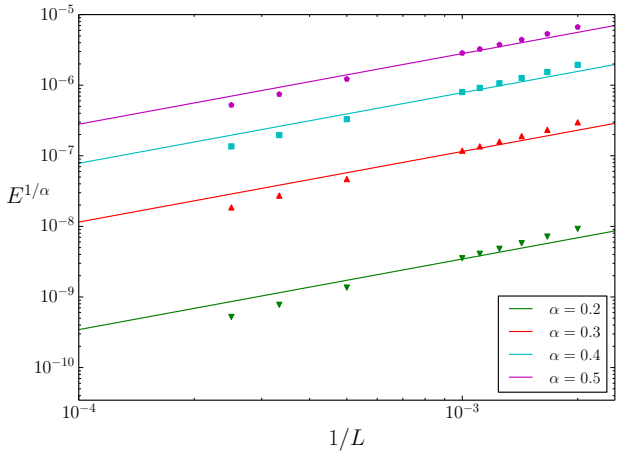

Figure 3.8: Scaling analysis of the groundstate energy, scaled by the inverse of the decay exponent α^{-1}, against inverse system size $1/L$ on a log-log plot. All data points have $\Delta = 0.7$ and $\mu = 0.2$. The lines are fit to the function $\tilde{E}_L^\alpha = \tilde{E}_g^\alpha \cdot \frac{1}{L}$, where $\tilde{E}_g^\alpha$ is a variational parameter for the gradient and y-intercept is fixed to zero. In all cases for $\alpha > 0$ we see the energy decay to zero with increasing system size.

Hamiltonian and the physical Hamiltonian can be compared directly, the system size L for the physical spectrum is chosen to be same as the subsystem size L_A of the partitioned states. For the physical energy, there is a clear exponential decay for all choices of α. At $\alpha = 0$ the result agrees with the analytical result found in Eq. (3.3.4). As α is tuned away from the infinite point and approaches the short range limit $\alpha \to \infty$, the energy reduces to a zero value (up to $e^{-L/\xi}$ due to finite size). The first excited state E_1 remains gapped away from E_0 for all α so it is in the same topological phase as the local model, protected by the non-trivial value of $\mathcal{M}$, and can be characterised by the same $\mathbb{Z}_2$ topological invariant.

As the decay in energy is a consequence of the decaying coupling between the two ends of the chain, for all $\alpha > 0$ we should find that the energy in the $L \to \infty$ limit is zero. This can be evidenced in Fig. 3.8 where a scaling analysis of the physical edge mode energy has been carried out for different values of α. We use a linear scaling ansätze $\tilde{E}_L^\alpha = \tilde{E}_g^\alpha \cdot \frac{1}{L}$, with $\tilde{E}_g^\alpha$ a variational parameter for the gradient. The y-intercept is fixed to zero. The energy is linearised by the

exponent $E^{1/\alpha}$ and plotted against inverse system size on a log-log plot. For all values of α we find that the energy decays to zero energy with increasing system size, hence the non-zero energy can be attributed to a finite size effect and the infinite range model is a 'special point' that remains at non-zero energy for all L. Note that if a log-log plot results in a straight line then the input data must be of the form $y = ax^b$ where $\log(a)$ is the y-intercept and b is the slope. That the data points in Fig. 3.8 are straight lines justifies the linearisation $E \to E^{1/\alpha}$ followed by the use of a linear ansätze. The result is that energy scale to zero as $E \sim (1/L)^\alpha$. In order to improve the fitted lines in Fig. 3.8 it is required to let α also be a variational parameter and not be fixed exactly to the coupling decay exponent.

The partitioned ground state energies in Fig. 3.7, ϵ_0^1 and ϵ_0^2, display a slightly different behaviour to the physical energy E_0, indicating that the form of the entanglement Hamiltonian is not identical to the physical Hamiltonian. For $\alpha \gtrsim 0.5$, E_0 and ϵ_0^2 have the same slope; however, E_0 is initially subject to a faster decay. For these values of α the decay in ϵ_0^2 is dominated by the overlap of the two edges, whereas the decay in E_0 is less affected by exponentially localised edge modes and has a decay dominated by the non-local coupling. The single partition has energy ϵ_0^1 that is an order of magnitude less than all other energies. If this had the properties of a long-range chain with a single boundary we would see that it has zero energy, pinned in the same way as the local Majorana chain. Instead we see two behaviours: there is an initial fast decay, followed by a slower decay. The fast decay can be attributed to a sharp reduction in overlap between the physical and virtual edge, that is steeper than ϵ_0^2, as the physical edge is exponentially localised. The slope that follows decays similarly to E_0 and ϵ_2, that must be a feature of non-local couplings.

It would be interesting in future work to complete a scaling analysis of the ground state entanglement energies ϵ_0^1 and ϵ_0^2, to support the discussion given above. As a conjecture, one would expect that ϵ_0^2 remains fixed when $\alpha = 0$ for any system size and decays as α increases, similarly to the behaviour of E_0. On the other hand, ϵ_0^1 should, in the $L \to \infty$ limit, be zero for all choices of α. This is akin to the physical energy of the ground state of the infinite range Hamiltonian with a single boundary, that is pinned to zero energy.

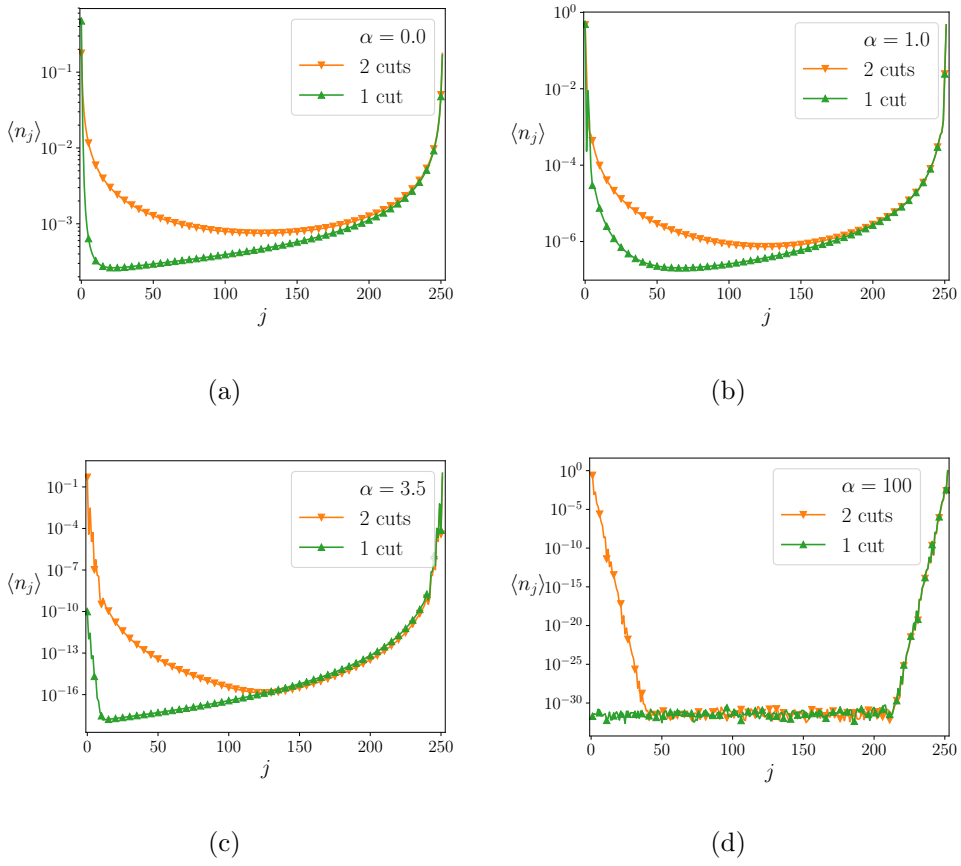

Figure 3.9: Local density $\langle n_j \rangle$ for the ground state of the entanglement Hamiltonian measured in subsystem A both for a single partition (green up triangles) and for two partitions (orange down triangles). The system is in a topological phase with $L = 500$, $\Delta = 0.7$ and $\mu = 0.2$; in both cases the region A has 252 sites. Figs. a-d have decay exponent $\alpha = 0, 1, 3.5, 100$ respectively. When α is small there are both virtual and physical boundaries that are a result of Majoranas pairing across all sites. (d) is an example of exponential localisation, where the nearly perfect straight lines (down to the computer noise level) are a result of local couplings simulated with very large α.

Entanglement eigenvectors for the groundstate

Following an analysis of the entanglement spectrum, it is also insightful to look at the ground state $|\Psi^E\rangle$ of H_E^f to see where entanglement is localising in the

region A. In Fig. 3.9 we plot the local density $\langle n_j \rangle$ of the ground state $|\Psi^E\rangle$ of H_E^f with both a single partition and two partitions for different values of α. (a) shows the infinite limit $\alpha = 0$. For two cuts leaving two virtual boundaries, the mode is localised to both edges with a power-law dependence. Contrast this with the behaviour of the physical edge localising at $j = 1$ of the green curve. Due to the effect of non-local couplings the physical edge mode is correlated with the remainder of the chain, in particular it is with the edge mode formed at the partition.

Moving to (d) shows the expected behaviour for a local chain. For a single cut, the entanglement decays exponentially away from the partition to the level of computer noise. With two cuts, the entanglement between regions A and B localises at two places, but as with the single cut it decays exponentially in both cases. This figure should be used as a example of the known behaviour expected in local one-dimensional gapped ground states. (b) and (c) show two intermediate α values between (a) and (d). Comparing with (d), in (b) and (c) the initial decay from both the partition and the physical edge is exponential. However, non-local couplings and finite size restrict this decay, forcing an algebraic profile that allows entanglement to spread out across the chain. Notice that as α increases, the smallest value on the y-axis reduces by orders of magnitude for both a single cut and two cuts. This is a signature of the edge Majoranas becoming more localised as it becomes less energetically favourable to couple with Majoranas at other sites.

3.5 Summary

In this Chapter we aimed initially to focus on an infinite-range non-interacting free-fermion chain to probe its topological properties. By fixing the chain to have OBC in 1-dimension, we showed that a generating function method could be used in order to arrive at closed form solutions for the groundstate of the Schrödinger equation. In doing so, we also extracted the conditions for existence of a topological phase and the specific localisation properties of the groundstate. Through the approach of first studying a semi-infinite chain and then a finite chain, it was found that non-zero energies arise specifically though the presence

of a second boundary that is physically coupled to the first boundary. Without the second, the parity dictates that there is a an edge mode localised at the boundary; however, PHS pins it to zero energy. Finding a zero energy Majorana mode at the end of a semi-infinite chain is sufficient evidence that the non-local chain is in a topological phase. This was confirmed numerically using the Pfaffian invariant that is a well-defined invariant for a $\mathbb{Z}_2$ topological phase.

We next questioned what signatures the extended range couplings would have on the single-particle entanglement spectrum. For the local chain, it is is expected that when a partition is made there forms a virtual edge mode at the boundary of the partition. As correlations decay exponentially [79], when there are two partitions the edges have an exponentially decaying overlap giving very close to zero energy midgap states. When a single cut is made, there forms a single virtual boundary that is far enough from the exponentially decaying physical boundary to have no effect. The spectrum results in a single zero energy midgap state. Compared with the non-local chain, we see that for a single cut or two cuts there are two modes split from zero energy in the gap of the bulk.

Exposing the localisation properties of the midgap states of the entanglement Hamiltonian for a single partition shows that the virtual edge modes have a slower decay than the physical edge modes. Regardless of the asymmetry of the boundary modes, there are fluctuations between the two edges that result in the forming of hybridised boundary modes with non-zero energy. This is certainly a feature of the non-local coupling, compared with the local chain with a single cut that has a single zero energy mode and with an exponentially localised virtual energy mode.

In future work it would be interesting to see if the generating function method easily generalises to the to other parameter regimes, e.g. long range hopping with short rang pairing, decaying couplings or 2-dimensional lattices. This would be a good exercise in testing the robustness of the method and its success brings its applicability to physically realistic models. It would also be good to complete a more thorough analysis of correlations through correlation functions of the ground state. It would be the aim to find accurate length scales that the non-local chain can be compared against quantitatively.

Chapter 4

Efficiency of the Kohn-Sham model in describing interacting fermions

4.1 Introduction

Finding the ground state of a quantum many-body system is a notoriously difficult problem. These interacting systems have a Hilbert space that grows exponentially with the number of particles being modelled, posing problems for direct diagonalisation of the Hamiltonian on a computer. They are also often intractable when attempting an analytical treatment due to the non-integrability of the model. There are a variety of approximate analytic and numerical methods that may be employed, including: mean-field theory, perturbation theory, density functional theory (DFT), and many others. However, when one uses an approximate method it is often the case that some information may be lost and the resulting state does not fully capture all properties of the interacting system.

In this Chapter, we study the applicability of the Kohn-Sham (KS) model, where through DFT local densities are the basic variable, when approximating the ground state of an interacting Hamiltonian. The KS model is a non-interacting auxiliary system that, in principle, has the ability to predict all observable quantities of an interacting system. This is possible through the Hohenberg-Kohn

theorems that show first that there is a unique mapping from an external potential to a quantum state. Then, by variationally minimising the energy with respect to the local electron density, the lowest energy gives the correct distribution of densities [80]. It is most effective when interactions are small and the physics of the system does not change much from the non-interacting point. This is because interactions may change the effective degrees of freedom of the system, that are not well described by a single Slater determinant of orbitals in the free manifold of the non-interacting model. An example of this is the ability of KS to describe fractional charges or predicting phase transitions, such as the Mott transition [81]. Further, known functionals used in the strongly correlated regime are currently unsuccessful as a general tool to be used for any system. This is certainly an open question in DFT.

We focus on the ability of the KS model to reproduce biparitite entanglement of the interacting model [2]. To do so, we use the interaction distance $D_{\mathcal{F}}$ – a tool that measures how far a given entanglement spectrum is from the set of all free fermionic entanglement spectra, the closest state is the optimal free state. Since it was first introduced in [19], there have been a variety of works that have followed highlighting the usefulness of $D_{\mathcal{F}}$ in diagnosing properties of many-body quantum systems [2, 3, 82, 83, 84, 85]. By applying this tool to DFT, we can determine how optimal the KS model is over the space of all free states. This gives a quantitative answer to how well the KS model reproduces entanglement, whilst as a byproduct allows an optimal entanglement model to be defined. This optimal entanglement model, with the optimal free state as its groundstate, is a standard for which free auxiliary models may be compared against. The proposal of an optimal entanglement model is important in the context of DFT/KS theory as it sets a lower bound for how accurate the entanglement features of the corresponding groundstate can be. It also highlights, in regions where $D_{\mathcal{F}} \approx 0$, where a better free approximation could be made than the KS model.

We first introduce DFT and KS theory as an approximation for many-body systems, before introducing $D_{\mathcal{F}}$ as a tool to probe them. We find that the interaction distance bounds the applicability of the optimal entanglement model in all of parameter space, whilst it only bounds the KS model in the perturbative regime. The analysis is concluded with a study of the Hubbard dimer, a toy model for

strongly correlated systems, highlighting that even for this simple system DFT can produce unbounded errors on entanglement in the strongly correlated regime.

4.2 Density functional theory

The idea of DFT is simple: if the ground state electron density distribution $n(\mathbf{r})$ is known, then all other observable quantities may be deduced [80]. Therefore, we may reduce the interacting many-body system to a problem of non-interacting electrons, and providing they reproduce the correct $n(\mathbf{r})$, we recover all observables of the interacting system, albeit approximately. One advantage of using non-interacting fermions is that we may use a Slater determinant to produce the required anti-symmetric ground state wavefunction from single-particle states, thus making the calculation tractable. The non-interacting system is called the KS system and, through DFT, there exists a unique mapping between a ground state and its non-interacting KS counterpart [86]. Remarkably, the KS ground state has been used beyond finding local densities, for e.g. to find average quantum work [87] or even entanglement calculations [88], in some cases. Let us now look at little closer at DFT and KS theory.

In DFT the density distribution $n(\mathbf{r})$ is the basic variable of the system, where $\mathbf{r}$ is a lattice vector. Consider an N-particle many-body wavefunction $|\Psi\rangle = \Psi(\mathbf{r}_1, \mathbf{r}_2, \ldots, \mathbf{r}_N)$ that we wish to approximate, spin degrees of freedom have been dropped for now. Its density distribution $n(\mathbf{r})$ at $\mathbf{r}$ is found by tracing out all other degrees of freedom

$$n(\mathbf{r}) = N \int \prod_{j=2}^{N} d\mathbf{r}_j \Psi^*(\mathbf{r}, \mathbf{r}_2, \ldots, \mathbf{r}_N)\Psi(\mathbf{r}, \mathbf{r}_2, \ldots, \mathbf{r}_N), \tag{4.1}$$

where the factor N ensures that normalisation of the wavefunction gives the correct number of particles in the system. As a first approximation we could identify $|\Psi\rangle$ as a product of single-particle wavefunctions $\psi_j(\mathbf{r}_j)$ at some general point $\mathbf{r}_j$, this is the Hartree approximation. However, this does not take into account the anti-symmetric nature of a fermionic wavefunction. Therefore, we

use a Slater determinant [89]

$$\Psi(\mathbf{r}_1, \mathbf{r}_2, \ldots, \mathbf{r}_N) = \frac{1}{\sqrt{N!}} \begin{vmatrix} \psi_1(\mathbf{r}_1) & \psi_2(\mathbf{r}_1) & \ldots & \psi_N(\mathbf{r}_1) \\ \psi_1(\mathbf{r}_2) & \psi_2(\mathbf{r}_2) & \ldots & \psi_N(\mathbf{r}_2) \\ \vdots & \vdots & \ddots & \vdots \\ \psi_1(\mathbf{r}_N) & \psi_2(\mathbf{r}_N) & \ldots & \psi_N(\mathbf{r}_N) \end{vmatrix}. \tag{4.2}$$

If the many-body wavefunction is an eigenstate of a non-interacting Hamiltonian then this single Slater determinant would give everything we need. One could variationally optimise over the single particle states until the true ground state is found, known as the Hartree-Fock approximation [90, 91]. However, in general this is not the case as interactions cause mixing between single particle states – they cannot be treated as independent orbitals. Note that in this introductory section the discussion is consistent with the DFT literature with a specific set of problems in mind: atomic systems consisting of electrons and nuclei. However, the basic principles can be extended to more abstract models, like spin systems or particles with different exchange statistics.

4.2.1 The Hohenberg-Kohn theorems

At the core of DFT are the Hohenberg-Kohn theorems [80]. The two theorems state that:

(1) The external potential is a unique functional of the electron density in the ground state, and therefore the total energy is also a functional of the ground state electron density, up to an additive constant.

(2) The groundstate energy may be obtained variationally, i.e. the total energy of a system is minimised for the correct ground state density.

Take an explicitly interacting Hamiltonian H that satisfies the Schrödinger equation $\langle\Psi| H |\Psi\rangle = E_{\text{gs}}$, where E_{gs} is the ground state energy. A general H is built from a kinetic operator, $\hat{K}$, an interaction operator, $\hat{W}$, and a local external potential, $\nu_{\text{ext}} = \sum_j \nu(\mathbf{r}_j)$. The first theorem tells us that if ν_{ext} is a functional of electron density $n(\mathbf{r})$ and so is the ground state energy, then the sum of $\hat{K}$ and $\hat{W}$ must also be a functional of $n(\mathbf{r})$. To show this, assume that there are two Hamiltonians H^a and H^b that only differ in potentials by no more than an

additive constant ν^a_{ext} and ν^b_{ext}, corresponding to ground states $|\Psi^a\rangle$ and $|\Psi^b\rangle$ respectively. Now suppose that they have the same ground state density $n(\mathbf{r})$. The variational principle returns the inequality

$$E^a < \langle\psi^b|\, H^a\, |\psi^b\rangle = \langle\psi^b|\, H^b\, |\psi^b\rangle + \langle\psi^b|\, (H^a - H^b)\, |\psi^b\rangle \tag{4.3}$$

$$= E^b + \langle\psi^b|\, (\nu^a_{\text{ext}} - \nu^b_{\text{ext}})\, |\psi^b\rangle \tag{4.4}$$

$$= E^b + \int d\mathbf{r}\, n(\mathbf{r})(\nu(\mathbf{r})^a - \nu(\mathbf{r})^b). \tag{4.5}$$

In the final line we have used that the total potential energy is the sum of all point potential energy contributions in space $\langle\psi|\, \nu^{\text{ext}}\, |\psi\rangle = \int d\mathbf{r}\, n(\mathbf{r})(\nu(\mathbf{r})$. Now, interchange a and b and sum the result. The result $E^a + E^b < E^b + E^a$ is a contradiction. Therefore the first theorem holds. The physical idea behind this is that two systems each with a fixed N electrons will interact and move around in the same way, unless there is disorder or defects introduced into one of the systems. These disorders are represented by the external potential that determines the resulting wavefunction. That all systems with the same number of electrons and external potential behave the same is called N- and ν-representability.

Taking into account $\nu-$representability, the energy expectation value of the total Hamiltonian can be expressed as

$$\langle\Psi|\, H\, |\Psi\rangle = \langle\Psi|\, \hat{K} + \hat{W}\, |\Psi\rangle + \sum_j^N \langle\Psi|\, \nu(\mathbf{r}_j)\, |\Psi\rangle \tag{4.6}$$

$$= F[n(\mathbf{r})] + \int d\mathbf{r}\, n(\mathbf{r})\nu(\mathbf{r}), \tag{4.7}$$

where $\hat{F} = \hat{K} + \hat{W}$ is an operator with functional form F that is the combined interaction and kinetic energy functionals. To show the second theorem we need to apply the variational principle to a $\nu-$representable system that obeys the first theorem. Given an electron density distribution $n(\mathbf{r})$ there is a corresponding unique groundstate $|\Psi\rangle$ with energy E_0 and external potential ν^{ext}. If this state is used as a trial state for the potential $\tilde{\nu}$ then

$$\langle\Psi|\, H\, |\Psi\rangle = \langle\Psi|\, \hat{K}\, |\Psi\rangle + \int d\mathbf{r}\, n(\mathbf{r})\tilde{\nu}(\mathbf{r}) \tag{4.8}$$

$$= E_{\tilde{\nu}} > E_0, \tag{4.9}$$

where the final inequality comes from the uniqueness of the groundstate and the variational principle. This implies that the ground state is non-degenerate; however, it has been shown that DFT may be applied to degenerate ground states [92] and also excited states [93]. The Hohenberg-Kohn theorems show that solutions to the Schrödinger equation can be found by variationally minimising the functional $E[n(\mathbf{r})]$ with respect to ν-representable densities. Thus, the complexity of the many-body problem is reduced from one that grows exponentially with system size to one that grows linearly with system size.

4.2.2 The Kohn-Sham equations

Following the work by Hohenberg and Kohn [80], Kohn continued work on this subject along with Le Jeu Sham in order to develop a systematic method for approximating the functional $F[n(\mathbf{r})]$, defined in Eqs. (4.6) and (4.7). To do so, they map the interacting Hamiltonian onto a fictitious Hamiltonian of non-interacting electrons [86]. One result of Kohn and Sham is that the energy functional in Eq. (4.7) may be rewritten as

$$E[n] = K[n] + \int d\mathbf{r}\ \nu(\mathbf{r})n(\mathbf{r}) + \frac{1}{2}\iint d\mathbf{r}d\mathbf{r}'\ \frac{n(\mathbf{r})n(\mathbf{r}')}{|\mathbf{r}-\mathbf{r}'|} + E_{xc}[n]. \tag{4.10}$$

where the final term, the exchange-correlation energy $E_{xc}[n]$, has an unknown form and contains all contributions to energy that are not accounted for in the single-particle terms and Coulomb repulsion (or the Hartree energy). In order to make the step from Eq. (4.7) to (4.10) the electron interaction operator $\hat{W}$ is separated into a known density-density term and everything else $E_{xc}[n]$.

A commonly used approximation for $E_{xc}[n]$ when looking at electron systems is the local density approximation [86]. It has the form

$$E_{xc}^{\mathrm{LDA}}[n] = \int d\mathbf{r}\, n(\mathbf{r})\epsilon_{xc}^{\mathrm{heg}}[n], \tag{4.11}$$

where $\epsilon_{xc}^{\mathrm{heg}}$ is the exchange-correlation energy density of an interacting homogeneous electron gas. It is a good approximation when the density is almost constant or when kinetic energy is dominant, i.e. weakly interacting [94]. Of course, $\epsilon_{xc}^{\mathrm{heg}}[n]$ must also be known or approximated. There are numerous ways

to do so, one method is to calculate exchange and correlation parts separately $\epsilon_{xc} = \epsilon_x + \epsilon_c$. The exchange part can be found exactly using a Hartree-Fock method and has an exact form $\epsilon_x = -Cn^{1/3}$, where C is a constant fixed by the system [95]. The exact functional form of ϵ_c is unknown, but can be found using quantum Monte Carlo simulations with essentially exact results [96]. The local density approximation in Eq. (4.11) is successful in its own right and it also forms the basis for other more sophisticated approximations.

From this form it is possible to construct an auxiliary Hamiltonian, H_{KS}, that upon acting on single-particle orbitals $\psi_j(\mathbf{r})$ gives contributions to the energy ϵ_j that, in principle, sum to the total energy of the system. The Kohn-Sham Hamiltonian is given by

$$H_{\mathrm{KS}} = \hat{K} + \hat{V}_{\mathrm{KS}} \tag{4.12}$$

where $\hat{V}_{\mathrm{KS}} = \nu_{\mathrm{ext}} + \nu_{\mathrm{H}} + \nu_{xc}$, ν_{H} is the Hartree potential, and ν_{xc} is the exchange correlation potential. To find solutions of the groundstate, one must variationally solve the Schrödinger equation

$$H_{\mathrm{KS}}\psi_j(\mathbf{r}) = \epsilon_j\psi_j(\mathbf{r}), \tag{4.13}$$

until the correct density distribution $n(\mathbf{r}) = \sum_j |\psi_j(\mathbf{r})|^2$ is achieved. Here we assume that the form of the exchange-correlation potential is unknown. There are various approximations that can be made, with varying levels of success, but here we choose to use an *exact* method.

4.2.3 Finding Kohn-Sham eigenstates by an exact DFT method

In order to test the applicability of DFT and KS theory we choose to use an exact method [87]. This is a numerical method and is effective only for very small system sizes where it is possible to obtain eigenstates by exact diagonalisation. The method works as follows:

1) Obtain the true groundstate (or an excited state) of an interacting Hamiltonian by exact diagonalisation.

2) Build a free auxiliary Hamiltonian using the same kinetic operator and external potential as the interacting Hamiltonian with a local potential operator that may be varied at each site.

3) Vary the local potentials of the auxiliary Hamiltonian until, by direct comparison with the local electron densities of the interacting model, the Hamiltonian adopts the correct H_{KS} groundstate wavefunction.

The method is powerful because it allows for the true KS wavefunction to be found for any choice of parameter value, up to some predetermined accuracy. Of course, its success depends on the correct wavefunction being computable in a finite amount of time. Hence, it is most successful for small system sizes. In [2] the exact method reproduces electron densities within an accuracy of 10^{-6} of the exact result. This was only achievable, consistently, in a system of two sites with spin-$\frac{1}{2}$ fermions, i.e. a 4-dimensional local Hilbert space. For larger system sizes (of even length) the computation time using the method outlined above became unreasonable to find reliable results. This could be improved by using a faster method to search the parameter space of the local potentials.

4.2.4 Limitations of DFT

The limitations of DFT follow mostly from choosing the correct functionals to minimise the energy $E[n]$ [81]. In particular, the functional form of the exchange-correlation energy is unknown. This term contains interaction effects that are not included in the other KS terms: the kinetic energy of non-interacting orbitals, the Hartree energy, and local potentials. There are many known functionals with varying levels of success: the simplest is a local density approximation, that is known to overbind molecules; the generalised gradient approximation, that has problems when gradients vary too quickly; and hybrid functionals, that combine different functionals but lack simplicity [94]. For systems that are not amenable to an exact KS treatment, choosing the appropriate functional can drastically affect the success of the result.

Another limitation of DFT is in its ability to accurately detect phase transitions or other effects inherent to strongly correlated systems. In [97] it was shown that DFT is successful, in principle, in probing first and second order

phase transitions. However, a Mott transition has the signature of moving from a conducting to an insulating phase through the opening of a Mott gap. This gap is not detectable by KS methods, but is important in the study of condensed matter systems. Further, DFT fails to provide a good approximation to a groundstate when the underlying quasiparticles are non-longer built from the same orbitals that describe the non-interacting limit. An example would be a groundstate built from fractionalised charges or fractionalised spins.

It is desirable to find a general method that can help improve on these limitations. To do so, the method would require knowledge (or optimisation of) the underlying quantum correlations that give the resultant quasiparticle structure. However, in DFT it is always possible to minimise the energy functional, i.e. to find the correct groundstate, with the correct local densities. It is not always possible to match the many-body entanglement with a free system. The closest free system, in terms of its biparitite entanglement, is found through the interaction distance that is discussed next.

4.3 Interaction distance

In this Section we introduce the interaction distance that is a diagnostic tool used to measure how far an entanglement spectrum is from the set of all free entanglement spectra [19]. Often in the study of many interacting particles it is first the aim to simplify the complexity of the problem by modelling the fully interacting system as free, as is demonstrated in the previous subsection via DFT. However, free (or close to free) approximations, such as DFT, mean field theory, or perturbation theory, are successful only when correlations are weak and can often fail to capture the full effect of correlations in a quantum system. Often, interesting physics arises from strong correlations. The interaction distance is the minimum distance between a given state and the manifold of all free states, through its biparitite entanglement. By defining an interaction distance we may directly probe an interacting model to find how close it is to free in all of parameter space and how optimal a given auxiliary free system is in the space of all free models. In practice the interaction distance is a variational method, but in contrast to usual variational methods it is basis independent. Through it, we

find that away from the non-interacting point of a model the groundstate may still have a free description, but in some other basis of free-fermions.

Next, we define the interaction distance and discuss how one would attempt to calculate it through a minimisation over single-particle entanglement levels. Then, we show that for a four-level entanglement spectrum there exists closed form solutions for the interaction distance and the minimising state.

4.3.1 Definition and calculation of the interaction distance

We aim to determine how close a given state $|\Psi\rangle$ is from the set of all free states, in terms of it bipartite entanglement. The entanglement spectrum, see section 2.3.2, can be used to quantify the entanglement between subsystems A and B of the full system $A \cup B$. It defined through the reduced density matrix found by tracing out one part of the full system $\rho = \mathrm{Tr}_B |\Psi\rangle\langle\Psi|$.

The interaction distance is defined as the minimum trace distance between a given reduced density matrix ρ and the set of all free reduced density matrices, $\sigma \in \mathcal{F}$ [19]

$$D_{\mathcal{F}} = \min_{\sigma \in \mathcal{F}} D_{\mathrm{tr}}(\rho, \sigma), \tag{4.14}$$

where $D_{\mathrm{tr}}(\rho, \sigma) = \frac{1}{2}\mathrm{Tr}\,|\rho - \sigma|$ is the trace distance metric for ρ and σ. The free density matrix σ is the exponential of a free-fermion Hamiltonian, i.e. Eq. (2.31), and therefore lies in $\mathcal{F}$. Instead of using the trace distance as a measure we are free to define the interaction distance in terms of some other entanglement indistinguishability tool, for e.g. relative entropy [98] or $\frac{1}{4}\mathrm{Tr}(\rho - \sigma)^2$. The reason for choosing the trace distance lies in its restatement in terms of projectors: it is $D_{\mathrm{tr}}(\rho, \sigma) = \frac{1}{2}\max_P \mathrm{Tr}P(\rho - \sigma)$, where the maximum is over all projectors P [98]. This is a useful interpretation of the trace distance. If ρ and σ are in a different basis then we can allow P to project one onto the basis of the other before measuring. It is also a metric distance, lending many other nice symmetries and properties (for e.g. satisfying the triangle inequality or being bound from above) that will be useful later in this chapter.

In its operator form in Eq. (4.14), the minimisation procedure will be a rather difficult task. Instead, the minimum trace distance can be found from the spectra

of ρ and σ, even if they do not share a common eigenbasis [85]. By diagonalising both ρ and σ, resulting in diagonal matrices ρ_D and σ_D respectively, finding the minima is reduced to finding a unitary transformation U that minimises the distance $D_{\text{tr}}(\rho_D, U^\dagger \sigma_D U)$. It was proven in [99] that the minimum occurs when the spectra are both sorted in the same order. Thus, U takes the form of a permutation matrix that sorts the spectra σ_D into the same order as ρ_D, or the identity $U = \mathbb{1}$ for ordered spectra.

In Eq. (2.41) we showed explicitly the structure of the many-body entanglement spectrum for free fermions. We may therefore recast σ in terms of the variational parameters, $\{\epsilon_k\}$,

$$\sigma = \exp\left[-E_0^f - \sum_k n_k(j)\epsilon_k\right], \tag{4.15}$$

where now the upper limit of the summation has been deliberately omitted. The $n_k(j)$ are free to represent any fermionic density operators and are no longer necessarily the same as those that built the original Hamiltonian. Thus, the interaction distance minimises over every possible free-fermion representation with only linearly many parameters. It is a significantly more efficient minimisation procedure than minimising over the full σ that grows exponentially with system size. We may therefore represent the minimisation in terms of the free modes $\{\epsilon_k\}$ as follows:

$$D_{\mathcal{F}}(\rho) = \frac{1}{2} \min_{\{\epsilon_k\}} \sum_j \left| e^{-E_j^E} - e^{-E_j^f\{\epsilon_k\})} \right|, \tag{4.16}$$

where $E_j^f(\{\epsilon_k\})$ are the eigenvalues of $-\log\sigma$ that are ordered in the same way as the eigenvalues E_j^E of $-\log\rho$.

4.3.2 Exact optimal free state for a four-level system

In this work we aim to use an exact KS scheme that removes errors due to approximating an accurate exchange-correlation functional. To complement this approach, we also use exact interaction distance calculations that remove errors due to numerical accuracy of the variational code [82, 2].

Reparametrisation of entanglement levels

By an exhaustive analysis of the interaction distance, we may obtain a full analytical solution for the optimal free state entanglement spectrum, and for $D_{\mathcal{F}}$ itself, for a four level system, ρ. The corresponding free spectrum, with a fixed number of four many-body levels, has two single-particle levels, ϵ_1 and ϵ_2, that build the full spectrum, as dictated by Eq. (2.41). It is convenient to work with eigenvalues of the reduced density matrix, σ, allowing the single-particle energies to be reparametrised by probabilities: b_1 and b_2, such that $0 \leq b_1 \leq b_2 \leq \frac{1}{2}$. Then, the free many-body spectrum is built in the following way:

$$\begin{aligned} \sigma_1 &= \left(\frac{1}{2}+b_1\right)\left(\frac{1}{2}+b_2\right), & \sigma_2 &= \left(\frac{1}{2}-b_1\right)\left(\frac{1}{2}+b_2\right), \\ \sigma_3 &= \left(\frac{1}{2}+b_1\right)\left(\frac{1}{2}-b_2\right), & \sigma_4 &= \left(\frac{1}{2}-b_1\right)\left(\frac{1}{2}-b_2\right), \end{aligned} \tag{4.17}$$

where the range of b_1 and b_2 ensures normalisation $\sum_j \sigma_j = 1$ and fixes the ordering to $0 \leq \sigma_4 \leq \sigma_3 \leq \sigma_2 \leq \sigma_1 \leq 1$. This reparametrisation is intuitive as it is simply all possible combinations of fermionic populations, expressed as probability amplitudes. If we wished to study a 2^N-level system, with for e.g. $N = 3$ free fermions, to build the full spectrum we take the product of each of the levels in Eq. (4.17) with each of $(\frac{1}{2}+b_3)$ and $(\frac{1}{2}-b_3)$, that results in a normalised 8-level spectrum as required.

Finding minima of $D_{\mathcal{F}}$ by direct differentiation

We wish to minimise Eq. (4.14) with respect to the free parameters $\{b_j\}$. So, first attempt to do so by directly differentiating the trace distance $D_{\text{tr}} = \frac{1}{2}\text{Tr}|\rho-\sigma|$, having substituted in Eq. (4.17), to find the stationary points as a function of the free parameters. In doing so, we find that the derivatives are not defined in the regions $\sigma_j = \rho_j$ for any j. We also find that second derivatives are always zero when $\sigma_j \neq \rho_j$, thus defining a saddle point and not a minimum. The minimum trace distance must therefore live on one of the boundary curves $\sigma_j = \rho_j$ or an intersection of two or more curves.

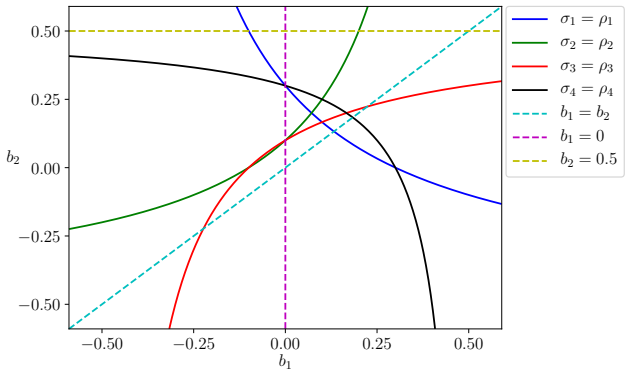

Figure 4.1: Free parameter values, b_1, b_2, that produce boundary curves $\sigma_j = \rho_j$ (solid lines) for $\{\rho_j\} = \{0.4, 0.3, 0.2, 0.1\}$. The triangle of dashed lines enclose the normalised and ordered regions for the free spectra. There are a variety of points of intersection within the normalised and ordered region for this choice of ρ. The intersection that matches the low level entanglement spectrum will give the smallest interaction distance. Thus, it is the b_1, b_2 pair at the intersection between $\sigma_1 = \rho_1$ and $\sigma_2 = \rho_2$ that give the interaction distance, $D_{\mathcal{F}} = \frac{2}{7}$.

Finding minima of $D_{\mathcal{F}}$ by matching low-lying levels

As it is the low-energy entanglement levels that dominate the behaviour of the system, if it is possible to match these levels then the optimal free state will more accurately represent the interacting system. In some cases, however, the intersection between the low level curves does not fall within the normalised and ordered region. In that case the most faithful representation lies on the curve $b_1 = b_2$.

An exhaustive analysis results in the following set of solutions for the interaction distance:

$$D_{\mathcal{F}} = \begin{cases} 2\sqrt{\rho_1} - 2\rho_1 - \rho_2 - \rho_3, & \text{if } \rho_1 \geq (\rho_1 + \rho_2)^2 \quad (4.18a) \\ \left| \dfrac{\rho_1\rho_4 - \rho_2\rho_3}{\rho_1 + \rho_2} \right|, & \text{otherwise.} \quad (4.18b) \end{cases}$$

and the corresponding set of free parameter solutions:

$$(b_1, b_2) = \begin{cases} \left(\sqrt{\rho_1} - \frac{1}{2}, \sqrt{\rho_1} - \frac{1}{2}\right), & \text{if } \rho_1 \geq (\rho_1 + \rho_2)^2 \quad (4.19a) \\ \left(\frac{\rho_1 - \rho_2}{2(\rho_1 + \rho_2)}, \rho_1 + \rho_2 - \frac{1}{2}\right), & \text{otherwise.} \quad (4.19b) \end{cases}$$

These exact solutions allow for an accurate study of the interaction distance without any error of numerical optimisation. The solutions (4.18a) and (4.18b) correspond to the cases where it is not possible and possible to match the lowest two levels of the entanglement spectrum, respectively.

In Fig. 4.1 we show an example of the boundary curves for the interacting spectrum $\{\rho_j\} = \{0.4, 0.3, 0.2, 0.1\}$, that produces $D_{\mathcal{F}} = \frac{2}{7}$. We are able to deduce this solution by first considering the condition: $\rho_1 \geq (\rho_1 + \rho_2)^2$. For our set $\{\rho_j\}$, this inequality is not satisfied so $b_1 \neq b_2$ and the minimum trace distance must therefore live at an intersection between the $\sigma_1 = \rho_1$ and $\sigma_2 = \rho_2$ curves. The pair b_1, b_2 at this intersection result in the free state σ that returns the interaction distance. It remains an open question to generalise this method to spectra with more than four levels.

4.4 Applicability of the Kohn-Sham model

We now aim to quantify the applicability of the Kohn-Sham model through an interaction distance analysis of an exact KS ground state, as introduced in section 4.2.3. By dealing with an exact KS model, both numerically and analytically, we remove the need to approximate the exchange-correlation functional that would likely result in errors creeping into the analysis. Of course, that we use an exact method limits our analysis to small system sizes when attempting a numerical treatment. When an analytical analysis permits we simply require that the ground state density distribution of the KS model is exactly the same as the interacting model – making the results applicable to any system size.

We begin by forming an upper-bound on observable quantities between two generic density matrices, before applying the bounding to local densities that are relevant to DFT and KS theory. Through this analysis we propose an 'optimal

entanglement model' that is a free auxiliary model with the optimal free state as its ground state. We find that, providing the interacting system is in the perturbative limit, the KS model is a good approximation to the optimal entanglement model. Thus, providing a constructive method for finding the optimal entanglement model within that regime – a task that remains an open question for the system in general.

4.4.1 Bounding observables with $D_{\mathcal{F}}$

The trace distance is a metric on the space of density matrices that is the maximum distance over all positive operator valued measures [98]. Therefore, we expect the state that minimises it over all free states to approximate well all observable quantities, as well as its bipartite entanglement. Of course, other methods may reproduce a single observable optimally, but the optimal free state best approximates *all* observables.

Consider the expectation value of an observable $\mathcal{O}$ for two density matrices ρ_1 and ρ_2 given by $\langle\mathcal{O}\rangle_{\rho_1} = \mathrm{Tr}\left[\mathcal{O}\rho_1\right]$ and $\langle\mathcal{O}\rangle_{\rho_2} = \mathrm{Tr}\left[\mathcal{O}\rho_2\right]$, respectively. To compare these expectation values we define their difference by the metric

$$d_{\mathcal{O}}(\rho_1, \rho_2) = \left|\langle\mathcal{O}\rangle_{\rho_1} - \langle\mathcal{O}\rangle_{\rho_2}\right|, \tag{4.20}$$

which, through the additivity property of the trace (as it is a linear map) $\mathrm{Tr}(A+B) = \mathrm{Tr}(A) + \mathrm{Tr}(B)$, reduces to

$$d_{\mathcal{O}} = \left|\mathrm{Tr}\left[\mathcal{O}(\rho_1 - \rho_2)\right]\right|. \tag{4.21}$$

We may express $\rho_1 - \rho_2$ in its diagonal basis, $\rho_1 - \rho_2 = \sum_k \psi_k \left|\psi_k\right\rangle\!\left\langle\psi_k\right|$, where ψ_k are the eigenvalues of $\rho_1 - \rho_2$. Then, via direct substitution into $d_{\mathcal{O}}$, we find that

$$d_{\mathcal{O}} = \left|\mathrm{Tr}\left[\mathcal{O}\sum_k \psi_k \left|\psi_k\right\rangle\!\left\langle\psi_k\right|\right]\right| \tag{4.22}$$

$$= \left|\sum_k \left\langle\psi_k\right| \mathcal{O} \left|\psi_k\right\rangle \psi_k\right| \tag{4.23}$$

$$\leq \left|\max_k \left\langle\psi_k\right| \mathcal{O} \left|\psi_k\right\rangle \sum_k \psi_k\right| = \left|\mathcal{O}_{\max}\right| \left|\sum_k \psi_k\right|, \tag{4.24}$$

where $\mathcal{O}_{\max}$ is the largest eigenvalue of the operator $\mathcal{O}$ in absolute value. It then follows from the Cauchy-Schwarz inequality [100] that

$$d_{\mathcal{O}} \leq |\mathcal{O}_{\max}| \sum_k |\psi_k| = |\mathcal{O}_{\max}| \operatorname{Tr} |\rho_1 - \rho_2| \,, \tag{4.25}$$

where the final equality contains the definition of the interaction distance when ρ_2 is the optimal free state of ρ_1. Therefore, upon setting $\rho_1 = \rho$ and $\rho_2 = \sigma$ the difference in expectation values are bounded by the interaction distance,

$$\left| \langle \mathcal{O} \rangle_\rho - \langle \mathcal{O} \rangle_\sigma \right| \leq C_{\mathcal{O}} D_{\mathcal{F}}, \tag{4.26}$$

with $C_{\mathcal{O}} = \frac{1}{2} |\mathcal{O}_{\max}|$ that depends only on the operator $\mathcal{O}$. As a result, the expectation value of any observable $\mathcal{O}$ with respect to the ground state ρ of the interacting system can be reproduced by the optimal free state σ with an accuracy that is controlled by $D_{\mathcal{F}}$. In contrast to Eq. (4.26), other methods aim to optimally determine a single observable at the expense of introducing unbounded error on the rest of the complementary observables. We will later see that this is the case for DFT when we find the interaction distance for a example system – the Hubbard dimer.

4.4.2 Bounding density with $D_{\mathcal{F}}$

We would like now to compare the applicability of the KS ground state and the optimal free state. As it is the local density of fermions that DFT optimises over, let us apply inequality (4.26) to the operator $\mathcal{O} = \hat{n}_j$. Following the notation introduced in the previous subsection, for a state with reduced density matrix ρ we define $\hat{n}_{j,\rho} = \operatorname{Tr}(\rho \hat{n}_j)$ as the local density at site j. The 'natural' metric [101], between ρ and σ, on the metric space of local densities over all sites is given by

$$D_n(\rho, \sigma) = \sum_j |\hat{n}_{j,\rho} - \hat{n}_{j,\sigma}| \,. \tag{4.27}$$

To arrive at this definition from Eq. (4.26), we must sum over all sites. Then, Eq. (4.26) becomes

$$\sum_j \left| \langle \hat{n}_j \rangle_\rho - \langle \hat{n}_j \rangle_\sigma \right| \leq \sum_j C_{\hat{n}_j} D_{\mathcal{F}}. \tag{4.28}$$

The left hand side of this equality is the definition of the natural metric and the right hand side consists of a constant $C = \sum_j C_{\hat{n}_j}$ multiplied by the interaction distance. The bound reduces to

$$D_n(\rho, \sigma) \leq C D_{\mathcal{F}}. \tag{4.29}$$

Due to the key property of the (exact) Kohn-Sham model, that $\langle \hat{n}_j \rangle_\rho = \langle \hat{n}_j \rangle_\kappa$, the bound in Eq. (4.29) may be cast in terms of the optimal, σ, and Kohn-Sham, κ, ground states

$$D_n(\kappa, \sigma) \leq C D_{\mathcal{F}}. \tag{4.30}$$

Hence, the interaction distance bounds the density distance between the KS and optimal free state. This bound implies that for $D_{\mathcal{F}} \approx 0$, e.g. in the perturbative regime, the optimal free state has local fermion densities that are very close to the densities of the KS ground state, and are exact when $D_{\mathcal{F}} = 0$. Of course, this does not give any information about how well κ reproduces other observables – it only gives the applicability of σ compared with exact DFT.

4.4.3 Trace distance bounding in perturbative limit

We now investigate when the ground state found by the exact KS method is a good approximation to the optimal free state by forming an upper bound on $D_{\text{tr}}(\kappa, \sigma)$ within the perurbative limit. Assume that the density matrices are a continuous functional of the fermion densities, e.g. when the system is in the perturbative regime with no phase transitions caused by the interactions. We can write $n_F = n + \delta n$, with n_F the ground state density of the optimal free state, n the ground state density of the interacting/KS model, and δn a small linear response.

First consider the limit $\delta n \to 0$. In this limit $D_{\text{tr}}(\kappa, \sigma) \to 0$ and $D_{\mathcal{F}} \to 0$, so that the inequality above is satisfied by the equality $0 = C \cdot 0$. Next, consider δn to be small, but non-zero. From Eq. (4.30), it can be seen that the density metric is bound by the interaction distance. We showed in section 4.2 that, when DFT Hohenberg-Kohn-type theorems apply, any property of a pure state interacting system described by a Hamiltonian $\hat{H} = \hat{K} + \hat{W} + \hat{V}$, can be written as a functional

of the system ground state density. So, in particular, the (non-diagonal) density matrix elements can also be written as a functional of the ground state density, and thus as a functional of n and δn.

For small δn, we can approximate $D_{\mathrm{tr}}(\sigma,\kappa)$ through a Taylor expansion around $\delta n = 0$. Up to $\mathcal{O}(\delta n^2)$, the trace distance becomes

$$D_{\mathrm{tr}}(\kappa,\sigma)[\delta n, n] \approx \left.\frac{\delta^2 D_{\mathrm{tr}}}{\delta n^2}\right|_{\delta n=0} (\delta n)^2 > 0, \tag{4.31}$$

which holds due to $\delta n = 0$ being a minimum (and the trace distance being a metric). Similarly, we can approximate the density metric about the minimum:

$$D_{\mathrm{n}}(\kappa,\sigma) = D_{\mathrm{n}}(\kappa,\sigma)[\delta n, n] \tag{4.32}$$

$$\approx \left.\frac{\delta^2 D_{\mathrm{n}}}{\delta n^2}\right|_{\delta n=0} (\delta n)^2 > 0 \tag{4.33}$$

Using Eqs. (4.31) and (4.33), and up to higher orders than $(\delta n)^2$ in δn, we can then write

$$D_{\mathrm{tr}}(\kappa,\sigma)[\delta n, n] \approx f(n)\cdot D_{\mathrm{n}}(\kappa,\sigma), \tag{4.34}$$

where $f(n) = \left.\frac{\delta^2 D_{\mathrm{tr}}}{\delta n^2}\right|_{\delta n=0} \left(\left.\frac{\delta^2 D_{\mathrm{n}}}{\delta n^2}\right|_{\delta n=0}\right)^{-1}$ is a functional of n, but for a given n it will be a number greater than zero. Using Eq. (4.30) we then obtain

$$D_{\mathrm{tr}}(\kappa,\sigma) \leq f(n)\cdot C D_{\mathcal{F}}. \tag{4.35}$$

Therefore, when the interaction distance is small σ and κ are close and have very similar entanglement properties.

This analysis is restricted to $f(n)$ being a well-behaved function, which is ensured from the beginning by fixing the density matrices to be a continuous functional of the density with small interactions. With this restriction, it is expected that both the numerator and denominator of $f(n)$ will be small, as the optimal model will not have varied much from the non-interacting point. Providing they numerator and denominator result in a finite value for $f(n)$, for e.g. they scale similarly, then in the perturbative regime for $D_{\mathcal{F}} \approx 0$ the KS model offers a way to constructively obtain the optimal entanglement model and, in turn, the optimal free state.

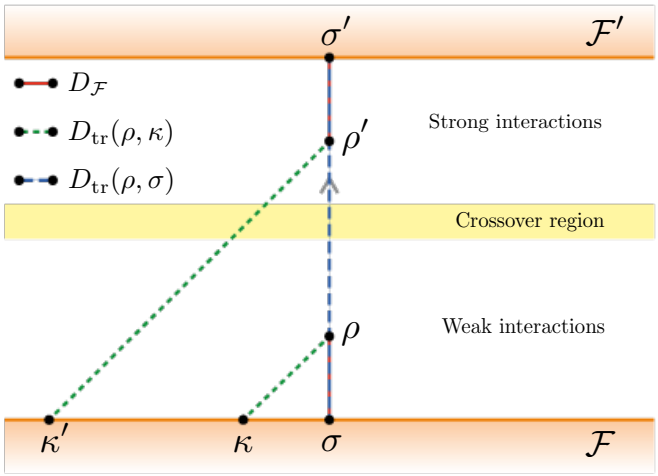

Figure 4.2: A sketch of the relative positions of interacting, ρ, optimal-free, σ, and Kohn-Sham, κ, reduced density matrices on a manifold parametrised by the entanglement spectrum. The spectra in the free regions, $\mathcal{F}$ and $\mathcal{F}'$, have a structure that is factorisable into free fermions, i.e. the same as Eq. (4.15). The regions differ by the number of non-zero single-particle probabilities contribute to σ. Interactions have the effect of changing the effective degrees of freedom from one free manifold $\mathcal{F}$ to another $\mathcal{F}'$. The KS model is always built from operators living in the manifold $\mathcal{F}$, giving unbound errors on its trace distance from the interacting state $D_{\mathrm{tr}}(\rho,\kappa)$.

4.4.4 Triangle Inequality

We now investigate the bipartite entanglement of the model. We employ the triangular inequality of the trace distance metric between the interacting, ρ, the optimal free, σ, and the KS, κ, reduced density matrices. In the perturbative regime the interaction distance provides an upper bound for $D_{\mathrm{tr}}(\kappa,\sigma)$; therefore, we have $D_{\mathrm{tr}}(\rho,\kappa) \leq (1+c)D_{\mathcal{F}}$, where the constant $c = f(n)\cdot C$ from Eq. (4.35). Moreover, due to σ being optimal we have that $D_{\mathcal{F}}$ provides a lower bound to $D_{\mathrm{tr}}(\rho,\kappa)$, thus giving

$$D_{\mathcal{F}} \leq D_{\mathrm{tr}}(\rho,\kappa) \leq (1+c)D_{\mathcal{F}}. \tag{4.36}$$

Hence, in the perturbative regime when $D_{\mathcal{F}} \approx 0$ the KS model reproduces all properties of the interacting system, while a non-zero $D_{\mathcal{F}}$ bounds the errors in

determining the entanglement properties of the interacting model. The KS model within this regime provides a faithful construction of the optimal entanglement model. Away from the perturbative regime it is possible that the upper bound in (4.36) fails, by having κ far from ρ even if $D_{\mathcal{F}} \approx 0$. This is due to strong interactions, that may not only change the effective local fermion potential, $\hat{V}_{\mathrm{KS}}$, but also the effective kinetic term, $\hat{K}$, that does not contain energy contributions from interactions. In this limit a single Slater determinant of orbitals in $\mathcal{F}$ no longer accurately captures the groundstate.

This change in degrees of freedom is sketched in Fig. 4.2 (taken from [2]), where the relative positions of the reduced density matrices are shown on a manifold parametrised by the entanglement spectrum, such that the distance between points is given by their trace distance. There are two shaded (orange) regions $\mathcal{F}$ and $\mathcal{F}'$ that represent free regions with reduced density matrices of the same form presented in Eq. (4.15) and spectra that can be factorised into single-particle levels. The regions differ in the number of non-zero single-particle probabilities used to build the spectrum. Thus, the regions are connected. To see this consider a spectrum with a set of single-particle levels that live in $\mathcal{F}$. If $\mathcal{F}$ and $\mathcal{F}'$ differ by only one single-particle level, then one could tune a single level continuously to zero to move it from $\mathcal{F}$ to $\mathcal{F}'$; however, this is not the effect that interactions have on the entanglement spectra studied here so the regions can be considered effectively disconnected. To move from one region to another it is therefore required for interactions cause a transition (or crossover) into a new behaviour, changing the number of required single-particle modes.

In Fig. 4.2, for weak interactions all three density matrices are close as the interacting model is close to the non-interacting point and their trace distance is small due to Eq. (4.36). The projection of equal fermion densities onto the manifold $\mathcal{F}$ is along the $D_{\mathrm{tr}}(\rho, \kappa)$ diagonal dotted lines for which there is no bound on the error away from the perturbative limit. Large interactions U can have the effect of changing the effective degrees of freedom of the interacting state ρ', whilst emitting a free description, i.e. $D_{\mathcal{F}} \approx 0$, making κ' a bad approximation to ρ'. Nevertheless, σ always provides the closest free description of ρ.

The parent Hamiltonian of the optimal free state can be used to define a suitable auxiliary free model that identifies the effective degrees of freedom of

the interacting model for all coupling regimes. When $D_{\mathcal{F}} \approx 0$ such an auxiliary model not only faithfully reproduces the entanglement properties of the interacting model but, due to Eq. (4.26), it can also estimate all of its observables, such as local fermion densities. This 'optimal entanglement' model generalises the KS model that can fail to reproduce the entanglement properties even if $D_{\mathcal{F}} \approx 0$. To build this auxiliary model one first needs to identify the effective fermionic degrees of freedom that correspond to the quantum correlations of the model. If $D_{\mathcal{F}} \approx 0$ for strong interactions then the number of fermionic degrees of freedom of the emerging free theory can be either the same or smaller than the initial theory without the interaction term: interactions may freeze some of the initial fermionic degrees of freedom and do not increase their number.

4.5 Interaction distance and KS analysis of the Hubbard dimer

We now apply the procedure of section 4.4 to a known model that is amenable to both the exact KS method (see section 4.2.3), and exact $D_{\mathcal{F}}$ calculations (see section 4.3.2). The Hubbard dimer is a 1-dimensional chain of spin-$\frac{1}{2}$ fermions restricted to $L = 2$ sites. It has already been studied using an exact KS method in [87] and at half-filling, $N_\uparrow = N_\downarrow = 1$, it has a four-level entanglement spectrum meaning that the result of section 4.3.2 may be applied. The interacting model (in 1-dimension) is integrable, so it exhibits exact solutions, and is an example of a strongly correlated system. It is therefore an excellent model to exemplify the applicability of KS theory and the optimal entanglement model. We begin by introducing the Hubbard model in general, before restricting to the dimer.

4.5.1 The Fermi-Hubbard model

The Fermi-Hubbard model is a simple model of hopping electrons, that includes a Coulomb repulsion for electrons of different spin occupying the same lattice site. It is an extension of the tight-binding model, that successfully describes a metallic phase of electrons on a lattice, where now the interaction U gives rise to, amongst other phenomena, an insulating phase [102].

4. EFFICIENCY OF THE KOHN-SHAM MODEL IN DESCRIBING INTERACTING FERMIONS

In the extensive literature analysing the properties of the Hubbard model it has been found to exhibit not only a metal-insulator transition, but also features of antiferromagnetism, ferromagnetism, Luttinger liquid physics, and superconductivity [103, 104]. It has been studied under many different conditions, including, but not limited to, infinite and finite [105] system sizes, periodic [106] or twisted [107, 108] boundary conditions, attractive interactions [109], embedding on a 2-dimensional lattice [110, 111], etc.. It has also been treated by a number of analytical and numerical techniques. Analytical solutions rely on the systems integrability in 1-dimension [112] and follow the Bethe-Ansatz approach [106, 107, 113]. Numerical techniques include DMRG calculations [114], dynamical mean-field theory [115] and quantum Monte-Carlo simulations [116]; though it is often used as a test bed for new techniques [87], as is also the case here [2]. For a thorough comparison of a variety of different approximate methods see [117]. Both $T = 0$ and $T > 0$ properties of a two dimensional Hubbard model on square lattice are benchmarked using 9 different techniques, including DMRG and Monte Carlo, comparing energies and double occupancy patterns.

The Hubbard model has gained particular attention due to its simplicity, yet its ability to predict the behaviour of more complicated physical systems. This is a feature of universality – the Hubbard model ignores many of the complications present in real models; however, its universal, non-trivial, features remain important in understanding them [104].

The model Hamiltonian

In this study we restrict to a 1-dimensional chain of spin-$\frac{1}{2}$ fermions, with creation (annihilation) operator $c^\dagger_{j,s}$ ($c_{j,s}$) for a fermion at site j and spin $s \in \{\uparrow, \downarrow\}$, with a local repulsive interaction $U \geq 0$ and open boundary conditions. The Hamiltonian for L sites is

$$\hat{H} = \sum_{j,s} \left[-J \left(c^\dagger_{j,s} c_{j+1,s} + \text{h.c.} \right) + \nu_j \hat{n}_{j,s} \right] + U \sum_j \hat{n}_{j,\uparrow} \hat{n}_{j,\downarrow}, \tag{4.37}$$

where $\hat{n}_{j,s} = c^\dagger_{j,s} c_{j,s}$ is the number operator for spin-s fermions at site j, ν_j is an onsite potential, and J is the amplitude for hopping between lattice sites. From here on, for simplicity, we work in units of J by setting $J = 1$.

Important symmetries of the Hamiltonian

The total number of each spin species $N_\uparrow = \sum_j \hat{n}_{j,\uparrow}$ and $N_\downarrow = \sum_j \hat{n}_{j,\downarrow}$ commute with the Hamiltonian $[\hat{H}, N_s] = 0$, and so does their sum $N = N_\uparrow + N_\downarrow$. The magnetisation is given by $S^z = \frac{1}{2}(N_\uparrow - N_\downarrow)$, which also commutes with the Hamiltonian. We may therefore choose the pair (N, S^z) as good quantum numbers for the model. These operators both generate $U(1)$ transformations of the Hamiltonian – N gives invariance under global gauge transformations and S^z gives rotations about the S^z axis.

The total spin operator is $\mathbf{S}_{\text{tot}} = (S^x, S^y, S^z)$, where $S^\alpha = \frac{1}{2}\sum_j \sum_{s,s'} c^\dagger_{j,s}(\sigma^\alpha)_{s,s'}c_{j,s'}$ and $(\sigma^\alpha)_{s,s'}$ picks out elements of the 2×2 Pauli matrix σ^α. Eigenvalues of the total spin operator are given by $\mathbf{S}^2 = S(S+1)$, where S is the spin of the eigenstate. If $S \propto N$ the model is ferromagentic, whereas for $S = 0$ it is anti-ferromagnetic. All operators S^α obey $[H, S^\alpha] = 0$, so the Hamiltonian is invariant under global spin rotations and thus has an $SU(2)$ symmetry. The use of symmetries allow eigenstates to be grouped in sectors that reduce the dimension of the Hilbert space where desired solutions exist, for e.g. a gauge symmetry implies particle number conservation so the Hilbert space can broken up into sectors of fixed N and the $SU(2)$ symmetry gives sectors of conserved S.

Another useful symmetry is a particle-hole symmetry $\mathcal{P}$, given by $\mathcal{P}c^\dagger_{j,s}\mathcal{P}^\dagger = (-1)^j d_{j,s}$ and $\mathcal{P}c_{j,s}\mathcal{P}^\dagger = (-1)^j d_{j,s}$, where $d^\dagger_{j,s}(d_{j,s})$ are fermionic operators related to the old operators by $d^\dagger_{j,s}d_{j,s} = 1 - c^\dagger_{j,s}c_{j,s}$. When the chemical potential is set to zero everywhere, i.e. $\nu_j = 0$ for all j, the Hamiltonian transforms as $H(U) \to H(U) - U(L - N)$ that gives a symmetric spectrum about half-filling. Thus, reducing the number of states required to be determined. There are a variety of symmetries that are important and utilised in the Bethe ansatz approach to diagonalise the Hamiltonian [103]. In fact, as the model is integrable it has an infinite set of commuting operators in the thermodynamic limit [112].

Phases of the half-filled Hamiltonian

At half-filling, with $(N, S^z) = (L, 0)$, the model has two phases: a conducting phase at $U = 0$ and a Mott-insulator phase for all $U > 0$ [106]. However, for very small system sizes and with anisotropic local potentials the conducting phase

extends by a small amount into the insulating phase. This results in a *crossover* region, indicated in Fig. 4.2, that makes the Hubbard model (and specifically the $L = 2$ dimer) a useful tool when exploring the effect of correlations on the KS groundstate and the optimal free state. Evidence for the crossover region is given in the next section.

For the dimer, in order to define an optimal entanglement model it is required to identify the frozen degrees of freedom in the Mott-insulator phase that the KS model fails to capture. It is then possible to build a Hamiltonian that has the remaining degrees of freedom in the insulating phase and the optimal free state as its ground state.

4.5.2 Entanglement properties of the Hubbard dimer

Restricting the Hamiltonian in Eq. (4.37) to $L = 2$ sites at half-filling $N_\uparrow = N_\downarrow = 1$ results in the Hamiltonian

$$\hat{H} = \sum_{s\in\{\uparrow,\downarrow\}} \left[-(c^\dagger_{1,s}c_{2,s} + c^\dagger_{2,s}c_{1,s}) + \nu_1 n_{1,s} + \nu_2 n_{2,s}\right] + U(n_{1,\uparrow}n_{1,\downarrow} + n_{2,\uparrow}n_{2,\downarrow}). \tag{4.38}$$

The Hilbert space is spanned by basis vectors $\mathcal{H} \in \{|\uparrow\downarrow, 0\rangle, |\uparrow,\downarrow\rangle, |\downarrow,\uparrow\rangle, |0,\uparrow\downarrow\rangle\}$, where the notation $|\alpha,\beta\rangle = |\alpha\rangle \otimes |\beta\rangle$ corresponds to α fermions at site 1 and β fermions at site 2. An eigenstate of this Hamiltonian $|\Psi\rangle = a_1|\uparrow\downarrow, 0\rangle + a_2|\uparrow,\downarrow\rangle + a_3|\downarrow,\uparrow\rangle + a_4|0,\uparrow\downarrow\rangle$, may be expressed in vector notation $|\Psi\rangle = (a_1, a_2, a_3, a_4)^T$. It is possible to construct a matrix representation of the Hamiltonian that may be diagonalised directly to find the eigenstate amplitudes $\{a_j\}$ and the corresponding energy, E.

Full solution to interacting model

The Hamiltonian, whilst respecting the basis ordering given above and fermionic anti-commutation, is

$$\hat{H} = \begin{pmatrix} U+\nu & -1 & 1 & 0 \\ -1 & 0 & 0 & -1 \\ 1 & 0 & 0 & 1 \\ 0 & -1 & 1 & U-\nu \end{pmatrix}, \tag{4.39}$$

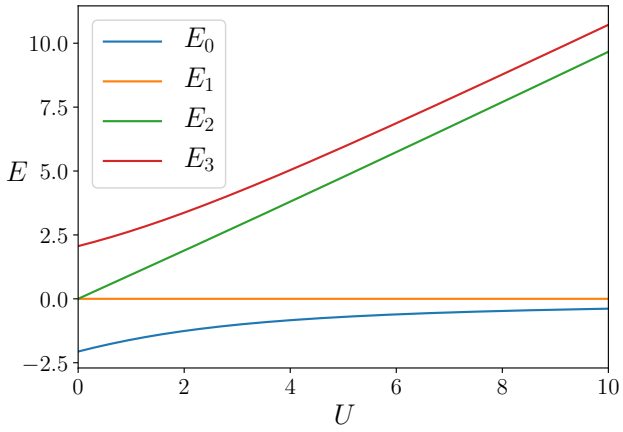

Figure 4.3: Eigenvalues of the half-filled Hubbard dimer, given in Eq. (4.40), with varying U and constant $\nu = 0.5$.

where $\nu = \nu_1 - \nu_2$. This includes a shift in the energy scale by $-(\nu_1 + \nu_2)$ so that the Hamiltonian depends only on the difference between potentials ν and the interaction strength U, i.e. we reduce the number of variables from three to two. Now, using the Schrödinger equation $\hat{H}\,|\Psi\rangle = E\,|\Psi\rangle$, the energies of $\hat{H}$ are found to be [118]

$$\begin{aligned} E_0 &= r\cos\left(\frac{\theta+2\pi}{3}\right)+\frac{2U}{3}; & E_1 &= 0; \\ E_2 &= r\cos\left(\frac{\theta+4\pi}{3}\right)+\frac{2U}{3}; & E_3 &= r\cos\left(\frac{\theta}{3}\right)+\frac{2U}{3}; \end{aligned} \tag{4.40}$$

with $r = \frac{2}{3}(U^2+3\nu^2+12)^{\frac{1}{2}}$ and $\theta = \arccos\left[\frac{8U(9\nu^2-U^2-18)}{27r^3}\right]$. The ordering of levels was determined by plotting each energy as a function of U with fixed $\nu > 0$, see Fig 4.3.

The corresponding (unnormalised) eigenstates are

$$|\Psi\rangle_{E\neq 0} = \begin{bmatrix} \frac{2}{U+\nu-E} \\ 1 \\ -1 \\ \frac{2}{U-\nu-E} \end{bmatrix} \qquad \text{and} \qquad |\Psi\rangle_{E=0} = \begin{bmatrix} 0 \\ 1 \\ 1 \\ 0 \end{bmatrix}. \tag{4.41}$$

It is clear that in the $U \to \infty$ limit the groundstate energy E_0 approaches $E_1 = 0$. In this limit the double occupancy states have amplitudes $\sim \frac{2}{U} \to 0$ that approach

zero, as Coulomb repulsion becomes dominant. However, the eigenstates corresponding to E_0 and E_1 remain orthogonal and form the lower Hubbard band. The excited states E_2 and E_3 also approach each other as U increases, thus forming the upper Hubbard band. The gap between the upper and lower bands is called the Mott gap and it scales with U. The gap does not exist at $U = 0$ where quantum fluctuations dominate. The dimer highlights the Mott gap quite clearly; it persists for all system sizes up to the thermodynamic limit $L \to \infty$ for $U > 0$. We would now like to study the entanglement properties of the groundstate $|\Psi_0\rangle$ corresponding to E_0.

Entanglement spectrum of the half-filled Hubbard dimer

Following the introduction to the entanglement spectrum in section 2.3.2 it is clear that the eigenstates found above, in the fermion representation with basis states $\{|\uparrow\downarrow, 0\rangle, |\uparrow, \downarrow\rangle, |\downarrow, \uparrow\rangle, |0, \uparrow\downarrow\rangle\}$, are already expressed in Schmidt form when a partition is made between sites 1 (subsystem A) and 2 (subsystem B). This is clear as each state in subsystem A is orthogonal, likewise for subsystem B. Further, each state in A uniquely determines the state in B. Therefore, eigenvalues of the reduced density matrix $\rho = \mathrm{Tr}_B |\Psi\rangle\langle\Psi|$ can be read directly from the (normalised) eigenstate. They are $\rho_j \in \{\frac{4}{Z(U+\nu-E_0)^2}, Z^{-1}, Z^{-1}, \frac{4}{Z(U-\nu-E_0)^2}\}$ with E_0 given in Eq. (4.40) and $Z = \sum_j \rho_j$. It is clear that there exists a degenerate pair of ρ_j and two levels that differ by the sign of ν in the denominator. In the large U limit we expect these non-degenerate levels to also become degenerate as U becomes dominant. The purpose of the anisotropic local potentials is now clear: without it the spectrum would have a pair of two-fold degenerate levels for any parameter value, that always returns $D_{\mathcal{F}} = 0$ due to Eq. (4.18b).

From this set of levels we may proceed and calculate the interaction distance $D_{\mathcal{F}}$ using the analytical solution for the four-level spectrum given in section 4.3.2. To do so, we first require to order the states from largest to smallest, with the ordering $\rho_j \geq \rho_k$ for $j < k$. See Fig. 4.4 where the levels are plotted for varying U. It is most illuminating in this figure to not label the levels by their sorted order, but instead as $\{\tilde{\rho}_{+\nu}, \tilde{\rho}_d, \tilde{\rho}_d, \tilde{\rho}_{-\nu}\}$ where the subscripts are clear from the discussion above; only one of the degenerate levels $\tilde{\rho}_d$ has been plotted. The ordering makes

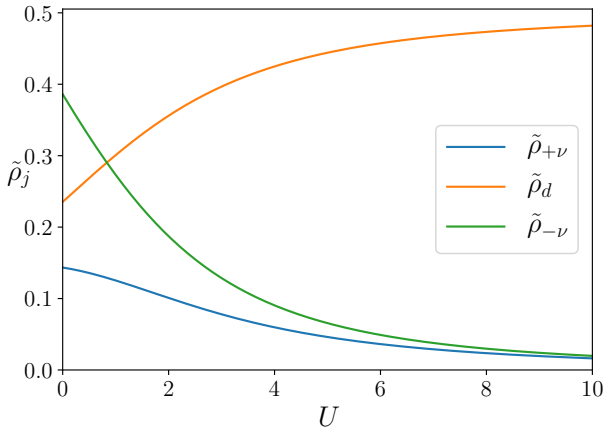

Figure 4.4: Eigenvalues $\{\tilde{\rho}_j\}$ of the reduced density matrix ρ with varying U and constant $\nu = 0.5$. The levels are found using the groundstate given in Eq. (4.41). The plot highlights the ordering of levels required to calculate $D_{\mathcal{F}}$. The level $\tilde{\rho}_d$ (orange) is two-fold degenerate. Labels in the main text without tilde are reserved for the ordered set of levels.

perfect sense: in the large U limit the dominant entanglement levels are those corresponding to singly occupied states in each subsystem. We see that for U beyond ~ 1 this is the case. For $U \lesssim 1$ the level corresponding to the entangled mode $|0\rangle \otimes |\uparrow\downarrow\rangle$ is the most probable as the presence of $\nu = \nu_1 - \nu_2 > 0$ favours occupations at site 2. The other levels can be explained by similar arguments.

As a final note before calculating $D_{\mathcal{F}}$, the entanglement spectrum only splits into upper and lower Hubbard bands beyond the value of $U_c \sim 1$. Therefore the Mott gap does not exist for all $U > 0$, but is present only beyond the crossover value U_c. It is not clear from the energy spectrum alone where the crossover occurs, making the entanglement spectrum a useful tool for probing the phase of this system. The crossover indicates when the dominant behaviour changes from quantum fluctuations due to tunnelling to the formation of magnetic moments due to Coulomb repulsion.

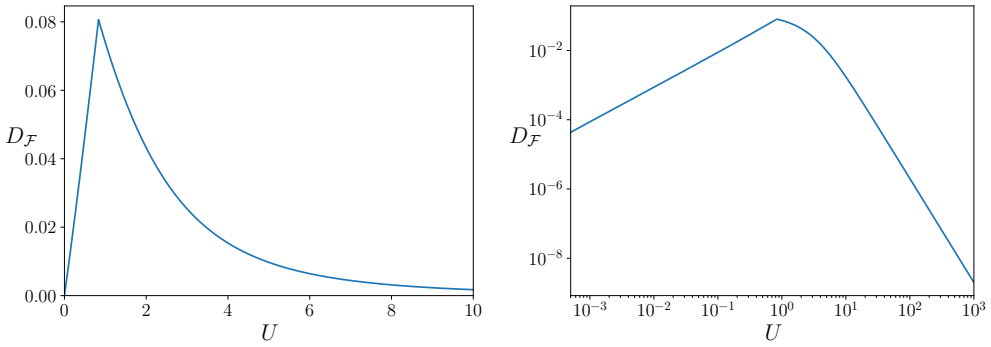

(a) (b)

Figure 4.5: The interaction distance of the groundstate, with fixed $\nu = 0.5$ and varying U, calculated using Eqs. (4.18b) and (4.41). In (a) the range of U is reduced, showing the growth from the non-interacting point $U = 0$ with $D_{\mathcal{F}} = 0$ to the crossover at $U = U_c$. In (b) the range of U is extended, with logarithmic scaling in both axes, showing the decay to $D_{\mathcal{F}} = 0$ beyond $U = U_c$.

Interaction distance of the groundstate

We are now in a position to calculate the interaction distance using the spectrum of ρ. It is found (via a computer) that for all values of U the inequality $\rho_1 < (\rho_1 + \rho_2)^2$ holds. Therefore, as discussed in section 4.3.2, the optimal free state is found by matching the largest two eigenvalues of ρ and $D_{\mathcal{F}}$ is always given by Eq. (4.18b). In Fig. 4.5 the interaction distance is plotted against U.

At $U = 0$ the system consists of free fermions that may hop between sites, without interaction, giving an expected $D_{\mathcal{F}} = 0$ (see Fig. 4.5a). As the interaction is turned on the effect of Coulomb repulsion begins mixing the single-particle states, moving the system away from its free description. Up to the crossover U_c, charge fluctuations remain dominant. In agreement with Fig. 4.4, U_c is indicated by a discontinuity in the derivative of $D_{\mathcal{F}}$. The crossover occurs at $U_c = 0.8334$ and $D_{\mathcal{F}}(\rho)\big|_{U=U_c} = 0.0806$. As a reference, this value is approximately half the maximum interaction distance $D_{\mathcal{F}}^{\max} = \frac{1}{6} \approx 0.1667$ for a four-level spectrum, that was calculated in [19]. Moving away from U_c and spin fluctuations begin to dominate, quickly (as evidenced by the sharp slope in 4.5b) fixing spins to lattice sites. This reduces $D_{\mathcal{F}}$ as its peak occurs when there are maximal spin *and* charge

fluctuations.

That $D_{\mathcal{F}} \to 0$ as $U \to \infty$ is an artefact of the freezing of double occupancy (or charge) degrees of freedom, resulting in the spins being effective free particles. Without charge fluctuations, each site is occupied by an up or down spin and is free to point in either direction. Of course, to preserve $N_\uparrow$ and $N_\downarrow$ the spins must form an entangled pair. This describes the maximally entangled singlet state $|\Psi\rangle = \frac{1}{\sqrt{2}} = [|\uparrow,\downarrow\rangle - |\downarrow,\uparrow\rangle]$, that has zero energy. Moving slightly away from the infinite limit and charge fluctuations will be present allowing for double occupations. However, the energy cost for doing so is of the order of the Mott gap $\sim U$ so the system still has a close to free description and $D_{\mathcal{F}}$ reflects this by being small.

Explicit expression for the interaction distance

By finding an explicit expression for the interaction distance it is possible to determine exactly how fast $D_{\mathcal{F}}$ decays from the crossover and into the insulating phase. Using the results from the previous two sections, the interaction distance is given by

$$D_{\mathcal{F}}\big|_{U>U_c} = \left|\frac{b-a}{ab+2a+2b}\right|, \tag{4.42}$$

where $a = (U+\nu-E_0)^2$ and $b = (U-\nu-E_0)^2$. With this expression it is possible to us a Taylor expansion about $1/U = 0$. However, the form of the energy, given in Eq. (4.40), does not lend itself to the calculation. By approximating $E \approx -4/U$ the calculation becomes tractable. This is the known effective ground-state energy in the strong coupling regime following a second-order perturbative expansion [22]. With this approximation we obtain the following expansion for the interaction distance in the strongly correlated limit $U \gg 1$

$$D_{\mathcal{F}} \approx \frac{4\nu}{U^3} + \frac{8\nu^3 - 64\nu}{U^5} + \mathcal{O}\left(U^{-7}\right), \tag{4.43}$$

where subsequent terms continue in odd powers of $1/U$. From this analysis we see that the interaction distance decays very quickly in the insulating phase. The dominant term in $D_{\mathcal{F}}$ decays with U^{-3} whilst the dominant term in E_0 decays with U^{-1}. Thus, the bipartite correlations approach the infinite interaction limit quicker than the energy.

4.5.3 Kohn-Sham and optimal entanglement models for the Hubbard dimer

The calculations in the previous subsection show that the Hubbard dimer has two competing behaviours arising from quantum tunnelling and from Coulomb repulsion, where the dominant behaviour is separated by a crossover point. The inequality in Eq. (4.36) predicts that the ground state of the corresponding KS model will be close to optimal for atleast $U \ll U_c$. Its behaviour as $U \to U_c$ from below is a little more uncertain; however, we have seen that within $U < U_c$ the degrees of freedom of the groundstate remain the same as at $U = 0$ so we may also expect the KS model to be close to optimal up to this point. However, beyond $U = U_c$ the bound in (4.36) does not hold. The KS formalism has no means of detecting the freezing of double occupancies so will undoubtedly result in large errors in predicting bipartite correlations. Before making this analysis complete, we build a Hamiltonian with the optimal free state as its groundstate in the strongly correlated limit.

Requirements of the optimal entanglement model

The aim now is to build a non-interacting auxiliary Hamiltonian H_{aux} that has the optimal free state σ as its groundstate. We can do so with the ideas of KS theory in mind: interaction effects are tuned by defining an appropriate potential term in the Hamiltonian that reproduces a property of choice. Here we wish to reproduce the bipartite correlations of σ, that by the inequality in Eq. (4.26) should produce all observables within the bound of $D_{\mathcal{F}}$. This has an advantage over the KS system, where in principle it is possible to produce all observables, as we saw in the previous sections that correlations are important when characterising features of many-body systems.

In order to define a Hamiltonian that reproduces the optimal free state it is important to know exactly what spectrum we are aiming for. For all U we saw that as $\rho_1 < (\rho_1 + \rho_2)^2$ then the interaction distance is found using Eq. (4.18b). Consequently, the free parameter solutions in Eq. (4.19b) give the correct set of $\{\sigma_j\}$. In the limit of $U > U_c$, that is currently our focus, $\rho_1 = \rho_2$ that correspond to single occupancy modes. Therefore, the free parameter solutions

are $(b_1, b_2) = (0, 2\rho_1 - \frac{1}{2})$. The existence of a zero solution means that the optimal state will have two sets of degenerate levels, i.e. $\sigma_1 = \sigma_2$ and $\sigma_3 = \sigma_4$.

Defining an optimal entanglement model

The optimal free state can be found by defining a Hamiltonian consisting of two non-interacting two site chains, each with a single spinless fermion, with creation (annihilation) operator $c_j^\dagger(c_j)$, see the inset of Fig. 4.6. Then, appropriately tuning a local chemical potential at one of the sites freezes occupations away from that site, mimicking the freezing of double occupations due to Coulomb repulsion. By making a partition such that sites $1, 2$ are subsystem A and $3, 4$ are subsystem B, the resulting entanglement spectrum is that of the optimal free state. The Hamiltonian for this auxiliary model is

$$\hat{H}_{\text{aux}} = -\left(c_1^\dagger c_3 + c_3^\dagger c_1\right) - \left(c_2^\dagger c_4 + c_4^\dagger c_2\right) + \frac{\mu}{2} c_1^\dagger c_1 \tag{4.44}$$

where $\mu = 2\left[\sqrt{\frac{\sigma_1}{\sigma_3}} - \sqrt{\frac{\sigma_3}{\sigma_1}}\right]$. For the four-level system these levels may be expressed in terms of the interacting levels ρ_j and therefore also the parameters of the interacting Hamiltonian (4.37), however the form here is certainly more presentable. See Fig. 4.6 where the behaviour of μ is given, the linear growth beyond U_c gives that $\mu \approx U$. Note that at present there is no constructive way to produce the potential μ without prior knowledge of the desired optimal entanglement levels.

The specific form of the auxiliary Hamiltonian is motivated by the simplicity of spinless free-fermionic models. They are always exactly solvable and have a finite number of tunable parameters: a fermion can only hop between sites, give energy to Cooper pairs, or be influenced by a local potential. The choice of hopping in H_{aux} is fixed to imitate that of spinful fermions in the non-interacting Hubbard dimer. Pairing terms are omitted that may render the state topological (which is not our aim), leaving local potential terms as free variables to imitate the effect of interactions. This is not a unique construction and it would be interesting to see what other constructions are capable of producing the optimal free state.

To see why the degeneracies of optimal spectrum are important consider the full and reduced Hilbert space for this system. The full Hilbert space is $\mathcal{H} \in$

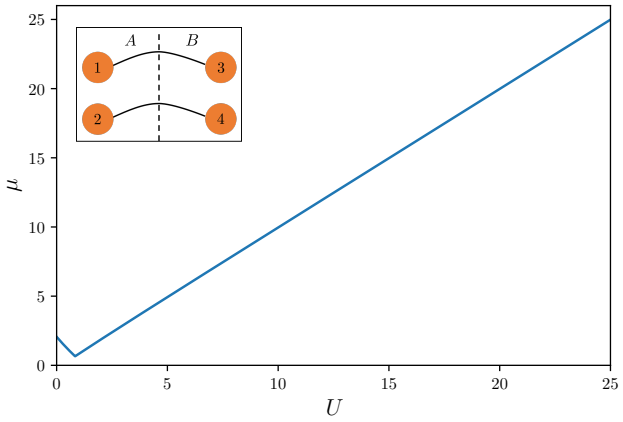

Figure 4.6: The exact value of the chemical potential μ for varying U and fixed $\nu = 0.5$. The purpose of μ is to imitate the effect of interactions in the Hubbard dimer. In the strongly correlated regime $U > U_c$, the linear growth suggests that $\mu \approx U$. Inset: A sketch of the strongly correlated optimal entanglement model, as defined in Eq. (4.44). The model consists of two non-interacting chains with a single spinless fermion allowed to hop, across solid lines, on each chain. A chemical potential is applied to site 1 to have the correct optimal free state as its groundstate.

$\{|1100\rangle, |1001\rangle, |0110\rangle, |0011\rangle\}$, where each local Hilbert space corresponds to an empty $|0\rangle$ or filled $|1\rangle = c^\dagger |0\rangle$ site, with an assumed tensor product structure. The reduced Hilbert space for subsystem A is therefore $\mathcal{H}^A \in \{|11\rangle, |10\rangle, |01\rangle, |00\rangle\}$. These have a very similar structure to the dimer Hilbert space introduced in section 4.5.2: they are of the same dimension and the states in A uniquely determine the states in B. The effect of the chemical potential is to reduce occupation at site 1, whilst favouring occupation at site 3. At the same time, sites 2 and 4 share equally the probability for occupation. Therefore, μ (equally) reduces the probability of modes $|11\rangle$ and $|10\rangle$, whilst having the opposite effect on modes $|01\rangle$ and $|00\rangle$. Recognising that there exists a double degeneracy in the spectrum is pivotal to the success of this auxiliary model, though it would not be unreasonable to propose an auxiliary model that has the effect of distributing levels in some other way by use of different local potentials. Before discussing the results it is worth

taking a moment to understand the procedure used for relating observables of models in a different basis.

Determining local density (and other observables) from reduced spectra

When calculating physical quantities, e.g. local electron density, of the auxiliary model there is some interpretation required to accurately predict properties of the interacting model. For example, for the auxiliary model defined in Eq. (4.44) that models the strongly correlated limit of the Hubbard dimer, the effect of the chemical potential is to reduce occupations at one of the four sites. If one was to measure density at sites 1 and 2 (or region A) of the auxiliary model in the basis that it is built in, then it would not give the same density as the two spin occupations at site 1 (region A) of the interacting model – in the $U \gg 1$ limit the auxiliary groundstate has an expectation value of total density in region A to be $\langle \hat{n}_A \rangle_{\text{aux}} \approx \frac{1}{2}$ whereas the interacting model has $\langle \hat{n}_A \rangle_{\text{int}} \approx 1$.

The optimal entanglement model is an auxiliary model constructed to produce the entanglement spectrum of the optimal free state. As such, the applicability of the bound $D_n \leq CD_{\mathcal{F}}$ depends on the basis that the spectrum is measured in. In order to extract the correct local electron density from the optimal entanglement model requires measurement in the Schmidt basis of the interacting system, in agreement with the result for $\langle \hat{n}_j \rangle_{\text{int}} = \text{Tr}\left[\hat{n}_j \rho\right]$. With the entanglement spectrum of the auxiliary model $\{\alpha_k\}$, the correct density is found by calculating the following for different configurations of α_k:

$$\langle \hat{n}_j \rangle_{\text{aux}} = \sum_k \langle \psi_k | \hat{n}_j | \psi_k \rangle \alpha_k, \tag{4.45}$$

where $|\psi_k\rangle$ is a Schmidt vector in region A of the interacting model. One configuration of α_k gives the correct density distribution within $CD_{\mathcal{F}}$ of the interacting model. For the Hubbard dimer example, it is the configuration ordered in the same relative size order as the interacting levels that gives the correct density distribution. Note that when an auxiliary model can be defined with the same physical degrees of freedom as the interacting model, e.g. the KS model, then there is no minimisation over configurations required.

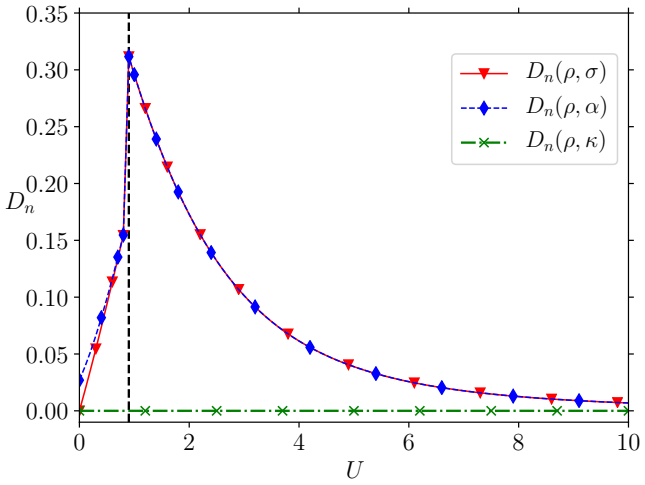

Figure 4.7: Density difference between the interacting state, ρ and each of the optimal, σ, auxiliary, α and KS κ states, with varying U and fixed $\nu = 0.5$. The vertical dashed line shows the maximum density difference where there is a crossover at $U_c = 0.9$ from one behaviour to another. We see that, for all values of U, κ accurately predicts the groundstate density. On the other hand, σ and α, that give identical results for $U > U_c$, approach zero when U is large due the upper bound of D_n with $D_{\mathcal{F}}$ found in Eq. (4.30).

Numerical analysis of auxiliary models

Having defined an optimal entanglement model we are now in a position to test the applicability of it, compared with the KS model. We compare: the interacting, ρ, the optimal free, σ, the KS, κ, and the auxiliary, α states, using a variety of measures. In particular, we measure the density difference D_{n} in Fig. 4.7, the trace distance D_{tr} in Fig. 4.8a, and the entanglement entropy S in Fig. 4.8b.

Beginning with Fig. 4.7 where the density difference metric is calculated, the local densities corresponding to κ are within 10^{-6} of the interacting state density for all values of U. This is an artefact of the exact method used and is an expected result. For the optimal free state, at $U = 0$ it captures the density exactly as ρ is explicitly free. Likewise as U is increased beyond the crossover, where we expect the interaction distance to decrease rapidly as evidenced in Fig 4.5, the density metric also decreases rapidly due to the bound in Eq. (4.30). The constant in the

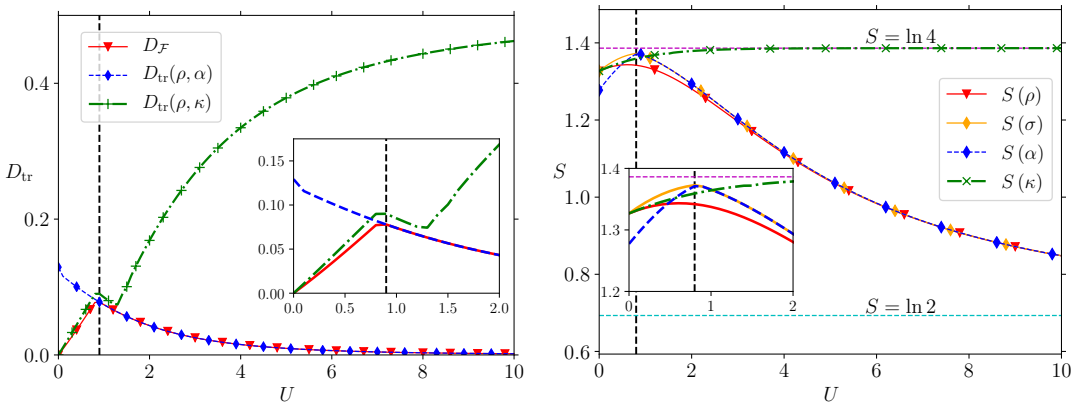

(a) (b)

Figure 4.8: (a) Trace distance metric between the interacting state ρ and each of the optimal σ, auxiliary α and KS κ states. (b) Entanglement entropy for ρ, σ, α, and κ states. Both figures vary U with fixed $\nu = 0.5$, and the black dashed line shows where the crossover point $U_c = 0.9$. The value of U_c found in this figure is consistent with Fig. 4.7. The insets of (a) and (b) show the same data zoomed into the region of the crossover. Surprisingly, κ remains close to optimal for a small range of U even beyond U_c and diverges after a kink in both (a) and (b), though in (b) it is not so obvious even in the inset.

bound takes the value 4 for the dimer, as the maximum of the density operator is 1 that is summed over all occupations. In the strongly correlated limit the inequality is saturated, giving $D_{\mathcal{F}} = 4D_{\rm n}(\rho,\sigma)$, so that $D_n(\rho,\sigma) \sim U^{-3}$ consistent with $D_{\mathcal{F}}$.

The optimal entanglement model, with groundstate α, fails to capture the correct density even at $U = 0$. This is due to the definition of $H_{\rm aux}$, where the local potential at site 1 does not have the same effect as turning off interactions in the interacting Hamiltonian, where there is a local potential acting on both spin-up and spin-down fermions. It is of no concern as the success of α lies beyond the crossover. Beyond U_c the density of α matches σ, by construction. There appears to be a discontinuity in both $D_{\rm n}(\rho,\sigma)$ and $D_{\rm n}(\rho,\alpha)$. This is an artefact of the optimal free state drastically changing behaviour at the crossover from one free manifold to another, as depicted in Fig 4.2.

We now move to Fig. 4.8, where both measures are of entanglement between subsystems A and B. Of course, the entanglement entropy is built from the entanglement spectrum so we expect the information in (a) and (b) to be complementary, see section 2.3.3. In (a) the interaction distance is plotted for the same parameter range as in Fig. 4.5 in the previous section, so that will not be discussed in any further detail here. In both (a) and (b) the auxiliary model agrees exactly with the optimal free state beyond U_c, by its construction. We see that its entropy reduces to $S = \ln 2$ signalling the freezing of degrees of freedom and a maximally mixed reduced density matrix. For $U < U_c$ it does not capture the entanglement features of ρ and, from (b), we see it has less entanglement. This is because the effect of the potential at site 1 restricts the quantum fluctuations in the upper chain.

On the other hand, the KS model shows agreement with the optimal free state up to the crossover and even slightly beyond. Beyond this, the error in approximating the correct entanglement is significant. This is due to the KS model failing to capture the freezing of degrees of freedom, as in (b) the entropy saturates at $S = \ln 4$ signalling a maximally mixed reduced density matrix with 4 degrees of freedom. Nevertheless it captures the correct density due the density being an average over all four states, $\langle n_{j,s} \rangle$.

4.6 Summary

In this chapter we aimed to quantify the applicability of the KS model and DFT through an interaction distance analysis. By defining an optimal entanglement model, a parent Hamiltonian to the optimal free state, we can use it as a tool to compare the success of the KS model against. The optimal free state has an entanglement spectrum that is built from single-particle levels and is the closest free spectrum to the interacting model, matching its low energy behaviour. Through the bound (4.26), when measured in an appropriate basis, the groundstate of the optimal entanglement model returns all observable quantities within the bound of the interaction distance.

Expanding the trace distance $D_{\mathrm{tr}}(\kappa, \sigma)$ and density distance $D_{\mathrm{n}}(\kappa, \sigma)$ about the non-interacting point for small deviations $n + \delta n$ from the exact density n,

we see that the KS model is not only accurate in local electron densities, but is also a good approximation to the optimal entanglement model in the perturbative regime. This is supported numerically, where the KS groundstate of the Hubbard dimer is a good approximation beyond the crossover to the Mott phase. Well into the strongly correlated regime the the KS model fails to reproduce the correct entanglement features and is limited by a fixed kinetic operator that restricts its ability to appropriately freeze degrees of freedom, due to the effect of interactions.

For the Hubbard dimer, we find that in the infinite interaction limit the interaction distance approaches zero. Through the bound $D_n(\rho, \alpha) \leq C D_{\mathcal{F}}$, with $D_{\mathcal{F}} \approx 0$ means that the optimal entanglement model has the same density distribution as the interacting model for large interactions, when measured appropriately. KS methods are known to fail when probing beyond a Mott transition, so the optimal entanglement model offers a constructive way to determine a groundstate with the correct ground state density in the Mott-insulator phase.

In future work we aim to find a constructive method for determining the optimal entanglement model. We envisage a method similar to DFT, but where one can tune the single-particle entanglement levels of the resulting groundstate through an external potential or other free fermionic terms in the Hamiltonian. Other works have aimed to combine DFT and strongly correlated systems, but these still rely on finding an appropriate functional. For e.g. in [119] the authors start with a Hamiltonian without a kinetic term and slowly turn it on to capture strongly correlated effects, but the form of the energy functional relating to the kinetic operator requires approximation. An open question is to test the behaviour of an exact groundstate found using this method and determine its applicability in a similar vain to the analysis of this chapter.

It would also be insightful to extend the Hubbard dimer analysis beyond the two site chain. This includes determining the extent of applicability of the KS model and also whether it is possible to define an optimal entanglement model for any system size.

4. EFFICIENCY OF THE KOHN-SHAM MODEL IN DESCRIBING INTERACTING FERMIONS

Chapter 5

Conclusions and outlook

In Chapter 1, the work in this thesis was motivated through the application of novel ideas to quantum technologies – a research area that is vast and ongoing. There were two main aims focussed on in this work: to understand the topological phase of models with potential applications to quantum computing and to find new and efficient ways of modelling strongly correlated systems. These aims are very broad and the results presented here are by no means exhaustive. However, the contribution of these works opens up new questions for future study that will be outlined in the remainder of this Chapter.

The extended Majorana chain

For the first of these aims we studied an extended Kitaev chain. This model is a generalisation of the local Kitaev chain where the hopping and pairings are extended over all sites with a variable power-law decaying exponent. The exponent can be tuned between the local model and an infinite range model with all sites coupled with equal amplitude. We definitively showed the existence of edge Majorana modes in the extended chain, as is the case for the local chain. By analysing a closed chain with periodic or antiperiodic boundary conditions, it is not possible to correctly approach the infinite limit and a confirmation of edge modes is limited to the study of an appropriate topological invariant. This can be avoided by looking directly at an open chain to derive specific features of the topological phase. We analysed the extreme case, infinite range couplings, by

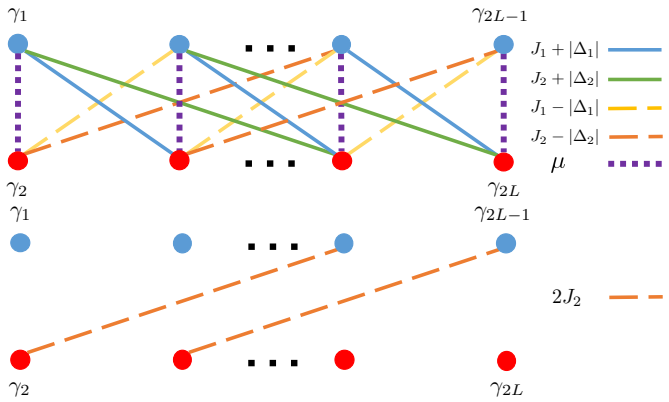

Figure 5.1: Pictorial representation of the Hamiltonian terms in a Majorana representation of an extended Majorana chain with variable couplings parameters. (top) All couplings for a chain that extends to next-nearest neighbour at most. (bottom) A special case with $J_1 = \Delta_1 = \mu = 0$ and $J_2 = -|\Delta_2| > 0$, exposing two Majoranas at each end. Thus, the Hamiltonian requires the full $\mathbb{Z}$ classification of the BDI symmetry group.

using of a generating function method that was modified for a non-local model. Using this method it was possible to expose exponentially localised edge modes at zero energy on a semi-infinite chain and non-zero energy modes on a finite chain, where a $\mathbb{Z}_2$ topological invariant is a sufficient classification of the model.

It would be interesting to see whether the generating function method can be applied to other models, including chains requiring $\mathbb{Z}$ classification. A $\mathbb{Z}$ classification implies that it is possible to have more than one Majorana at each boundary. An example of this was given in [69], where hopping and pairing couplings are indexed by their range, for e.g. nearest neighbour hopping would be J_1, next-nearest neighbour J_2 and so on. Then, by switching off certain couplings one can achieve multiple Majorana end modes. As an example, allow couplings to extend over a maximum of two sites and switch off the nearest neighbour couplings $J_1 = \Delta_1 = 0$ with $\mu = 0$. When $J_2 = -\Delta_2 > 0$ the resulting chain has two zero energy Majoranas per end, see Fig. 5.1. This construction can be manipulated to produce any desired number of Majoranas at each edge, providing the couplings extend sufficiently along the chain and they are tuned appropriately.

At present, this construction is quite unphysical. However, application of an analytical approach may expose novel features that deem the construction useful.

By probing the single-particle correlations we found that non-local couplings change the known signature of a topological phase in its entanglement spectrum and the localisation properties of the midgap single-particle entanglement modes. Making a partition of a local chain has the effect of forming a virtual boundary at the partition that is host to a virtual edge mode. When a single partition is made, entanglement localises at the virtual edge and decays exponentially into the subsystem forming a single zero energy midgap state. Extending to long-range couplings and a single partition results in two midgap states with energies split from zero. Thus, the entanglement Hamiltonian must contain long-range terms to account for the non-zero energy. As the entangled mode shows where entanglement is localising, it must be that the non-local coupling between all sites allows for entanglement to extend more than exponentially close to the partition. As an open question, it would be interesting to study the scaling of correlations in the long-range model. For short range interactions it was proven by Hastings [79] that the presence of a gap implies exponentially decaying correlations: does that hold here? In [64], the authors found that extending only pairing terms resulted in an algebraic decay of correlations. This may explain why the physical edge couples with the virtual edge in our study.

Applicability of the Kohn-Sham model

For the second major aim of the thesis, we aimed to quantify the applicability of the KS model through an interaction distance analysis. The KS model is a free auxiliary with density functional theory at its core. It is successful in approximating local electron densities and other observables when an exchange-correlation functional can be accurately defined. The interaction distance measures how far a given quantum state is from the manifold of all free states, through a minimisation over all free entanglement spectra. It is thus a useful tool for comparing the KS model with all other possible free states. We found that in the weakly interacting limit there exists a tight bound on how close the KS state is to the

optimal free state. Beyond this limit, the KS model provides accurate local densities, but has unbound errors on correlations due to the fixed form of the kinetic operator. To rectify this, we proposed an optimal entanglement model that has the optimal free state as its ground state.

The optimal entanglement model can be considered both physically and conceptually. In this work we aimed to approach from the 'physical' side, by defining a non-interacting model that reproduces the entanglement spectrum of the Hubbard dimer in the strongly correlated limit where the KS model fails. By its construction, the auxiliary model defined produced the correct spectrum. However, this study was limited to a small system size where we could feed in the desired solution. This leads to a (hard) open question: is it possible to produce the optimal free state without prior knowledge of the solution? This idea is akin to DFT, where no prior knowledge of local density is needed to achieve the desired result and a variational method is used to find the minimum. The optimal entanglement model is certainly not unique as it is possible to make any choice of Hilbert space to construct it from. It would be desirable to find a basis that allows for a direct measurement of physical quantities without the need for reordering entanglement levels with the same ordering as the interacting model.

From the conceptual side, the optimal entanglement model is a tool to compare against. When attempting to approximate complex systems with free fermions one may ask the question, is this a good approximation to the optimal entanglement model. If the answer is no, then the approximate method being used is not optimally capturing the bipartite correlations, which may lead to errors in its analysis. It would be interesting to quantify the applicability of other free approximations, such as mean-field theory or other flavours of DFT, by building a catalogue of bounds to compare each approximation against another.

References

[1] Kristian Patrick, Titus Neupert, and Jiannis K. Pachos, Topological quantum liquids with long-range couplings, *Physical Review Letters* **118**, 267002 (2017). i, 42, 43, 53

[2] Kristian Patrick, Marcela Herrera, Jake Southall, Irene D'Amico, and Jiannis K. Pachos, Efficiency of free auxiliary models in describing interacting fermions: From the Kohn-Sham model to the optimal entanglement model, *Physical Review B* **100**, 075133 (2019). i, 76, 82, 85, 94, 96

[3] Kristian Patrick, Vincent Caudrelier, Zlatko Papić, and Jiannis K. Pachos, Interaction distance in the extended XXZ model, *Physical Review B* **100**, 235128 (2019). ii, 76

[4] Horst L. Stormer, Nobel Lecture: The fractional quantum Hall effect, *Reviews of Modern Physics* **71**, 875 (1999). xi, 9

[5] David Deutsch and Richard Jozsa, Rapid solution of problems by quantum computation, *Proceedings of the Royal Society of London. Series A: Mathematical and Physical Sciences* **439**, 553 (1992). 1

[6] Peter W. Shor, Polynomial-time algorithms for prime factorization and discrete logarithms on a quantum computer, *SIAM review* **41**, 303 (1999). 1

[7] Lov K. Grover, A fast quantum mechanical algorithm for database search, preprint quant-ph/9605043 (1996). 1

[8] David P. DiVincenzo, The physical implementation of quantum computation, *Fortschritte der Physik: Progress of Physics* **48**, 771 (2000). 2

[9] A. Yu Kitaev, Fault-tolerant quantum computation by anyons, *Annals of Physics* **303**, 2 (2003). 2, 15

[10] Chetan Nayak, Steven H. Simon, Ady Stern, Michael Freedman, and Sankar Das Sarma, Non-Abelian anyons and topological quantum computation, *Reviews of Modern Physics* **80**, 1083 (2008). 2, 14

[11] Jiannis K. Pachos, Introduction to topological quantum computation, Cambridge University Press (2012). 2

[12] A. Yu Kitaev, Unpaired Majorana fermions in quantum wires, *Physics-Uspekhi* **44**, 131 (2001). 2, 29, 34, 38, 42, 58, 63, 64

[13] Liang Jiang, Takuya Kitagawa, Jason Alicea, A. R. Akhmerov, David Pekker, Gil Refael, J. Ignacio Cirac, Eugene Demler, Mikhail D. Lukin, and Peter Zoller, Majorana fermions in equilibrium and in driven cold-atom quantum wires, *Physical Review Letters* **106**, 220402 (2011). 2

[14] Sebastian Diehl, Enrique Rico, Mikhail A. Baranov, and Peter Zoller, Topology by dissipation in atomic quantum wires, *Nature Physics* **7**, 971 (2011). 2

[15] Antonio Acín, Immanuel Bloch, Harry Buhrman, Tommaso Calarco, Christopher Eichler, Jens Eisert, Daniel Esteve, Nicolas Gisin, Steffen J. Glaser, Fedor Jelezko, et al., The quantum technologies roadmap: A European community view, *New Journal of Physics* **20**, 080201 (2018). 2

[16] Richard P. Feynman, Simulating physics with computers, *International journal of theoretical physics* **21**, 467 (1982). 2

[17] Saleh Rahimi-Keshari, Timothy C. Ralph, and Carlton M. Caves, Sufficient conditions for efficient classical simulation of quantum optics, *Physical Review X* **6**, 021039 (2016). 2

[18] Katherine L. Brown, William J. Munro, and Vivien M. Kendon, Using quantum computers for quantum simulation, *Entropy* **12**, 2268 (2010). 2

[19] Christopher J. Turner, Konstantinos Meichanetzidis, Zlatko Papić, and Jiannis K. Pachos, Optimal free descriptions of many-body theories, *Nature communications* **8**, 14926 (2017). 2, 76, 83, 84, 102

[20] Falko Pientka, Leonid I. Glazman, and Felix von Oppen, Topological superconducting phase in helical Shiba chains, *Physical Review B* **88**, 155420 (2013). 3, 41, 43

[21] Lev Davidovich Landau, On the theory of phase transitions, *Ukrainian Journal of Physics* **11**, 19 (1937). 6

[22] Assa Auerbach, Interacting electrons and quantum magnetism, Springer Science & Business Media (2012). 6, 103

[23] Lev Davidovich Landau and Evgenii Mikhailovich Lifshitz, Statistical physics, Course of theoretical physics, Pergamon, London (1958), Translated from the Russian. 6

[24] Subir Sachdev, Quantum phase transitions, *Handbook of Magnetism and Advanced Magnetic Materials* . 7

[25] Xie Chen, Zheng-Cheng Gu, and Xiao-Gang Wen, Local unitary transformation, long-range quantum entanglement, wave function renormalization, and topological order, *Physical Review B* **82**, 155138 (2010). 7

[26] Xiao-Gang Wen, Quantum field theory of many-body systems: from the origin of sound to an origin of light and electrons, Oxford University Press on Demand (2004). 7

[27] V. Kalmeyer and R. B. Laughlin, Equivalence of the resonating-valence-bond and fractional quantum Hall states, *Physical Review Letters* **59**, 2095 (1987). 8

[28] X. G. Wen, Frank Wilczek, and A. Zee, Chiral spin states and superconductivity, *Physical Review B* **39**, 11413 (1989). 8

[29] X. G. Wen, Vacuum degeneracy of chiral spin states in compactified space, *Physical Review B* **40**, 7387 (1989). 8

[30] D. C. Tsui, H. L. Stormer, and A. C. Gossard, Two-Dimensional Magnetotransport in the Extreme Quantum Limit, *Physical Review Letters* **48**, 1559 (1982). 8, 9, 14

[31] Xiao-Gang Wen, Topological order: From long-range entangled quantum matter to a unified origin of light and electrons, *ISRN Condensed Matter Physics* **2013**. 8, 15

[32] Edwin H Hall, On a new action of the magnet on electric currents, *American Journal of Mathematics* **2**, 287 (1879). 8

[33] K. v Klitzing, Gerhard Dorda, and Michael Pepper, New method for high-accuracy determination of the fine-structure constant based on quantized Hall resistance, *Physical Review Letters* **45**, 494 (1980). 9

[34] Robert B. Laughlin, Anomalous quantum Hall effect: an incompressible quantum fluid with fractionally charged excitations, *Physical Review Letters* **50**, 1395 (1983). 10, 14, 15

[35] Jainendra K. Jain, Composite fermion theory of exotic fractional quantum Hall effect, *Annual Review of Condensed Matter Physics* **6**, 39 (2015). 10, 11, 15

[36] Y. Aharonov and D. Bohm, Significance of Electromagnetic Potentials in the Quantum Theory, *Physical Reveiw* **115**, 485 (1959). 12

[37] Y Hatsugai, Topological aspects of the quantum Hall effect, *Journal of Physics: Condensed Matter* **9**, 2507 (1997). 12

[38] Michael Victor Berry, Quantal phase factors accompanying adiabatic changes, *Proceedings of the Royal Society of London. A. Mathematical and Physical Sciences* **392(1802)**, 45 (1984). 13

[39] David J. Thouless, Mahito Kohmoto, M. Peter Nightingale, and M. den Nijs, Quantized Hall conductance in a two-dimensional periodic potential, *Physical Review Letters* **49**, 405 (1982). 13

[40] Xiao-Gang Wen, Topological orders and edge excitations in fractional quantum Hall states, *Advances in Physics* **44**, 405 (1995). 15

[41] Alexei Kitaev, Anyons in an exactly solved model and beyond, *Annals of Physics* **321**, 2 (2006). 15

[42] Lucile Savary and Leon Balents, Quantum spin liquids: a review, *Reports on Progress in Physics* **80**, 016502 (2016). 15

[43] Nicholas Read and E. Rezayi, Beyond paired quantum Hall states: Parafermions and incompressible states in the first excited Landau level, *Physical Review B* **59**, 8084 (1999). 15

[44] Xiao-Gang Wen, Colloquium: Zoo of quantum-topological phases of matter, *Reviews of Modern Physics* **89**, 041004 (2017). 16

[45] Alexander Altland and Martin R. Zirnbauer, Nonstandard symmetry classes in mesoscopic normal-superconducting hybrid structures, *Physical Review B* **55**, 1142 (1997). 16, 19, 62

[46] Ching-Kai Chiu, Jeffrey CY Teo, Andreas P Schnyder, and Shinsei Ryu, Classification of topological quantum matter with symmetries, *Reviews of Modern Physics* **88**, 035005 (2016). 16, 17, 18

[47] Themistocles M Rassias, Inner product spaces and applications, volume 376, CRC Press (1997). 16

[48] Ari M. Turner, Yi Zhang, and Ashvin Vishwanath, Band topology of insulators via the entanglement spectrum, preprint arXiv:0909.3119 (2009). 21

[49] Ingo Peschel, Calculation of reduced density matrices from correlation functions, *Journal of Physics A: Mathematical and General* **36**, L205 (2003). 22

[50] Hui Li and F. Duncan M. Haldane, Entanglement spectrum as a generalization of entanglement entropy: Identification of topological order in non-abelian fractional quantum hall effect states, *Physical Review Letters* **101**, 010504 (2008). 26

[51] Lukasz Fidkowski, Entanglement spectrum of topological insulators and superconductors, *Physical Review Letters* **104**, 130502 (2010). 26, 67

[52] Steven R. White, Density matrix formulation for quantum renormalization groups, *Physical Review Letters* **69**, 2863 (1992). 26, 28

[53] Steven R. White, Density-matrix algorithms for quantum renormalization groups, *Physical Review B* **48**, 10345 (1993). 26, 28

[54] Guifre Vidal, José Ignacio Latorre, Enrique Rico, and Alexei Kitaev, Entanglement in quantum critical phenomena, *Physical Review Letters* **90**, 227902 (2003). 27

[55] José Ignacio Latorre, Enrique Rico, and Guifre Vidal, Ground state entanglement in quantum spin chains, *Quantum Information and Computation* **4**, 48 (2004). 27

[56] Matthew B. Hastings, An area law for one-dimensional quantum systems, *Journal of Statistical Mechanics: Theory and Experiment* **2007**, P08024 (2007). 27

[57] Elliott Lieb, Theodore Schultz, and Daniel Mattis, Two soluble models of an antiferromagnetic chain, *Annals of Physics* **16**, 407 (1961). 28

[58] Xiao-Gang Wen, Topological orders in rigid states, *International Journal of Modern Physics B* **4**, 239 (1990). 33

[59] D. J. Thouless, Long-range order in one-dimensional Ising systems, *Physical Review* **187**, 732 (1969). 33

[60] R. Islam, C. Senko, W. C. Campbell, S. Korenblit, J. Smith, A. Lee, E. E. Edwards, C.-C. J. Wang, J. K. Freericks, and C. Monroe, Emergence and

frustration of magnetism with variable-range interactions in a quantum simulator, *Science* **340**, 583 (2013). 41, 43

[61] Falko Pientka, Leonid I. Glazman, and Felix von Oppen, Unconventional topological phase transitions in helical Shiba chains, *Physical Review B* **89**, 180505 (2014). 41, 43

[62] Joseph W Britton, Brian C Sawyer, Adam C Keith, C-C Joseph Wang, James K Freericks, Hermann Uys, Michael J. Biercuk, and John J. Bollinger, Engineered two-dimensional Ising interactions in a trapped-ion quantum simulator with hundreds of spins, *Nature* **484**, 489 (2012). 41

[63] Yuezhen Niu, Suk Bum Chung, Chen-Hsuan Hsu, Ipsita Mandal, S. Raghu, and Sudip Chakravarty, Majorana zero modes in a quantum Ising chain with longer-ranged interactions, *Physical Review B* **85**, 035110 (2012). 42

[64] Davide Vodola, Luca Lepori, Elisa Ercolessi, Alexey V Gorshkov, and Guido Pupillo, Kitaev chains with long-range pairing, *Physical Review Letters* **113**, 156402 (2014). 42, 115

[65] Davide Vodola, Luca Lepori, Elisa Ercolessi, and Guido Pupillo, Long-range Ising and Kitaev models: Phases, correlations and edge modes, *New Journal of Physics* **18**, 015001 (2015). 42

[66] Areg Ghazaryan and Tapash Chakraborty, Long-range Coulomb interaction and Majorana fermions, *Physical Review B* **92**, 115138 (2015). 42

[67] Oscar Viyuela, Davide Vodola, Guido Pupillo, and Miguel Angel Martin-Delgado, Topological massive Dirac edge modes and long-range superconducting Hamiltonians, *Physical Review B* **94**, 125121 (2016). 42, 46, 62

[68] L. Lepori and L. Dell'Anna, Long-range topological insulators and weakened bulk-boundary correspondence, *New Journal of Physics* **19**, 103030 (2017). 42

[69] Antonio Alecce and Luca Dell'Anna, Extended Kitaev chain with longer-range hopping and pairing, *Physical Review B* **95**, 195160 (2017). 42, 48, 62, 114

[70] Martin J Klein, On a degeneracy theorem of Kramers, *American Journal of Physics* **20**, 65 (1952). 45

[71] Shinsei Ryu, Andreas P. Schnyder, Akira Furusaki, and Andreas W. W. Ludwig, Topological insulators and superconductors: Tenfold way and dimensional hierarchy, *New Journal of Physics* **12**, 065010 (2010). 46

[72] Sergey S. Pershoguba and Victor M. Yakovenko, Shockley model description of surface states in topological insulators, *Physical Review B* **86**, 075304 (2012). 50, 53

[73] Doru Sticlet, Edge states in Chern Insulators and Majorana fermions in topological superconductors, Ph.D. thesis, Universite Paris-Sud (2012). 50

[74] Konstantinos Meichanetzidis, Mauro Cirio, Jiannis K. Pachos, and Ville Lahtinen, Anatomy of fermionic entanglement and criticality in Kitaev spin liquids, *Physical Review B* **94**, 115158 (2016). 50

[75] Konstantinos Meichanetzidis, Diagnosing Topological Quantum Matter via Entanglement Patterns, Ph.D. thesis, University of Leeds (2017). 50

[76] Andreas P. Schnyder, Shinsei Ryu, Akira Furusaki, and Andreas W. W. Ludwig, Classification of topological insulators and superconductors in three spatial dimensions, *Physical Review B* **78**, 195125 (2008). 62

[77] J. S. Lomont and M. S. Cheema, Properties of Pfaffians, *The Rocky Mountain Journal of Mathematics* **15**, 493 (1985). 65

[78] Markus Legner and Titus Neupert, Relating the entanglement spectrum of noninteracting band insulators to their quantum geometry and topology, *Physical Review B* **88**, 115114 (2013). 66

[79] Matthew B. Hastings and Tohru Koma, Spectral gap and exponential decay of correlations, *Communications in Mathematical Physics* **265**, 781 (2006). 74, 115

[80] Pierre Hohenberg and Walter Kohn, Inhomogeneous electron gas, *Physical Review* **136**, B864 (1964). 76, 77, 78, 80

[81] Aron J. Cohen, Paula Mori-Sánchez, and Weitao Yang, Challenges for density functional theory, *Chemical reviews* **112**, 289 (2011). 76, 82

[82] Jake Southall, An Investigation into the Properties of Interacting Fermionic Systems, Master's thesis, University of Leeds (2017). 76, 85

[83] Konstantinos Meichanetzidis, Christopher J. Turner, Ashk Farjami, Zlatko Papić, and Jiannis K. Pachos, Free-fermion descriptions of parafermion chains and string-net models, *Physical Review B* **97**, 125104 (2018). 76

[84] Samuel Spillard, Christopher J. Turner, and Konstantinos Meichanetzidis, Machine learning entanglement freedom or: How I learned to stop worrying and love linear regression, preprint arXiv:1803.01035 (2018). 76

[85] Jiannis K. Pachos and Zlatko Papić, Quantifying the effect of interactions in quantum many-body systems, *SciPost Physics Lecture Notes* **2018**, 4 (2018). 76, 85

[86] Walter Kohn and Lu Jeu Sham, Self-consistent equations including exchange and correlation effects, *Physical Review* **140**, A1133 (1965). 77, 80

[87] Marcela Herrera, Roberto M Serra, and Irene D'Amico, DFT-inspired methods for quantum thermodynamics, *Scientific Reports* **7**, 4655 (2017). 77, 81, 95, 96

[88] J. P. Coe, A. Sudbery, and I. D'amico, Entanglement and density-functional theory: Testing approximations on Hooke's atom, *Physical Review B* **77**, 205122 (2008). 77

[89] John C. Slater, The theory of complex spectra, *Physical Review* **34**, 1293 (1929). 78

[90] D. R. Hartree, The Wave Mechanics of an Atom with a Non-Coulomb Central Field. Part II: Some Results and Discussion, *Mathematical Proceedings of the Cambridge Philosophical Society* **24**, 111–132 (1928). 78

[91] Vladimir Fock, Näherungsmethode zur Lösung des quantenmechanischen Mehrkörperproblems, *Zeitschrift für Physik* **61**, 126 (1930). 78

[92] Mel Levy and John P. Perdew, The constrained search formulation of density functional theory, In Density functional methods in physics, 11, Springer (1985). 80

[93] Andreas Görling, Density-functional theory for excited states, *Physical Review A* **54**, 3912 (1996). 80

[94] Robert O. Jones, Density functional theory: Its origins, rise to prominence, and future, *Reviews of Modern Physics* **87**, 897 (2015). 80, 82

[95] N. M. Harrison, An introduction to density functional theory, *Nato Science Series Sub Series III Computer and Systems Sciences* **187**, 45 (2003). 81

[96] David M Ceperley and BJ Alder, Ground state of the electron gas by a stochastic method, *Physical Review Letters* **45**, 566 (1980). 81

[97] L.-A. Wu, M. S. Sarandy, D. A. Lidar, and L. J. Sham, Linking entanglement and quantum phase transitions via density-functional theory, *Physical Review A* **74**, 052335 (2006). 82

[98] Michael A. Nielsen and Isaac Chuang, Quantum computation and quantum information, Cambridge University Press (2002). 84, 89

[99] Damian Markham, Jarosław Adam Miszczak, Zbigniew Puchała, and Karol Życzkowski, Quantum state discrimination: A geometric approach, *Physical Review A* **77**, 042111 (2008). 85

[100] Arcadii Z Grinshpan, General inequalities, consequences and applications, *Advances in Applied Mathematics* **34**, 71 (2005). 90

[101] I. D'amico, J. P. Coe, VV. França, and K. Capelle, Quantum mechanics in metric space: Wave functions and their densities, *Physical Review Letters* **106**, 050401 (2011). 90

[102] John Hubbard, Electron correlations in narrow energy bands, *Proceedings of the Royal Society of London. Series A. Mathematical and Physical Sciences* **276**, 238 (1963). 95

[103] Fabian H. L. Essler, Holger Frahm, Frank Göhmann, Andreas Klümper, and Vladimir E. Korepin, The one-dimensional Hubbard model, Cambridge University Press (2005). 96, 97

[104] Hal Tasaki, The Hubbard model: An introduction and selected rigorous results, *Journal of Physics: Condensed Matter* **10**, 4353 (1998). 96

[105] M. J. Martins and R. M. Fye, Bethe ansatz results for Hubbard chains with toroidal boundary conditions, *Journal of Statistical Physics* **64**, 271 (1991). 96

[106] Elliott H. Lieb and F. Y. Wu, Absence of Mott transition in an exact solution of the short-range, one-band model in one dimension, *Physical Review Letters* **20**, 1445 (1968). 96, 97

[107] B. Sriram Shastry and Bill Sutherland, Twisted boundary conditions and effective mass in Heisenberg-Ising and Hubbard rings, *Physical Review Letters* **65**, 243 (1990). 96

[108] Krissia Zawadzki, Irene D'Amico, and Luiz N Oliveira, Symmetries and boundary conditions with a twist, *Brazilian Journal of Physics* **47**, 488 (2017). 96

[109] V. J. Emery, Theory of the quasi-one-dimensional electron gas with strong "on-site" interactions, *Physical Review B* **14**, 2989 (1976). 96

[110] A. M. S. Macêdo and M. D. CoutinheFilho, Numerical studies of Hubbard clusters: exact diagonalization and Monte-Carlo simulation, *Revista Brasileira de Física* **21**. 96

[111] D. J. Scalapino, Numerical studies of the 2D Hubbard model, In Handbook of High-Temperature Superconductivity, 495, Springer (2007). 96

[112] B. Sriram Shastry, Infinite conservation laws in the one-dimensional Hubbard model, *Physical Review Letters* **56**, 1529 (1986). 96, 97

[113] Xi-Wen Guan, Algebraic Bethe ansatz for the one-dimensional Hubbard model with open boundaries, *Journal of Physics A: Mathematical and General* **33**, 5391 (2000). 96

[114] Ryotaro Arita, Kazuhiko Kuroki, Hideo Aoki, and Michele Fabrizio, Density-matrix renormalization-group study of the spin gap in a one-dimensional Hubbard model: Effect of the distant transfer and exchange coupling, *Physical Review B* **57**, 10324 (1998). 96

[115] Antoine Georges, Gabriel Kotliar, Werner Krauth, and Marcelo J. Rozenberg, Dynamical mean-field theory of strongly correlated fermion systems and the limit of infinite dimensions, *Reviews of Modern Physics* **68**, 13 (1996). 96

[116] Zhaojun Bai, Wenbin Chen, Richard Scalettar, and Ichitaro Yamazaki, Numerical methods for quantum Monte Carlo simulations of the Hubbard model, In Multi-Scale Phenomena In Complex Fluids: Modeling, Analysis and Numerical Simulation, 1, World Scientific (2009). 96

[117] J. P. F. LeBlanc, Andrey E. Antipov, Federico Becca, Ireneusz W. Bulik, Garnet Kin-Lic Chan, Chia-Min Chung, Youjin Deng, Michel Ferrero, Thomas M. Henderson, Carlos A. Jiménez-Hoyos, et al., Solutions of the two-dimensional Hubbard model: benchmarks and results from a wide range of numerical algorithms, *Physical Review X* **5**, 041041 (2015). 96

[118] Daniel Zwillinger, CRC standard mathematical tables and formulae, Chapman and Hall/CRC (2002). 99

[119] Paola Gori-Giorgi, Michael Seidl, and G. Vignale, Density-functional theory for strongly interacting electrons, *Physical Review Letters* **103**, 166402 (2009). 111